UCLouvain

epl

École polytechnique de Louvain

Ion guiding, filtering and trapping with a single quadrupole device

Author: **Cyrille SEPULCHRE**
Supervisors: **Clément LAUZIN, Xavier URBAIN**
Readers: **Arnaud DELCORTE, Benoit HACKENS**
Academic year 2019–2020
Master [120] in Physical Engineering

Abstract

This master thesis investigates the characterisation of a quadrupole device in order to include it in an experiment dedicated to the study of the $[(CO_2)_m\text{-}(H_2O)_n]^+$ ionic clusters using high-resolution rovibrational spectroscopy. The interest of a quadrupolar element is triple: it can be used as an ion guide, as a mass filter or as an ion trapping system. In this work, it is shown that the same quadrupole device can be used in those three different purposes. This master thesis focuses mainly on the development of numerical simulations about the quadrupole. The quadrupole which will be used in the laboratory is noted quadrupole A in this work, and its performances are compared with two other systems, noted quadrupole B and quadrupole C. The quadrupole B is a newly designed quadrupole with round rods reproducing a hyperbolic field shape and the quadrupole C is designed with hyperbolic rods, allowing one to use the formalism of the Mathieu equation. The stability triangle of each system is derived. It is shown, through numerical simulations performed in SIMION and with a self-made *Python* script, that the quadrupole A can act as an ion guide, as a mass filter and as an ion trapping system. The *Python* script has been extended, allowing one to simulate ion trajectories in a multipolar system of any order. Those developments are particularly interesting to design future traps in the laboratory. Then, the current experimental setup is briefly presented, followed by a possible design for the future experiment including the quadrupole. With that new experimental setup, the required conditions to perform continuous excitation are discussed. Finally, the design of a miniaturised quadrupole is proposed, opening opportunities for the study of larger molecules.

Acknowledgements

This master thesis is the result of a long and complete work needing the participation of a whole team that I would like to thank here below.

First of all, I would like to particularly thank my promotor, Professor Clément Lauzin, for his daily presence, his numerous advices and his flexibility given the peculiar situation. It was a great opportunity for me to discover spectroscopic experiments like that, to introduce me into that field of research and to work in his team. I would like to thank my co-promotor, Professor Xavier Urbain, for his precious tips on some particular points. Both of them helped me and guided me on the right tracks to achieve this final work. They played also an important role in my thinking about my professional future and I would like to thank them for that time.

My warms thanks are also addressed to the Professors Rizzo and Boyarkin from EPFL who introduced me to their researches about multipolar devices before the start of my thesis.

I would like to thank A. Roucou who explained me the details of the laboratory experiment. He showed me the great daily real life of a researcher and he guided me a lot regarding the reflections about the new experimental setup.

I would like to thank M. Daman who built the whole electronics of the quadrupole, for his explanations and for his help in the design of the new miniaturised quadrupole. Special thanks to all the members of the electronics and mechanics workshop, for their availability and for their numerous tips. Thank you also to R. Glorieux and to all the members of the team of Pr. Lauzin and Urbain for the great shares and the general good atmosphere.

Finally, I would like to thank my family and friends who supported me every day, even more in this particular pandemic situation.

Contents

Chapter 1

Introduction and motivations

Since the 1950s, the field of atomic, molecular and optical physics (AMO) has witnessed several impressive breakthroughs. In terms of charged particles manipulation, Wolfgang Paul is the first scientist who succeeded experimentally to control an ion beam with a quadrupole [1]. Today, quadrupolar ion trapping systems are commonly called Paul traps in reference to his work. W. Paul received the Nobel Prize in Physics in 1989 with Hans G. Dehmelt "for the development of the ion trap technique." [2]. H. G. Dehmelt realised the experimental trapping inspired by Penning a few years before, and named it therefore the Penning trap [3].

With those traps, ion-photon [4] and ion-molecule reactions [5] can be studied in great details. The quadrupole can be used as an ion guiding system too, keeping the ion beam focused and injecting it properly into the next experimental element. The mass filtering of an ion beam is also possible with a quadrupole device, opening opportunities in high-resolution mass spectrometry. With the emergence of high power UV and IR lasers, spectroscopic studies of (macro-)molecules is performed and compared with the quantum physics theory of molecular states. Those breakthroughs were accompanied, in the 1960s-70s, by the extended theoretical description of the ion motion in a quadrupolar field, with the work of (among others) Peter Dawson [6] and Dieter Gerlich [7]. Their works summarise the basics of quadrupole fields, the uses of a quadupole device and outline some specific experimental effects such as the acceptance, the fringing fields, some non-linearities, etc.
A wide range of simulations have been performed more recently (in the 1990s-2000s) by Taylor *et al.* [8, 9, 10, 11]. They simulated a large number of realistic situations in order to precisely derive some typical behaviour of a quadrupole.

Thanks to the three main experimental uses of a quadrupole (ion guide, mass filter or ion trap), it is a versatile tool that can be included in a wide range of experiments. First of all, the quadrupole takes part in a lot of researches in fundamental physics: it is used, among others, to determine fundamental constants [12], to perform quantum physics experiments [13] or to do high-resolution spectroscopy [4]. Secondly, it is important in a wide range of biological studies: it allows one to analyse large biomolecules such as amino-acids [14], proteins [15] or even viruses [16] and it takes part in a lot of soft-landing processes (surface

deposition) [17].

In terms of fundamental physics, two main fields can be explored from the use of a quadrupole device. The first one is about very high-resolution spectroscopy of atoms and fundamental particles, in order to study quantum systems, implement atomic clocks, etc. One could cite, for example, all the work performed by the group of David Wineland (Nobel Prize in Physics in 2012) which combines in a perfect way all the notions of ion trapping, laser cooling and single ion spectroscopy [18, 19] and pushed the investigation of frequency standards much further than before. His group participated, for example, at the creation of entangled quantum states with trapped atomic ions [20] opening opportunities to the development of ion-trap quantum computers [21, 22].
The ALPHATRAP experiment [23], at the Max Planck Institute (Heidelberg, Germany), aims to perform experiments on hydrogenlike lead $^{128}Pb^{81+}$ in order to validate the quantum electrodynamics theory under high electromagnetic fields. In the experimental setup, some multipolar devices are used, the main one being a cryogenic Penning trap.
In the last years, the research field of atomic clocks has been pushed further in order to develop atomic clocks with highly charged ions (HCIs) [24, 25]. Their advantage lies in their extreme sensitivity, opening opportunities in the measurement and characterisation of candidates for dark matter, in the measurement of the variation of fundamental physics constants, etc.

The second investigation in terms of fundamental physics is related to the spectroscopy of species of astrophysical interest. The kinetic constants of chemical reactions occuring in space can also be determined with such a device. Among others, one could cite the important work of Dieter Gerlich who pioneered the use of the 22-pole trapping system instead of the usual quadrupole [26, 27, 28]. The 22-pole is usually coupled with a cold head in order to reproduce the outer space conditions and single spectral signatures. The studied ions are for instance hydrogen clusters [29, 30], water complexes [31], H_2D^+ [32] or even C_{60}^+ [33]. One high level experimental setup is for example the one of Oskar Asvany and Stephan Schlemmer, also including a 22-pole system in order to perform high-resolution spectroscopy on small ions. This setup is called COLTRAP and performs ion trapping at 4 K [34].

Then, spectroscopy on large ions and on biomolecules has been developed. The biggest problem in this study was to generate a biomolecular ion of high mass, but the development of techniques such as electrospray ionisation (ESI) [35, 36] and matrix assisted laser desorption ionisation (MALDI) [37, 38] overcame that problem. A wide overview of those techniques can be found in a paper written by Thomas Rizzo, Jaime Stearns and Oleg Boyarkin [39].

Another use of a quadrupole, more linked with the applied sciences, resides in soft landing. This idea has been introduced in 1977 by Franchetti *et al.* [40] and aims to prepare and modify surfaces with a slow mass-selected ion beam. The idea is to change the properties of a surface in order to perform material analysis, mass spectrometry, surface science, etc. A

wide range of experimental installations including quadrupole devices are used in order to perform soft landing [41, 42]. Among others, one could cite the BEEQ, coupling a magnetic sector (B) with two electric sectors (EE) and an electric quadrupole mass filter (Q) [43]. The setup of J. Laskin's research group is instead made of two quadrupoles, operating in ion guiding and mass selection mode respectively [44]. Finally, a third kind of experimental setup, in the research group of Blake *et al.*, uses an ion trapping system after the quadrupole mass filter [45, 46].

One final and very contemporary hot topic is the use of a quadrupole mass filter in the viral analysis. It has been proven [16] that an ionic virus can be generated, guided and filtered even with a mass of 40 million Da. A triple quadrupole mass filter is used in that experiment in order to select effectively the virus. It has been surprisingly observed, also in other studies [47, 48], that even after ionisation, mass selection and detection, the virus is intact and has kept its infectivity. Thanks to a high development in terms of instrumentation, it is now possible to analyse in depth the viruses and some incoming technologies presented in [49] seem promising for the future.

In this work, a quadrupole system is analysed in detail. Its purpose is to take part in an experiment aiming to perform high-resolution photodissociation spectroscopy on CO_2^+ and $[(CO_2)_m\text{-}(H_2O)_n]^+$ complexes. The motivation behind this investigation is to show that the same quadrupole device can act as an ion guide, as a mass filter and as an ion trapping system. Three different quadrupoles are compared in the following. Therefore, different denominations are used in order to avoid any confusion. The quadrupole used in the laboratory is called quadrupole A. A second quadrupole, with round rods of a ratio $r/r_0 = 1.1468$ (where r is the radius of the rods and r_0 is the free field radius between the rods) and reproducing ideally the desired hyperbolic field shape, is called quadrupole B. The last quadrupole, with a perfect hyperbolic field, is called quadrupole C.

In the next chapter, the theoretical formalism is explained: the equations of motion and the stability regions of an ion travelling into a quadrupole are presented. This theoretical formalism is extended to multipolar elements of any higher order. Then, the quadrupole A is presented in the chapter 3. Some theoretical results are reproduced thanks to simulations in SIMION and *Python*. The quadrupole A is compared with two other quadrupolar systems, B and C. The expected performances in terms of ion guiding, mass filtering (and the associated mass resolution) and ion trapping are presented in the chapter 4. Due to the Covid-19 pandemic and the consequent closure of the laboratory, the quadrupole has not been tested on the existing spectrometer. Still, in the chapter 5, the current experimental setup is introduced and a new experimental setup, using the quadrupole for infrared photodissociation spectroscopy, has been designed for a future possible implementation. The ability to perform continuous excitation is discussed and a presentation of a smaller quadrupole, improving the setup, is done at the end of this master thesis.

Chapter 2

State of the art

2.1 The quadrupole

Starting from the basics, an electric quadrupole device is a device made of four electrodes on which a certain voltage is applied. The purpose of a quadrupole is to act on a beam of charged particles. The force acting on those particles is the Lorentz force:

$$\vec{F} = q\vec{E} + q\vec{v} \times \vec{B} \tag{2.1}$$

with $\vec{F}$ the force applied on the particle in [N], q its charge in [C], $\vec{E}$ the applied electric field in [V/m], $\vec{v}$ the velocity of the particle in [m/s] and $\vec{B}$ the applied magnetic field in [T]. The latter is equal to zero in this study, the quadrupole is purely electrical.

There are two main kinds of quadrupoles widely developed in ion beam experiments: 2D and 3D quadrupoles. Their respective representations are given in Figure 2.1. The purpose of each quadrupole is different. In the 2D quadrupole, the system is open at both ends in the z direction: ions will flow through the quadrupole. In the 3D design instead, the quadrupole is closed and ions will therefore be confined: the quadrupole will only act as an ion trapping system.

The presented quadrupoles in Figure 2.1 are made of hyperbolic electrodes, which is useful in terms of potential description (see subsection 2.1.2). In this work, the used quadrupole is a 2D system, represented in Figure 2.2. It is made of four round rods, each rod being equally distributed on a circle of inscribed radius r_0. The rods are circular instead of hyperbolic and a discussion about this approximation will be done in the chapter 3. It is surrounded by an outer cap cylinder which is grounded to isolate the system.

In order to guide and confine ions, an alternating field with an eventual DC offset is applied to the electrodes. Due to the frequency range of the alternating field, mostly in the range of the MHz, one usually speaks about *radiofrequency quadrupoles* (RFQ). The radiofrequency is applied such that each opposite electrode has the same potential, and

two neighbour electrodes have an opposite potential (π-shifted). The charged particles will bounce back and forth between the rods while travelling through the quadrupole.

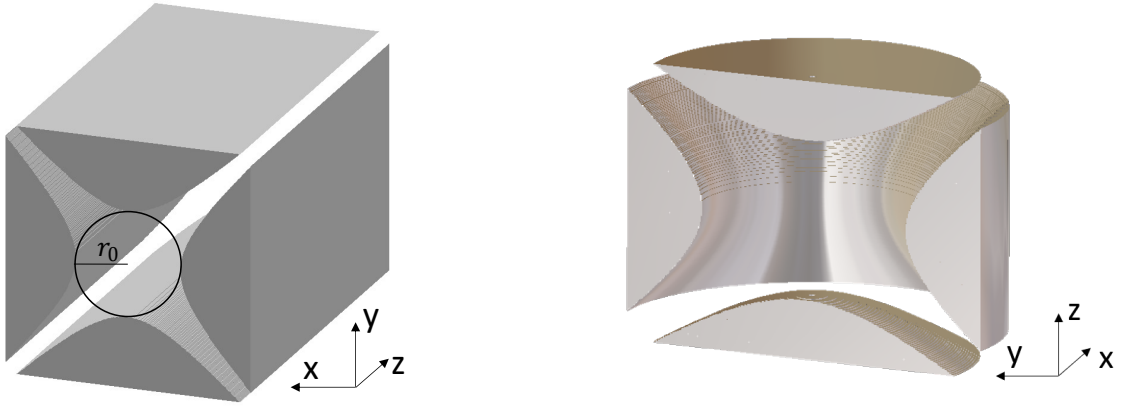

(a) (b)

Figure 2.1: Schematic representation of two quadrupoles made of hyperbolic electrodes. (a) 2D quadrupole and (b) a cross-sectional view of 3D quadrupole, also known as Paul trap.

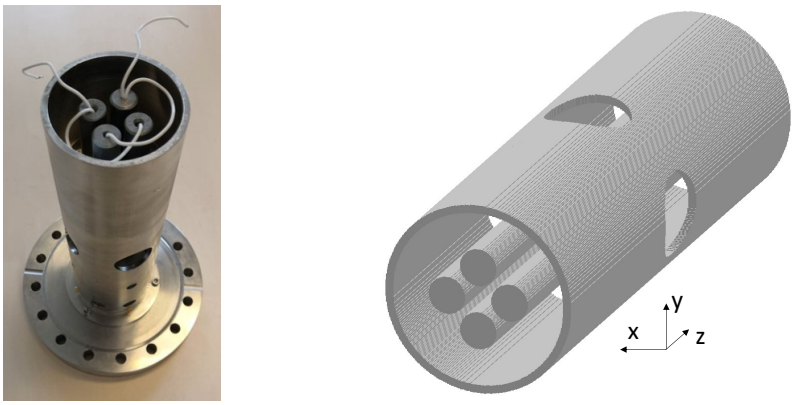

(a) (b)

Figure 2.2: (a) Picture of the quadrupole device that will be used in the future laboratory experiment, mounted on a flange and with its connectors (white wires) and (b) schematic representation of the quadrupole A.

2.1.1 Ion motion in an oscillatory field

The ion motion in an oscillatory field is the key point to understand the conditions of operation of a quadrupole. It has been widely studied by Gerlich (1992): this section is inspired by the second chapter of [7]. It has been mentioned before that the force acting on

the ions is the Lorentz force (Equation 2.1), so in absence of a magnetic field, the equation of motion is:

$$m\ddot{\vec{r}} = q\vec{E_0}(\vec{r})\ cos(\Omega t + \phi) + q\vec{E_s}(\vec{r}) \tag{2.2}$$

with m the mass in [kg], $\vec{r}$ the position vector in [m] and q the charge in [C]. The electric field is the sum of two terms: a static field and an oscillatory field, noted $\vec{E_s}$ and $\vec{E_0}$ respectively (in [V/m]), with Ω the angular frequency of the oscillatory field in [rad/s] and ϕ the angular phase in [rad].

In the simplest case, one can consider that the electric field is a purely oscillating field ($\vec{E_s}(\vec{r}) = \vec{0}$) without any phase shift ($\phi = 0$). The solution is then trivial:

$$\vec{r}(t) = \vec{R_0} - \vec{a}\ cos(\Omega t) \qquad \text{with} \qquad \vec{a} = \frac{q\vec{E_0}}{m\Omega^2} \tag{2.3}$$

with r_0 the initial position of the ion in [m] and $\vec{a}$ the amplitude of the oscillation in [m]. Each term is considered to be expressed in SI units. A typical value of the norm of $\vec{a}$ can be derived by taking $m = 44$ amu (corresponding to CO_2^+ or N_2O^+, 1 amu = 1.66 10^{-27} kg), $q = 1.60\ 10^{-19}$ C (for a singly charged ion), $\Omega = 2\pi \times 1$ MHz and the norm of the electric field is close to $|\vec{E_0}| \simeq 5\ 10^3$ V/m. It turns out that $|\vec{a}| \simeq 10^{-4}$ m.

Most of the time, the equation of motion is inhomogeneous given the shape of the electric field. Consequently, it can be solved analytically for a set of particular geometries only. The purpose of this section is not to derive all the mathematical principles behind the resolution of Equation 2.2 depending on the shape of the electric field. One single relevant solution (more general than Equation 2.3) will be considered, corresponding to the solution under the so-called adiabatic approximation.

The idea is to distinguish two contributions to the ion trajectory in the quadrupole: a slow drift term (the secular motion) and a fast oscillating term (the micromotion). This hypothesis is valid if Ω is high enough to keep $\vec{a}$ small compared to R_0. For example, in the approximation made before for $|\vec{a}| \simeq 10^{-4}$ m, this hypothesis is valid if $R_0 \gtrsim 5\ 10^{-3}$ m. The solution is then written as:

$$\vec{r}(t) = \underbrace{\vec{R_0}(t)}_{\text{smooth drift}} + \underbrace{\vec{R_1}(t)}_{\text{oscillating term}} \tag{2.4}$$

with, from Equation 2.3, $\vec{R_1}(t) = -\vec{a}cos(\Omega t)$. By considering also that $\vec{E}(\vec{r}, t)$ varies smoothly with $\vec{r}$, the electric field can be expanded around $\vec{R_0}$ as:

$$\vec{E}(\vec{r}) = \vec{E_0}(\vec{R_0}) + \vec{\nabla}\vec{E}(\vec{R_0})\ (\vec{r} - \vec{R_0}) + ... \tag{2.5}$$

and recalling the definition of $\vec{r}$ (Equation 2.4), it can be written:

$$\vec{E}(\vec{r}) = \vec{E_0}(\vec{R_0}) - (\vec{a} \cdot \vec{\nabla})\ \vec{E}(\vec{R_0})\ cos(\Omega t) + ... \tag{2.6}$$

Getting back to the equation of motion (Equation 2.2), with the hypothesis of $\vec{E_s}(\vec{r}) = 0$ and $\phi = 0$, one has for the acceleration part:

$$\begin{aligned} m\ddot{\vec{r}} &= m(\ddot{\vec{R}_0} + \ddot{\vec{R}_1}) \\ &= m\ddot{\vec{R}_0} + m[-\ddot{\vec{a}}cos(\Omega t) + 2\dot{\vec{a}}\Omega sin(\Omega t) + \vec{a}\Omega^2 cos(\Omega t)] \\ &\simeq m\ddot{\vec{R}_0} + m\vec{a}\Omega^2 cos(\Omega t) \\ &\simeq m\ddot{\vec{R}_0} + q\vec{E_0}cos(\Omega t) \end{aligned} \tag{2.7}$$

the derivatives of $\vec{a}$ have been neglected since they are taken as small compared to the smooth drift term. The electric field term is written by using Equation 2.6:

$$\begin{aligned} q\vec{E_0}cos(\Omega t + \phi) &= q[\vec{E_0}(\vec{R_0}) - (\vec{a}\cdot\vec{\nabla})\ \vec{E}(\vec{R_0})\ cos(\Omega t)]cos(\Omega t) \\ &= q\vec{E_0}cos(\Omega t) - q(\vec{a}\cdot\vec{\nabla})\ \vec{E_0}(\vec{R_0})cos^2(\Omega t) \end{aligned} \tag{2.8}$$

Pluging the eqs. (2.7) and (2.8) in eq. (2.2), one can see that the $q\vec{E_0}cos(\Omega t)$ term cancels out. Consequently, the equation of motion becomes:

$$m\ddot{\vec{R}_0} = -q\ (\vec{a}\cdot\vec{\nabla})\ \vec{E_0}(\vec{R_0})\ cos^2(\Omega t) \tag{2.9}$$

$$\implies = \frac{-q^2}{m\Omega^2}(\vec{E_0}\cdot\vec{\nabla})\vec{E_0}cos^2(\Omega t) \tag{2.10}$$

$$\implies = \frac{-q^2}{2m\Omega^2}\nabla E_0^2\ cos^2(\Omega t) \qquad \text{(using vector analysis[1])} \tag{2.11}$$

$$\implies = \frac{-q^2}{4m\Omega^2}\nabla E_0^2 \qquad (\text{using} < cos^2(\Omega t) >_{period} = 1/2) \tag{2.12}$$

As long as the objective is to derive an equation of motion for the smooth drift term, the cosine term can be averaged over one period. This is also justified by the fact that by hypothesis, $\vec{R_0}$ varies smoothly and slightly over one oscillation period.

This equation shows that the ion is, on average, feeling a *field gradient force*. By adding a non-zero static electric field $\vec{E_s}(\vec{r}) = -\nabla\phi_s$, one obtains the final equation of motion:

$$m\ddot{\vec{R}_0} = -\nabla V^*(\vec{R_0}) \qquad \text{with} \qquad V^*(\vec{R_0}) = \frac{q^2E_0^2}{4m\Omega^2} + q\phi_s \tag{2.13}$$

where $V^*(\vec{R_0})$ is called the effective potential (in [V]). The derivation of this potential has important consequences. Firstly, it is valid in a wide range of common geometries. The equation of motion becomes a simple differential equation with no time dependence in the potential term. The only limitation, beyond the hypothesis made before, is related to the frequency of the motion: higher order harmonics are not considered in this approximation

[1] $(\vec{E}\cdot\vec{\nabla})\vec{E} = \frac{1}{2}\nabla\vec{E}^2 - \vec{E}\times(\vec{\nabla}\times\vec{E}) = \frac{1}{2}\nabla E^2$ because $(\vec{\nabla}\times\vec{E}) = 0$ by definition.

(only Ω is present in $R_1(t)$) although some other frequencies can be present in the secular motion.

To have an information about the energy of the moving ion, one has to integrate the Equation 2.13 over time. It gives:

$$\frac{1}{2}m\dot{\vec{R}}_0^2 + \frac{q^2E_0^2}{4m\Omega^2} + q\phi_s = E_m \tag{2.14}$$

with E_m the total energy of the ion in [J]. This quantity is called the adiabatic invariant of the motion since it remains constant all along the ion trajectory in the quadrupole. It shows the direct correspondence between the kinetic energy stored in the micromotion and the electric potential.

The final objective, to push the reasoning further, is to find the conditions under which the adiabaticity criterion is valid. Indeed, in general, the equation of motion is non-conservative and leads to an increase in the total energy of the ion. The adiabaticity criterion is satisfied if the oscillatory process is fast compared to the smooth drift, which is slow.

This dinstinction between *fast* and *slow* could be done by comparing the relative velocity of both motions, or by comparing the secular frequency of the ion ω with the RF frequency Ω, etc. Indeed, the secular motion is expected to be periodic in most of the cases (and in the case of a quadrupole), and the secular frequency of the motion ω is associated to that periodicity. Another possible distinction, recalling the Taylor expansion of the electric field (see Equation 2.8), is that the first order term, i.e. the change in the field, has to be small compared to the field $\vec{E}(\vec{R}_0)$ itself. This condition is written as:

$$\eta = \frac{|2(\vec{a}\cdot\vec{\nabla})\vec{E}_0|}{|\vec{E}_0|} = \frac{2q|\nabla E_0|}{m\Omega^2} \tag{2.15}$$

The first equality is the ratio between the electric field perturbation and the field amplitude. It has to be smaller than one to preserve adiabaticity. A complete discussion about the values of η ensuring adiabatic conditions can be found in the previously cited book of Gerlich [7]. The underlying development is not of particular interest here. The conclusion of the discussion is that, in most of the cases, the system is adiabatic if $\eta < 0.3$. This condition is not exclusive: an ion might have an adiabatic motion with $\eta > 0.3$ but it will depend on other factors than the ones considered here.

To conclude this section, it is important to note that adiabaticity and stability are not the same concept: an ion can have a stable trajectory even if its total energy changes along it. Under some conditions, the trajectory of an ion under the adiabatic conditions could also be unstable. The question is then: under which conditions can one consider that the ion has a stable trajectory along the quadrupole ? One answer can be that a trajectory is stable if and only if it has a bounded phase space. However, in a quadrupole of finite

length, ions with a non-bounded phase space can be transmitted if the latter is growing up slowly. Another definition, more appropriate, could be that a trajectory is stable if a small perturbation leads to a stable oscillatory equilibrium. This idea will be used in the next section to derive stability conditions of the quadrupole.

2.1.2 Application to the quadrupole : the Mathieu equation

The formalism derived in the previous section is quite general, making approximations on the applied field but not on the geometry. In this section, the equation of motion will be reconsidered with the particular potential seen in a 2D quadrupole. The following is widely inspired by the work of Dawson and Whetten [50] and March and Hughes [51]. They have reviewed previous works about the quadrupole behaviour in order to derive the complete mathematical description of the RFQ. In the case of a quadrupole, the equation of motion takes a specific form, known as the Mathieu equation. This equation can be derived from the potential distribution in a quadrupole:

$$\phi = \phi_0(\lambda x^2 + \sigma y^2 + \gamma z^2) \tag{2.16}$$

with λ, σ and γ being three factors depending on the geometry. The potential has to obey the Laplace equation:

$$\nabla^2\phi = 0 \tag{2.17}$$

$$\implies \quad \nabla^2[\phi_0(\lambda x^2 + \sigma y^2 + \gamma z^2)] = 0$$

$$\implies \quad \lambda + \sigma + \gamma = 0 \tag{2.18}$$

In the case of a 2D quadrupole with hyperbolic electrodes, one finds:

$$\lambda = -\sigma = \frac{1}{r_0^2} \qquad \text{and} \qquad \gamma = 0 \tag{2.19}$$

with r_0 the inscribed radius between the electrodes in [m]. Taking an alternating field of the form $U - Vcos(\Omega t + \phi)$, the Equation 2.16 can be written:

$$\phi = [U - Vcos(\Omega t + \phi)]\,\frac{x^2 - y^2}{r_0^2} \tag{2.20}$$

with U and V the DC and RF amplitudes respectively in [V], Ω the angular frequency of the oscillating field in [rad/s] and ϕ the phase shift in [rad].

Getting back to the equation of motion and knowing that the electric field derives from the potential given in Equation 2.20, one obtains:

$$E_x = -\frac{\partial\phi}{\partial x} = -\,[U - Vcos(\Omega t + \phi)]\,\frac{2x}{r_0^2} \tag{2.21}$$

$$E_y = -\frac{\partial\phi}{\partial y} = [U - Vcos(\Omega t + \phi)]\,\frac{2y}{r_0^2} \tag{2.22}$$

and for the equation of motion:

$$m\frac{d^2x}{dt^2} = -q\left[U - Vcos(\Omega t + \phi)\right]\frac{2x}{r_0^2} \tag{2.23}$$

$$m\frac{d^2y}{dt^2} = q\left[U - Vcos(\Omega t + \phi)\right]\frac{2y}{r_0^2} \tag{2.24}$$

It is important to note that, in this configuration, the x and y motions are decoupled, which is an advantage considering the resolution of the above equations. Those equations correspond to the Mathieu equation, of the form:

$$\frac{d^2u}{d\xi^2} + [a_u - 2q_u cos(2\xi + \phi)]u = 0 \tag{2.25}$$

By identification, one can find the adimensional Mathieu factors:

$$\xi = \frac{\Omega t}{2} \qquad a_u = \pm\frac{8qU}{m\Omega^2 r_0^2} \qquad q_u = \pm\frac{4qV}{m\Omega^2 r_0^2} \tag{2.26}$$

where, in the two previous equations, u denotes x or y. The coefficients are respectively positive in the x direction and negative in the y direction to be consistent with eqs. (2.23) and (2.24).

The solutions of that equation have been derived in 1868 by Émile Mathieu [52]. It is a special form of Hill's equation that can be applied to a wide range of oscillatory processes in physics. According to Floquet's theory, solutions of the Mathieu equation can be written in the following form (details in [53, 54, 55] for example):

$$u(\xi) = A_1 e^{\mu\xi} \sum_{n=-\infty}^{\infty} C_{2n} e^{2ni\xi} + A_2 e^{-\mu\xi} \sum_{n=-\infty}^{\infty} C_{2n} e^{-2ni\xi} \tag{2.27}$$

where A_1, A_2 are constants to be determined considering the initial conditions. The C_{2n} coefficients and the parameter μ depend only on the initial (a_u, q_u) combination and not on the initial conditions of the ion. This is a key property of the quadrupolar systems: the shape of the trajectory, i.e. the nature of the motion, will depend on the operating conditions only and not on the initial parameters (position, phase and velocity) of the ion.

Equation 2.27 tells one whether an ion will have a stable trajectory in the quadrupole or not. The stability criterion is considered to be the following: an ion has a stable trajectory if and only if u remains finite when ξ tends to infinity. Of course, this mathematical definition is not sufficient in a real setup: it will be precised further, by taking into account the finite dimensions of the quadrupole. Stability depends on the value of μ, which is a complex number. Considering $\mu = \alpha + i\beta$, one has three cases to distinguish:

1. $\alpha \neq 0$: the solution will be unstable because of either the $e^{\mu\xi}$ or $e^{-\mu\xi}$ term, diverging to infinity as ξ increases.

2. $\alpha = 0$ and β is real but non-integer: the solution will be periodic and stable. This is the zone of stability.

3. $\alpha = 0$ and β is an integer: the solution is periodic but unstable (see for example [55] or the third chapter in [56] for more details). This case allows one to determine the limits of each stability region.

Given the required conditions on μ and remembering that it only depends on a_u and q_u, it is possible to reconstruct the so-called stability diagram of the Mathieu equation. This diagram shows the regions in the (a_u, q_u) plane where the solutions do not diverge. The Mathieu equation being solved in both x and y directions independently, it is the superposition of both diagrams that provides the stability region of a quadrupole. If a periodic solution exists, the Equation 2.27 can be written:

$$u(\xi) = A_1 e^{\mu\xi} \sum_{n=-\infty}^{\infty} C_{2n} cos\left((2n+\beta)\xi\right) + A_2 e^{-\mu\xi} \sum_{n=-\infty}^{\infty} C_{2n} sin\left((2n+\beta)\xi\right) \tag{2.28}$$

One way to find the C_{2n} coefficients is by expressing them in a recurrence equation, involving the a_β and b_β parameters, directly related to a_u, q_u and β. The stability limits are usually expressed as a function of the parameter q_u and are given by the a_β and b_β characteristic curves, where $\beta \in \mathbb{Z}$. In the literature, a_β is usually related to even values of β and b_β to the odd ones. The stability diagram is usually reconstructed by considering iso-β lines where, for the first stability region, $\beta \in$ [0,1], for the second, $\beta \in$ [1,2], etc. For example, one can write the limits of the first stability region as [1]:

$$a_0 = -\frac{1}{2}q_u^2 + \frac{7}{128}q_u^4 - \frac{29}{2304}q_u^6 + ... \tag{2.29}$$

$$b_1 = 1 - q_u - \frac{1}{8}q_u^2 + \frac{1}{64}q_u^3 - ... \tag{2.30}$$

A graphical representation of the stability diagram is given in Figure 2.3. In Figure 2.3a, four stability regions are represented for positive q_u only. The system is stable in the shaded areas and the limits of those regions are indicated with a_β and b_β. The limits have been computed thanks to the `mathieu_a`(β, q_u) and `mathieu_b`(β, q_u) functions in the *scipy.special* package in *Python*. In Figure 2.3b, a zoom has been made on the zones of stability for the smallest (a_u, q_u) values. Both the stability regions along the x and y directions of the quadrupole are represented: as long as their voltages are opposite, there is a symmetry in their stability diagrams with respect to the q_u axis. The first stability zone is highlighted in the figure. It is mostly used in the experiments because of its accessibility in terms of electronical parameters.

The first stability region (by considering positive a_u values only), also called the stability triangle, is shown in Figure 2.4. The two limits are set by $-a_0$ and b_1 (see eqs. (2.29) and (2.30)). The quadrupole described in this work will operate in that stability triangle.

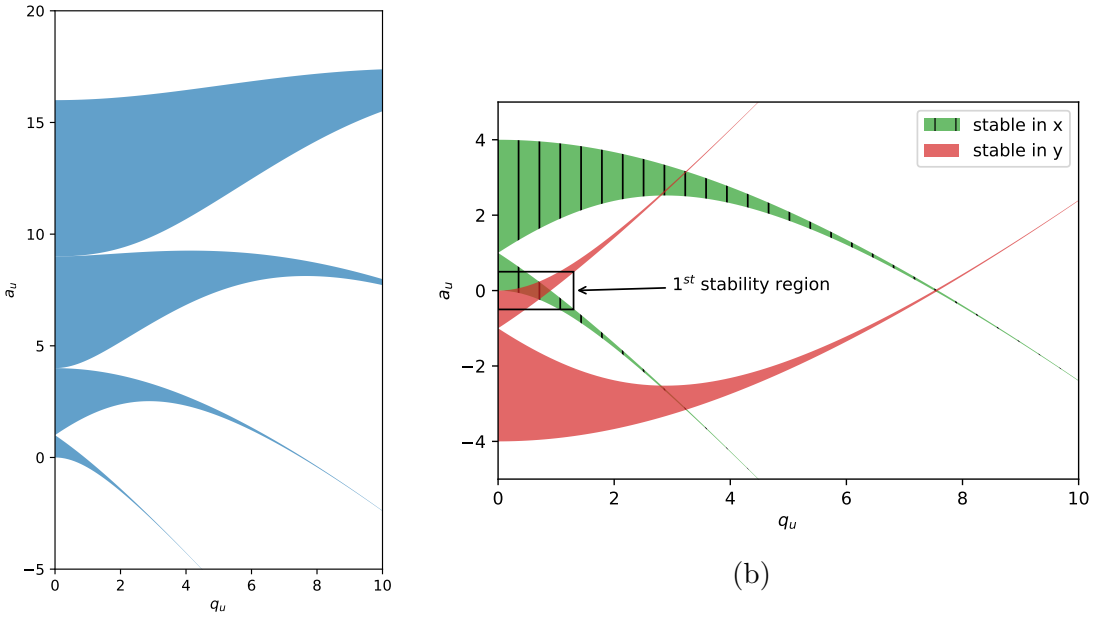

(a) (b)

Figure 2.3: (a) 4 stability regions computed from the solution of Mathieu equation (the figure is symmetric for $q_u < 0$ with respect to the a_u axis) and (b) zoom on the 1^{st} stability region of the quadrupole, obtained by overlapping both stability diagrams along the x and y directions.

The extreme q_u value is 0.904. That value tells one the minimal m/z ratio that can be selected in the ion guiding operating mode (see subsection 2.1.4). The apex of the stability triangle is denoted with an arrow in Figure 2.4. This operating condition is used in the case of mass filtering (see subsection 2.1.5). Finally, one can also note all the small region where $q_u < 0.3$: this is where the adiabatic approximation is valid.

One last point about this Mathieu equation and the stability of the ion motion concerns the frequency of oscillation of the ion. Given the Equation 2.28, one can see that the sine and cosine terms in the expansion are taking $(2n + \beta)\xi$ as an argument. Recalling the definition of ξ (see Equation 2.26), one can deduce that the secular frequency of the ion is:

$$\omega_{u,n} = (n \pm \frac{\beta_u}{2})\Omega \qquad \text{with } n \in \mathbb{Z} \tag{2.31}$$

this frequency is not unique: this is a spectrum depending on the value of β, linked to a_u and q_u. Some mathematical fits between the latter coefficients have been done in [6], the

most accurate one being:

$$\beta = \left(a - \frac{(a-1)q^2}{2(a-1)^2 - q^2} - \frac{(5a+7)q^4}{32(a-1)^3(a-4)} - \frac{(9a^2+58a+29)q^6}{64(a-1)^5(a-4)(a-9)} \right)^{1/2} \tag{2.32}$$

some tables about those coefficients have been published in [57, 58] for example.

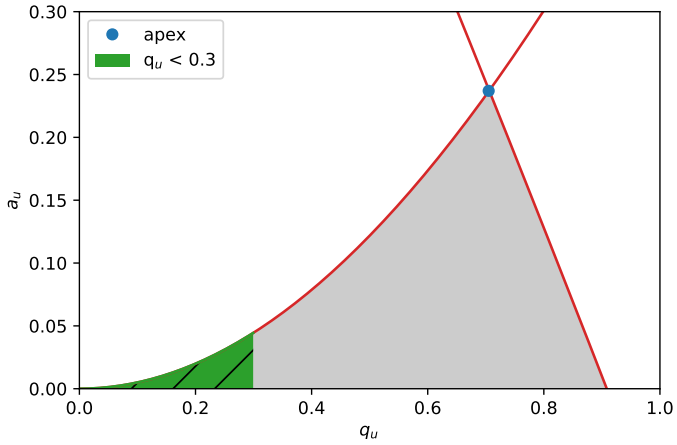

Figure 2.4: Detailed view of the first stability region (shaded in grey), for positive a_u values only.

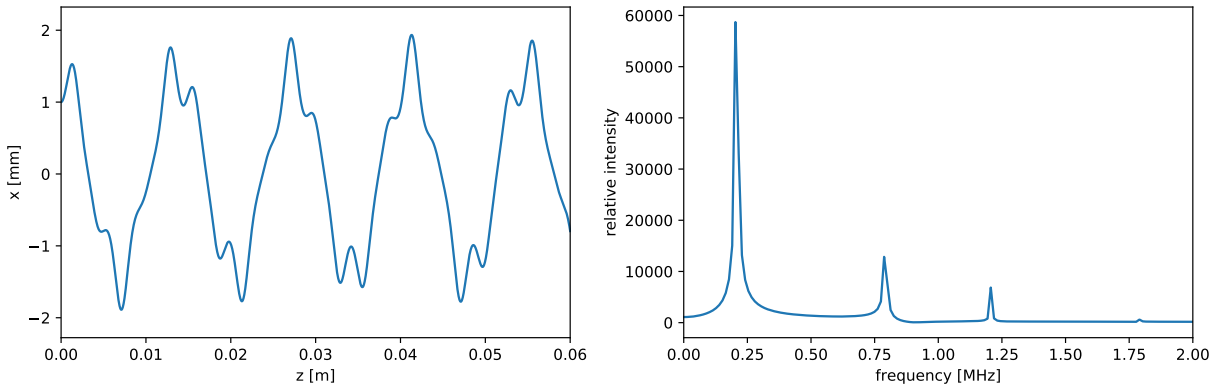

(a) (b)

Figure 2.5: (a) Typical trajectory of an ion in a quadrupole and (b) its associated fast Fourier transform.

A typical ion trajectory is shown in Figure 2.5a and its spectrum is shown in Figure 2.5b. The operating conditions are $(a_u, q_u) = (0, 0.548)$. The RF frequency is $\Omega = 2\pi \times 1$ MHz.

According to the Equation 2.32, $\beta \simeq 0.415$. This means that the frequencies should be: $\omega_0 = 0.207$ MHz, $\omega_1 = 0.793$ MHz, $\omega_2 = 1.21$ MHz, $\omega_3 = 1.79$ MHz, etc. This corresponds well to the frequencies computed with the Fast Fourier Transform (FFT) of the trajectory.

2.1.3 Non-ideal effects and fringing fields

The previous subsection gave an overview of the expected stability regions of a quadrupole. Still, it is based on the asumption that the quadrupole generates an infinite and perfect hyperbolic electric field between its rods. The quadrupoles used in laboratory experiments have a finite length, inducing two major side effects:

1. Some theoretically unstable ions are transmitted.
2. The presence of fringing fields modifies the trajectory of each ion before and after the physical limits of the quadrupole.

The first point will be explained in more details in section 4.2. The main idea is that some unstable ions are transmitted if their instability grows slowly while travelling into the quadrupole. This leads to a decrease in resolution when the quadrupole operates in the mass filtering mode.

The second point deserves to be explained in more details. The electric field does not end abruptly at both ends of the quadrupole: there are fringing fields. An example of this effect is shown in Figure 2.6.

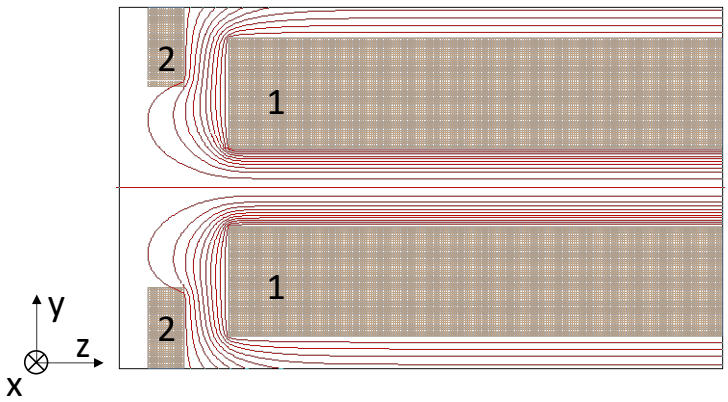

Figure 2.6: Equipotential lines at the extremity of the quadrupole rods, in the yz plane ($x = 0$), showing the presence of fringing fields. The legend is 1: the two opposite rods of the quadrupole having the same potential and 2: an electrode at fixed potential.

Two main studies have modeled and summarised this effect. The paper of Hunter and McIntosh is more theoretical and proposes a mathematical function to model the fringing fields [59]. The one of Dawson is more empirical and draws conclusions about the

consequences of fringing fields on the ions trajectories [60].

As a first guess, it appears that the fringing fields are linearly decreasing from the end of the quadrupole. The work of Hunter and McIntosh has shown that this relation scales more exactly with the function:

$$E_{FF}(x, y, z, t) = \phi(x, y, z, t) \ \left(1 - e^{-az-bz^2}\right) \tag{2.33}$$

with E_{FF} the fringing field in [V/m], $\phi(x, y, z, t)$ the hyperbolic potential in [V] and a and b two numerical constants depending on the distance between the rods and the next element (in [1/m] and [1/m^2] respectively). The position z is considered as starting from the end of the rods and is expressed in [m]. This relation shows that to lower the effect of fringing fields, one could place two metal plates at both ends of the quadrupole, just after the rods. Those endplates should be grounded in order to isolate the system as much as possible.

The fringing fields are inducing a small oscillation of the charged particles before entering into the quadrupole and after their exit. Those oscillations are often measured in number of RF cycles seen by the ion, that number being given by:

$$N_{RF} = \nu_{RF} t_{FF} \tag{2.34}$$

with ν_{RF} the RF frequency in [Hz] and t_{FF} the time during which the ion feels the fringing fields in [s].

Dawson has shown that those small oscillations cancel the phase effect of the quadrupole. With an abrupt potential, the ion trajectory is strongly influenced by the initial RF phase while entering into the quadrupole. This is no more the case with fringing fields. This effect is beneficial for the ion transmission. However, a drawback of those fringing fields effect is that if too many RF cycles are experienced by the ion in the fringing fields region, i.e. if its kinetic energy is too low or if the RF frequency is too high, its trajectory can become unstable. This causes a significant decrease in transmission.

2.1.4 Ion guiding

The first and simplest use of a quadrupole device is as an ion guide. This mode is also called the RF-only mode since in most of the cases, no DC offset is applied to the electrodes. Consequently, the Mathieu coefficient a_u is equal to 0 and the stability is fully determined by the value of q_u. The main interest in an ion guiding system is to know which ions, in terms of masses, are effectively guided by the quadrupole. Taking the definition of the q_u coefficient, it turns out that:

$$\left(\frac{m}{q}\right)_{min} = \frac{4V}{\Omega^2 r_0^2 q_u} \tag{2.35}$$

This means that a certain mass-over-charge ratio is selected if and only if it is above a minimal ratio given by the Equation 2.35: the RF-only quadrupole is actually a high-pass

mass filter. This can be interesting in an experiment if, for example, one wants to analyse the contamination of low masses with respect to the mass of interest. By increasing smoothly the RF voltage, low masses will be less and less transmitted and a change in signal should be observed. Also, by pushing the RF voltage at high values, only higher masses than the one of interest will be guided and their relative amount can be deduced.

In most of the actual ion beam experiments, a quadrupole in RF-only mode is placed just after the ion source in order to guide the ions to the main device (trapping system, interaction region, etc.). There, the RF-only quadrupole can also act as a focusing element, as shown in [61, 62]. This focusing effect will be explicited in the section 4.1.

2.1.5 Mass filtering

The purpose of this subsection is to prove that a quadrupole can act as a mass filter in certain operating conditions. The following discussion is based on the work of Miller *et al.* [63]. The idea is to understand, thanks to a simple qualitative description, the action of the quadrupole mass filter. To simplify the analysis, it is more convenient to distinguish the action of the quadrupole depending on the plane considered (XZ or YZ), each pair of electrodes separately. The considered particles are positive ions: the effect would have been opposite for negative ones.

First of all, the action of the alternating field is the following: during one half of the RF oscillation, the potential is positive, the particle is focused towards the center of the quadrupole. Then, during the next half-period, the potential is negative and the ion is defocused towards the electrode in that plane. Thanks to the alternating potential, the ion is successively focused and defocused, in a stable way if one stays in the stability triangle.

In a second step, one can think about the action of both the DC and RF potential on the ions, depending on their masses. The DC potential is taken positive in the XZ plane and negative in the YZ plane. Considering the XZ plane, a heavy ion will mostly feel an average potential and the RF oscillations will not perturb its trajectory in a significant way. Instead, a light ion will be strongly deflected by the RF oscillations and, if the RF potential becomes too negative, the light ion will crash onto the electrodes of that plane. The electrodes in the XZ plane act as a high-pass mass filter.

If one considers the electrodes lying in the YZ plane, the effect will be opposite. The heavy ions will again be influenced by the mean value of the potential, i.e. the DC potential, but this time it is negative. It means that those ions will feel an average defocusing potential until they crash onto the electrodes. Instead, for the lighter ions, the RF potential will act as a correction potential while positive. The electrodes in the YZ plane act as a low-pass mass filter.

Combining the two previously mentioned effects, one can carefully adjust both the DC

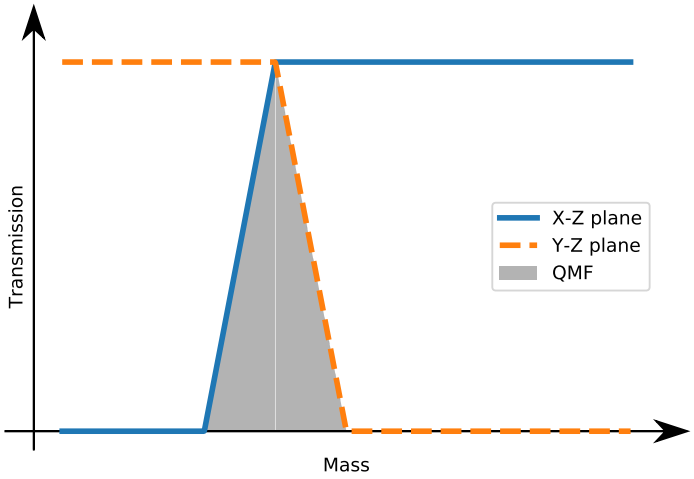

Figure 2.7: Illustration of the mass filtering effect of a quadrupole. This figure is adapted from Fig. 9 in [63].

and RF potentials in order to select a specific mass. One could say that the quadrupole is a *band-pass mass filter*: if the ion is too light, it will be unstable in the XZ plane. If it is too heavy, it will crash onto the electrodes lying on the YZ plane. This band-pass mass filtering effect is illustrated in Figure 2.7. The action of both XZ and YZ planes are represented separately and their combined effect corresponds to the shadowed grey area. In order to operate as an efficient mass filter, one will tend to minimise the range of masses that are passing through the quadrupole but being also careful to keep a sufficient transmission. This key concept of resolution will be discussed in more details in the section 4.2.

In a more practical point of view, the operating conditions under which a quadrupole can operate as a mass filter are given thanks to the stability triangle. Given the Mathieu coefficients a_u and q_u (see Equation 2.26), one can see that masses are scanned along a constant U/V line. The goal of the mass filter is consequently to operate as high as possible on the stability diagram, near the apex of the triangle. The value at the apex is $(a_u, q_u) = (0.237, 0.706)$. The link between (a_u, q_u) and U/V is given recalling the definition of the Mathieu coefficients:

$$\begin{cases} a_u = \frac{8qU}{m\Omega^2 r_0^2} \\ q_u = \frac{4qV}{m\Omega^2 r_0^2} \end{cases} \implies \frac{U}{V} = \frac{a_u}{2q_u} \tag{2.36}$$

At the apex, it gives U/V = 0.1678. This is the ideal mass scan line of a quadrupole. It is represented in Figure 2.8, with several points corresponding to different masses. In the first represented case, the mass selection is perfect. Still, by reducing the slope of the U/V curve, the mass selection becomes worst: this is illustrated with a second slope U/V = 0.16, where 3 masses are selected instead of the desired one only. This can be seen because

$m-2$, $m-1$ and m are all three in the shaded grey region corresponding to the stability triangle of the mass m.

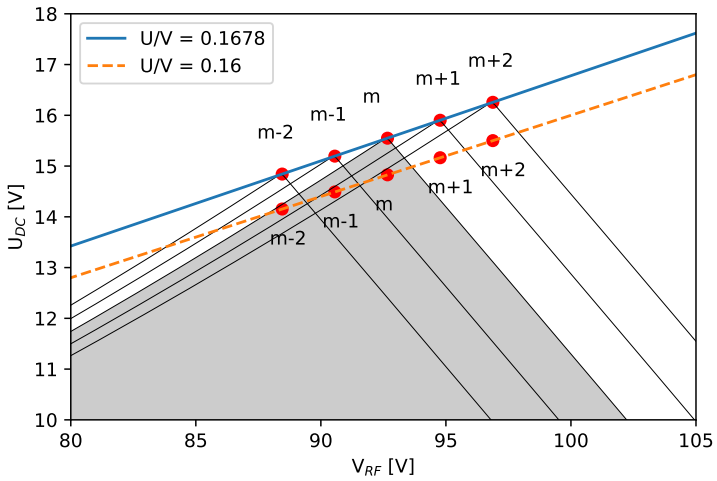

Figure 2.8: Zoom on the top of the stability triangle (in grey - see Figure 2.4), represented in U/V coordinates. Each black line represent the limit of stability for each mass.

2.1.6 Ion trapping

It has been mentioned in section 2.1 that ion trapping is widely performed with a 3D quadrupole device: ions have to be confined in all three directions of space. 2D quadrupoles can be used as ion trapping systems too, thanks to two additional electrodes placed at the entrance and at the exit of the quadrupole. The trapping operation is performed in three steps:

1. The entrance electrode is switched off: ions enter into the quadrupole. The exit electrode has a voltage higher than the kinetic energy of the ions. Consequently, ions are reflected back at the end of the quadrupole.

2. The entrance electrode is switched on, to act as an electrostatic mirror in the same way as the exit one. Thanks to both electrodes, ions will bounce back and forth in the quadrupole.

3. After a certain trapping time, the exit electrode is switched off and the trapped ions will fly away from the quadrupole to reach any other experimental section.

This sequence is represented in Figure 2.9. During the trapping operation, ions will interact together and with the rest gas in the trap *via* two processes. The first one is a simple collisional process that tends to narrow the energy distribution. The second process is a reactive process, where more complex molecules are formed. Also, the addition of a

cold head can allow one to perform helium tagging, which will be briefly discussed in the subsection 2.2.2.

In terms of operating conditions, the purpose is not to be mass selective anymore: one can stay low in the stability triangle. This is even better to keep small DC and RF voltages to prevent wide ions trajectories. Indeed, if the trajectories are too large, the ions will be lost when reflected at one end of the quadrupole.

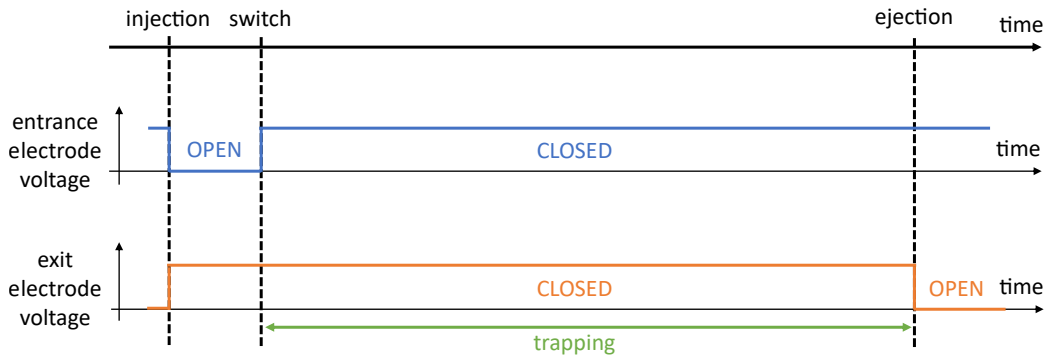

Figure 2.9: Typical timeline of a trapping operation, representing the voltages of the inner and the outer electrodes as a function of one trapping sequence.

2.2 Higher order multipoles and modern setups

2.2.1 Theoretical considerations

All the mathematical developments made in sections 2.1.1 and 2.1.2 have been done by considering the simple equations of motion under the adiabatic approximation, or by considering a simple hyperbolic potential for the quadrupole. In this subsection, the equations of motion for multipolar fields of any order are presented and the existence of a stability diagram is discussed. Again, the derivation is valid for ideal multipolar elements only. In a real experiment, a serie of other effects might appear (misalignment of the rods, fringing fields, non-ideal electrical contact at the rods, etc.). In order to have a better representation of the studied multipoles, a schematic view of an octupole and a 22-pole are given in Figure 2.10.

The potential induced by a series of hyperbolic electrodes uniformly distributed at a distance r_0 from the center is given by solving the Laplace equation. It is often written in polar coordinates [7, 64] and the transformation in cartesian ones gives, for a $2n$-order multipole:

$$\phi(x,y) = \frac{\phi_0}{r_0^n}\left[C_n^0 x^n y^0 - C_n^2 x^{n-2} y^2 + C_n^4 x^{n-4} y^4 - ...\right] \tag{2.37}$$

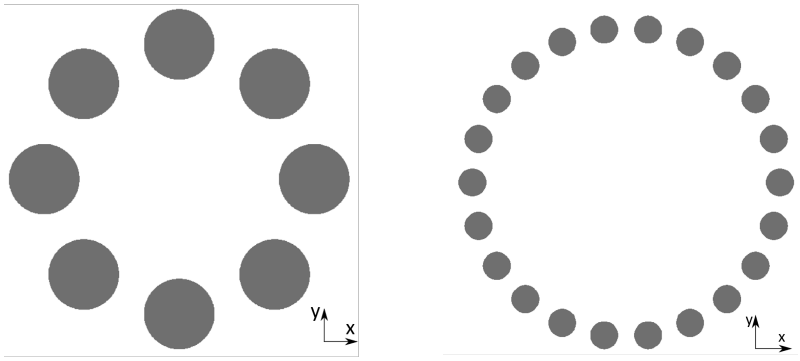

(a) (b)

Figure 2.10: Schematic representations of (a) an octupole and (b) a 22-pole.

where

$$\phi_0 = U - Vcos(\Omega t + \phi) \qquad \text{and} \qquad C_n^k = \frac{n!}{k!(n-k)!} \quad \text{for } k \leq n \tag{2.38}$$

Note that, when $n = 2$, the Equation 2.37 corresponds to the potential in the quadrupole (see Equation 2.20). The equations of motion can then be computed from the general potential and the electric field. By analogy with the eqs. (2.21) and (2.22), one has:

$$E_x = -\frac{\phi_0}{r_0^n}[nC_n^0 x^{n-1}y^0 - (n-2)C_n^2 x^{n-3}y^2 + (n-4)C_n^4 x^{n-5}y^4 - ...] \tag{2.39}$$

$$E_y = -\frac{\phi_0}{r_0^n}[-2C_n^2 x^{n-2}y^1 + 4C_n^4 x^{n-4}y^3 - 6C_n^6 x^{n-6}y^5 + ...] \tag{2.40}$$

and for the equation of motion, the generalisation of the eqs. (2.23) and (2.24) gives:

$$m\frac{d^2x}{dt^2} = -\frac{q}{r_0^n}\left[U - Vcos(\Omega t + \phi)\right]\left[nC_n^0 x^{n-1}y^0 - (n-2)C_n^2 x^{n-3}y^2 + (n-4)C_n^4 x^{n-5}y^4 - ...\right] \tag{2.41}$$

$$m\frac{d^2y}{dt^2} = \frac{q}{r_0^n}\left[U - Vcos(\Omega t + \phi)\right]\left[-2C_n^2 x^{n-2}y^1 + 4C_n^4 x^{n-4}y^3 - 6C_n^6 x^{n-6}y^5 + ...\right] \tag{2.42}$$

As for the quadrupole case, one can find an analogy with the Mathieu equation given the following parameters:

$$\widetilde{u} = \frac{u}{r_0} \qquad \xi = \frac{\Omega t}{n} \qquad a_n = \pm\frac{n^3 qU}{m\Omega^2 r_0^2} \qquad q_n = \pm\frac{n^3 qV}{2m\Omega^2 r_0^2} \tag{2.43}$$

$$\frac{d^2\widetilde{u}}{d\xi^2} + [a_{\widetilde{u}} - 2q_{\widetilde{u}}cos(\xi + \phi)][...] \tag{2.44}$$

where u and $\widetilde{u}$ denote x, y or $\widetilde{x}$, $\widetilde{y}$ respectively. The n coefficient corresponds to a multipolar element made of $2n$-poles. The [...] denotes the adimensional power expansion in x and y

respectively, given in the eqs. (2.41) and (2.42). The Mathieu parameters and equation for the quadrupole ($n = 2$) correspond well to the previously derived one in the subsection 2.1.2. Also, it can be shown (from the Equation 2.15 and by knowing the shape of the electric field) that the adiabatic parameter η, for a $2n$-pole, is written [7]:

$$\eta = q_n \left(\frac{r}{r_0}\right)^{n-2} \tag{2.45}$$

with again, in the case of the quadrupole, $\eta = q_n$. The adiabatic condition $\eta < 0.3$ remains accurate for multipolar elements of any order. However, in the case of higher multipolar fields than the quadrupole, it is impossible to determine a stability diagram. The x and y equations of motion are non-linear and coupled and the solution depends on the initial conditions (position, velocity and phase) of the ion.

Due to this lack of information about the stability of a higher order multipolar element, it is hard to perform efficient mass filtering with them. They are more widely used in ion guiding or trapping. The advantage in using higher order elements lies in the potential shape around the electrodes: the higher the multipolar field, the larger the field-free region. The interest in a large field-free region is that the ion-photon, the ion-ion or the ion-molecule interactions happen without any significant external perturbation.

2.2.2 Cooling versus heating

In some recent experiments, a lot of setups are cryogenically cooled down to temperatures around 4 K or even below. The interest in cooling the ions while trapping them has been already explained in the introduction: it is useful for the fundamental study of ion-molecule reactions. Cooling is also extended further, for spectroscopic measurements, studies of biomolecular ions, etc. The interest there is that due to the complexity of biomolecules, it is much easier to study them when they have a low energy: a smaller number of transitions are observed with a better signal-to-noise ratio.

In order to reach the cryogenic temperatures desired in all those experiments, one has to use the so-called buffer gas cooling technique. A detailed description of this process can be found in [65, 66]. The main idea is to use a buffer gas in a cold cell and to inject the ion beam into it. Helium is especially used as a buffer gas for two main reasons. It is a noble gas, weakly interacting with other molecules and it has a low vapour pressure at cryogenic temperatures. Then, by colliding with the helium atoms, the injected ions will be thermalized and cooled down close to that cryogenic temperature.

In most of the actual experiments, buffer gas cooling is done into the ion trapping system, which is always a $2n$-pole with n higher than 2. Indeed, it has been shown that an ion in a quadrupole can not be cooled down to a few kelvins due to the RF-heating process. The fast micromotion of the ions perturb the collisional processes happening in the trap and therefore hinders the cooling. This effect has been studied for several $2n$-poles

in [67], showing that RF-heating decreases as the order of the trap increases. This is due to the fact that the field free region increases while increasing the number of poles: the micromotion is only visible close to the rods.

In some experiments, one has to find a compromise between the high number of poles and the radial confinement of ions [39]. If an optical access is required, the laser is injected on the axis of the ion beam. Due to the large field-free region of high order multipoles, ions are not confined enough and so the interaction with the laser beam is low, leading to a small output signal.

2.2.3 Actual experiments

As it has been mentioned in the introduction, in the last few years, several experiments have shown the importance of quadrupoles but also higher order multipoles. In this subsection, experiments including two main types of multipoles (octupole and 22-pole) will be explained in more details. Finally, one last innovative concept of ion guiding and trapping will be presented.

Concerning ion spectroscopy, the COLTRAP experiment [34] of Asvany *et al.* is a reference. The central part of the experiment is a cryogenic 22-pole trap, able to reach temperatures of 4 K. They have demonstrated the fact that the helium used as a buffer gas can stick to the injected ions, forming small clusters. This helium tagging can be used as a spectroscopic technique while scanning the frequencies of an IR laser. Indeed, if a rovibrational transition is encountered, the resonance excitation will break the ion-He bond: a loss in the ion-He complex proves the existence of a transition. Another method, called laser inhibition of complex growth (LICG), consists in a competitive process between helium tagging and the interaction of the ion with a laser [68]. The measurement of the ion-He counts provides the spectrum of the excited ion.

In biomolecular analysis, the trend is also to use octupole or 22-pole traps. They are usually coupled with a cold head, aligned with a UV and/or an IR laser in order to dissociate the molecule and analyse its fragments. An example of such a setup is used by Rizzo, Boyarkin *et al.* [39], where their initial 22-pole has been replaced by an octopole [69]. This choice has been made for the previously mentioned reason of ion beam alignment with the laser and because they have observed that RF-heating does not impact the vibrational cooling drastically. Other determinant factors in the choice of an octopole instead of a 22-pole for such an experiment are discussed in the previously cited paper.

Finally, one last innovation deserves to be mentioned: the planar multipole ion trap [66, 70]. This recent kind of ion trapping system differs completely from the previously mentioned multipolar systems in terms of design. It is made of two parallel chips on which the guiding and trapping voltages are applied, as shown in Figure 2.11. Its main advantages are the miniaturisation, the simplicity, the versatility and the reduced cost of such a system.

The first reference, about the design of Wester *et al.*, is about the guiding and trapping of small ions while the second one, referencing a patent submitted by Rizzo *et al.*, aims to analyse large biomolecules. Both techniques seem to be very promising for the future of ion trapping.

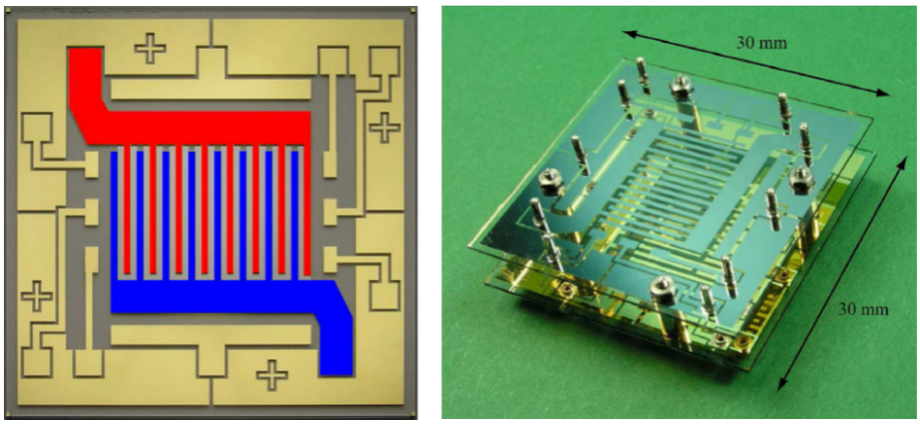

Figure 2.11: Top view and picture of a planar trap design. Fig. 7 in [66].

Chapter 3

General simulations on the quadrupole

The goal of this chapter is to apply the formalism of Mathieu equation derived in subsection 2.1.2 to the quadrupole A, which will be used in the future experimental setup.

This will be done thanks to simulations: there are key points which need to be evaluated before getting to the laboratory. In fact, it allows one to have a first idea about the performances of the real setup. It also imposes constraints on the operating parameters that have to be reached by the electronics.
In this work, the quadrupole A has been modeled and its performances have been simulated thanks to two different softwares. Firstly, with SIMION [71], which is a powerful simulation tool widely used in ion optics. Secondly, a *Python* code (version 3.0) has been written in order to compare and put into perspective the results obtained with SIMION. That comparison provides also a better understanding of the setup and further possible updates. This chapter introduces all the simulation formalism and discusses the basics of the quadrupole stability.

3.1 Modelisation

3.1.1 Studied setup

First of all, the quadrupole A has been drawn according to its real dimensions. This has been done in SIMION thanks to *Geometry Files* (`.GEM`) (see Appendix I in [71]) because of the versatility and the accuracy of such an approach. Also, the symmetry of the quadrupole has been used to spare some memory. In the performed simulations, each grid unit (gu), i.e. the mesh, corresponds to 0.25 mm. The final `.GEM` file used to draw the quadrupole is given in Appendix B. The drawn and real quadrupole are shown in Figure 3.1. Its main dimensions are given in the Table 3.1.

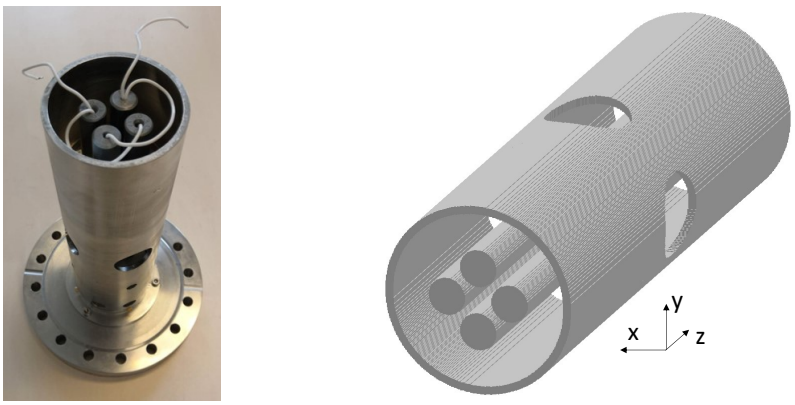

(a) (b)

Figure 3.1: (a) Picture of the quadrupole device that will be used in the future laboratory experiment, mounted on a flange and with its connectors (white wires) and (b) schematic representation of the quadrupole A.

Table 3.1: Summary of the main dimensions of the quadrupole A. All numerical quantities are given in mm.

Length	radius of the rods	free space radius	outer cap radius
200	6.3	4.5	32

In a real experiment, there are additional elements next to the quadrupole: it is placed after the skimmer and surrounded by two electrodes. Those elements are represented in Figure 3.2. Starting from the left of the figure, one can distinguish the skimmer, directly mounted on an electrode (number 3 in Figure 3.2) to perform the extraction. This is the link between the valve and the whole experiment. Then, a second electrode (4) has been added to optimise the ion focusing and achieve a good injection of the ion beam into the quadrupole. The quadrupole system is surrounded by two electrodes (5 and 6) to perform, for example, ion trapping.
The only important parameter to keep in mind concerning the skimmer is its radius of aperture: $r_s = 1.25$ mm. Several different skimmers are available in the laboratory but the currently used one has that radius r_s. The aperture of the electrode ($r_{elec} = 12$ mm) is much greater than the free space radius of the quadrupole ($r_0 = 4.5$ mm).

3.1.2 Simulation parameters

In the simulations, the quadrupole transmission will be studied for several operating conditions in terms of electrical parameters, extraction voltages, etc.
The quadrupole transmission is also highly dependent on the ion distribution in space and velocity. In the laboratory, ions are produced in a supersonic expansion. Consequently, the ions will have a velocity distribution given by a Maxwell-Boltzmann distribution. In

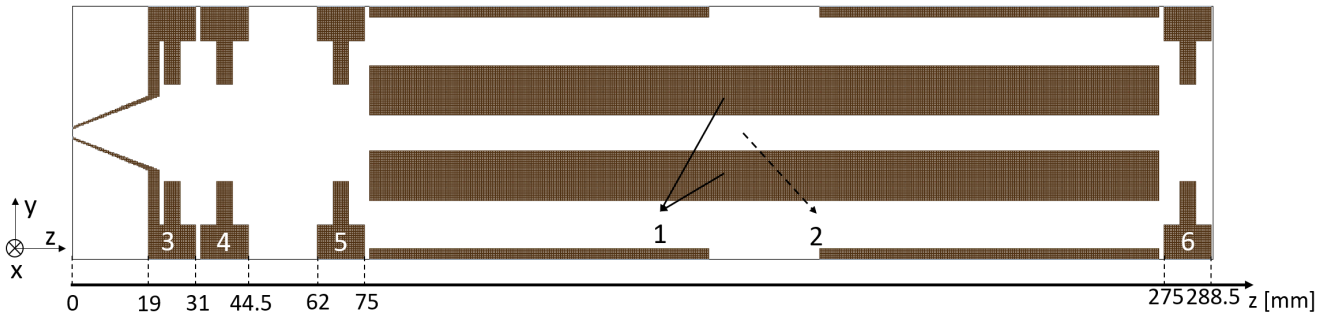

Figure 3.2: Cut view of the different elements of the simulated setup in SIMION. Each number represents an electrode (1 and 2 being the rods of the quadrupole, the rods 2 are not visible given the cut).

SIMION, this distribution has been approximated by a gaussian one. The mean velocity, 600 m/s, corresponds to the mean velocity of a jet of argon. Here, the goal is to deal with CO_2 instead of Ar, but the carbon dioxide supersonic jet is seeded in Ar: this is why a mean value of 600 m/s is used. The full width at half maximum (FWHM) of the ion beam has been put at 100 m/s, i.e. 26 K around the mean velocity. This is a typical enlargement for such a jet. All the parameters related to the ion distribution are given in Table 3.2.

Table 3.2: Main parameters of the ion distribution at the skimmer.

Spatial distr. (radius)	Velocity distr.	Mean velocity	FWHM velocity	# ions	m/z ratio
Uniform circular (1.25 mm)	Gaussian	600 m/s	100 m/s	1000	44

Regarding the electronics, a few parameters can be varied. They are mainly the skimmer and electrodes voltages for the first part of the setup. Moving to the quadrupole, one can adjust the RF and DC voltages, the frequency and the phase of the oscillating potential. The voltage of both surrounding electrodes can be specified too. After a first discussion with the electronic workshop, the RF frequency has been taken at 1.2 MHz. The other parameters will be specified depending on the simulation set.

3.2 First simulations

3.2.1 Extraction voltage

The first simulation that has been done is regarding the extraction voltage of the skimmer and the electrodes (3) and (4). The ions coming from the supersonic jet have a low kinetic energy: it stands around $E_{kin} = 0.082$ eV (see Table 3.2). This kinetic energy is not sufficient to inject the ions into the quadrupole efficiently. They will be reflected, they will

oscillate in an unstable manner: the ion guiding is, generally speaking, difficult to handle. A minimal extraction voltage has to be applied to the first set of electrodes in order to focus and inject the ions properly into the quadrupole.

In order to analyse the effect of this extraction voltage, one has to be in a highly stable position in the stability diagram and, by increasing the extraction voltage, transmission should increase at the exit of the quadrupole. In this case, the couple of DC/RF voltages is at (U,V) = (8,80), i.e. $(a_u, q_u) = (0.122, 0.610)$. This point is indicated on a stability triangle in Figure 3.3a. This is low in the stability diagram compared to the operating condition of the mass filter mode, i.e. the apex of the triangle. The choice in this operating condition is justified by the fact that one wants to observe the effect of the extraction only, not any instability that might appear because of an almost unstable operating point.

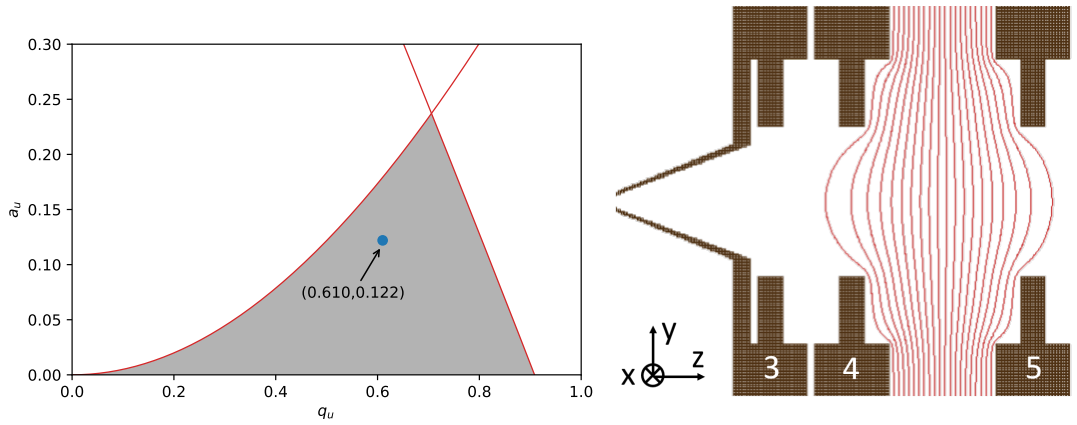

(a) (b)

Figure 3.3: (a) Operating point in the stability diagram for which the extraction voltage has been analysed and (b) equipotential contours for a non-zero extraction voltage on electrodes (3) and (4). The same cut view as in Figure 3.2 has been done.

In Figure 3.3b, a set of equipotential lines are represented, showing the smooth potential decrease between electrodes (4) and (5) (see Figure 3.2 for the corresponding legend). This potential decrease will induce both acceleration and focusing on the skimmed ions.

The Figure 3.4 summarises the results from the previously mentioned scan. One can observe a quick increase in transmission from 0% (without extraction) to 100% (around 1 V). Two cases have been simulated: the first simulates the extraction with a certain voltage applied to the electrode (3) and the second case simulates the extraction with the same voltage applied to both electrodes (3) and (4). In that second case, the voltages have been taken as equal for both electrodes. Two main parameters are impacting the transmission: the fringing fields and the focal length of the electrostatic lens corresponding

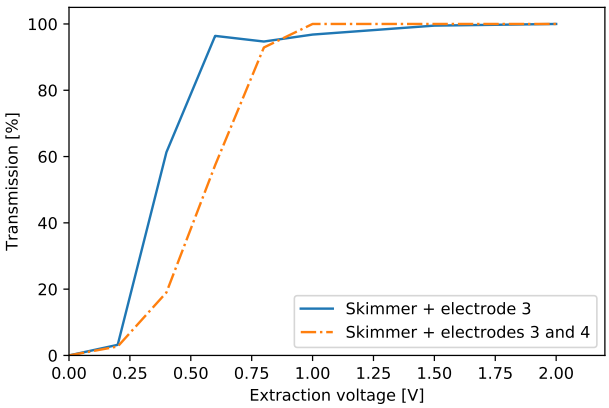

Figure 3.4: Transmission through the quadrupole as a function of the extraction voltage (applied to the skimmer system in Figure 3.2).

to the "skimmer + electrodes" system.

For an extraction voltage of 1 V, the outgoing ion beam remains highly divergent: the ions are strongly deflected in output because of the fringing fields. The divergence is reduced with a higher extraction voltage because the ions will spend less time in the fringing fields region (they have a higher kinetic energy) and therefore will be less deflected at both the entrance and the exit of the quadrupole. An extraction voltage of 2 V for both the electrodes (3) and (4) has been selected as reference for the next simulations. It gives a good compromise between the acceleration of the ions and the divergence of the outgoing beam.
With that extraction voltage, both curves (i.e. with or without the electrode (4) after the skimmer) are transmitting all ions. The powering up of the electrode (4) is only modifying the focal point of the equivalent electrostatic lens.

3.2.2 Divergence, beam size and focusing effects

One important approximation has been done so far regarding the ion beam distribution: it has been considered uniform in space, i.e. perfectly aligned and collimated. Experimentally speaking, this is not necessarily the case: the skimmer induces a certain beam divergence or anyway does not give a perfectly collimated ion beam as an output. Numerical studies [72, 73] about the effect of a skimmer similar to the one used in the laboratory show that the ion beam size is larger after passing through the skimmer, but this enlargement is stable: it is not divergent. A qualitative transmission analysis has been done for a set of distributions, by varying the radius and the divergence angle of the input distribution. Still, as long as the electrodes induce a focusing effect on the ion beam, a perfect transmission is kept until highly divergent and/or large beams. For example, in the (unfavourable) case of a divergence half-angle of 5° for a beam radius of 3 mm, the transmission is still maximal

for the $(U, V) = (8, 80)$ conditions.

Thanks to the strong focusing effect, the optimal distance between the quadrupole and the skimmer can be determined: it will correspond to the focal length of the electrostatic lens associated to the "skimmer+electrodes (3) and (4)" system. According to the simulations made on SIMION with an acceleration voltage of 2 V, the beam is focused at a distance $f \simeq 6.77$ cm from the tip of the skimmer. This is why, for that potential and considering the setup in Figure 3.2, it is convenient to put the second electrode to the same acceleration voltage: the focal length is closer to the entrance of the quadrupole. Without the second electrode, the focal length is smaller ($\simeq 4.1$ cm) and so the beam diverges much more while entering into the quadrupole.

All those notions of divergence and beam size are related to the acceptance of the quadrupole. It corresponds to all the points in phase space that lead to a stable transmission through the quadrupole for a certain operating condition. The acceptance can be determined thanks to the operating conditions and the ion distribution parameters. Numerous studies have investigated this acceptance problem [6, 64, 74, 75]. It turns out that it is highly dependent on (a_u, q_u) but also on the initial RF phase seen by the ions.

As long as the supersonic jet is non-uniform in space and time, it is hard to control the phase at which the ions enter into it: the ion bunch is usually longer than one RF cycle. Also, as it has been explained in the subsection 2.1.3, the fringing fields cancel out the phase effect on transmission. The acceptance should be computed anyway for a specific (a_u, q_u) operating point and several phase angles. This can be simulated for example thanks to the matrix method. This method is based on the same idea as the ABCD matrix in light optics but transposed to the study of ion optics. It is based on phase space dynamics. More details about this method can be found in [74, 76, 77].

The effects of both the focusing and the acceleration voltage can be seen in Figure 3.5a and Figure 3.5b respectively. Those figures show the spatial and velocity distributions at the skimmer (hashed blue) and at the focal point (orange) respectively. Instead of speaking about velocities, one should speak about speed: the represented quantity is the norm of the velocity vector, taking into account the small x and y components at the focal point.

The velocity distribution after the extraction is obtained by supposing that the electric potential is perfectly transferred into kinetic energy and added to the initial kinetic energy of the ion. It turns out that:

$$\begin{aligned} E_{kin,extr} = E_{kin,init} + E_{elec} \quad &\Longrightarrow \quad \frac{mv_{extr}^2}{2} = \frac{mv_{init}^2}{2} + qV \\ &\Longrightarrow \quad v_{extr} = \sqrt{v_{init}^2 + \frac{2qV}{m}} \end{aligned} \tag{3.1}$$

with q the charge in [C], V the acceleration voltage in [V], m the mass in [kg] and v the

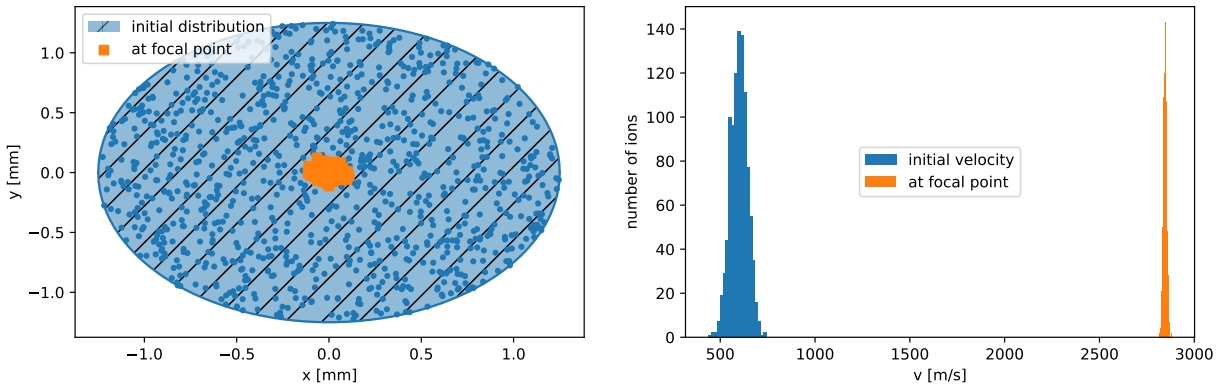

(a) (b)

Figure 3.5: (a) Spatial and (b) velocity distributions before extraction and at the focal point of the extraction system.

speed in [m/s]. For an extraction voltage of 2 V, it gives $v_{extr} = 3022$ m/s. As it can be seen from the simulation in Figure 3.5b, the central value is located around $v_{focal} \simeq 2850$ m/s: it can be deduced that, at the focal point, around 6% of the energy transfer is not achieved yet. Indeed, the potential value at the focal point is still equal to 0.23 V on the main axis, the total energy transfer will be achieved at the center of the electrode (5).

One final comment can be made regarding the extraction voltage. Indeed, it might seem quite low given the standard high voltages used in ion optics, for example in time-of-flight experiments, gating/bunching units, etc. Scientists do not agree on the strategy to adopt, some advocating for a high extraction voltage and others for the lowest possible one [66]. It actually strongly depends on the experimental setup, on the operating conditions (for example in terms of pressure), on the desired resolution, etc. Three main arguments can be made to defend the low extraction point of view.

Firstly, by analysing other papers and experiments of the same kind. According to the theory and some experimental setups developed by Gerlich *et al.*, following the formalism in the simulations of Taylor *et al.* and some other papers (see for ex. [75]), it turns out that an extraction voltage of 2 V is consistent. The objective of this experiment is to be as flexible as possible: the same quadrupole device will be used as an ion guide, as a mass filter or as an ion trapping system depending on the experiment. In the case of mass filtering for example, it will be shown in the section 4.2 that the resolution evolves in $R \propto 1/E_{kin}$. Because of that, a small voltage must be applied at the extraction.

Secondly, one can think about the collisions experienced by the ions with the residual gas in the chamber. When accelerated, the ions heat up by colliding with that gas: this effect has to be avoided (or anyway minimised) to keep the produced ions at a small temperature.

This has to be confirmed in the laboratory experiment.

Thirdly, one last great advantage of a low kinetic energy stands in the transit time of the ions in the quadrupole. The purpose of this experiment being the analysis of rovibationnal spectra produced thanks to laser photodissociation, a longer transit time implies a longer possible excitation of the ions. A small kinetic energy is consequently required in order to perform continuous excitation (see section 5.3).

3.3 Reconstruction of the stability triangle

Besides the extraction voltage, another important characteristic of the quadrupole is its stability region. The quadrupole should operate in the stability triangle, given a certain DC and RF voltage and given a certain RF frequency.

According to the theory previously derived (see subsection 2.1.2), an ion will have a stable trajectory if the operating condition of the quadrupole stays between the $-a_0$ and b_1 curves, representing the limits of the stability triangle. It has been shown in subsection 2.1.5 that U/V slopes correspond to $a_u/2q_u$ slopes on the stability diagram. The maximal slope passes through the apex of the triangle, which has the following coordinates: $(a_u, q_u) = (0.237, 0.706)$. This means that the maximal slope giving stable trajectories is U/V = 0.1678. In order to reconstruct the stability triangle effectively, scans have been performed, using SIMION, along constant U/V slopes. The result of those scans are represented on both a 2D and 3D view for different slopes in Figure 3.6. On the 2D view, only points with a transmission above 1% are represented.

As a first observation, one can say that the stability triangle is, in general, well reconstructed: the quadrupole A correctly follows the theory. However, by looking carefully to the limits of stability, it can be observed that the match is not perfect. This is partly due to the spacing of each considered operating condition: a finer scan on each U/V slope should be performed near the limit of stability. Still, another more significant effect can be observed. The stability points seem to be "shifted" to the left with respect to the theoretical triangle. The simulated apex is equal to $(a_u, q_u) = (0.231, 0.688)$ instead of $(a_u, q_u) = (0.237, 0.706)$ in the theory and the extreme q_u value is $q_u = 0.872$ instead of $q_u = 0.904$. Two hypotheses have been made to explain this shift:

1. SIMION tends to underestimate the r_0 due to the grid definition: a finer grid should be used to approach the exact value.

2. The potential form between the rods is not exactly hyperbolic due to the fact that round rods are used instead of hyperbolic ones. The Mathieu equation is not exactly describing the ion motion.

Firstly, the grid size has been increased to 10 gu/mm (gu = grid unit), in order to check the validity (or not) of the first hypothesis. The obtained stability triangle was identical to

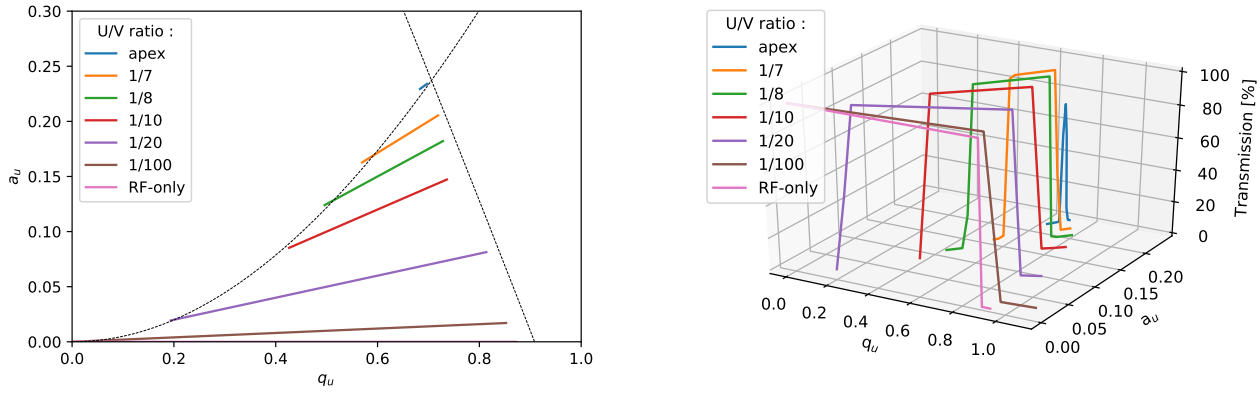

(a) (b)

Figure 3.6: Reconstruction of the stability triangle of the quadrupole A thanks to simulations in SIMION. (a) 2D representation with the dotted black line corresponding to the theoretical stability limit (see eqs. (2.29) and (2.30) in subsection 2.1.2). Only points above 1% of transmission are represented. (b) 3D representation of all the simulated conditions.

the previous one: the shift was present. One can conclude that SIMION works perfectly well even with a grid size of 4 gu/mm.

To check the validity of the second hypothesis, it is interesting to go back to the early work of Denison [78]. In that work, widely cited by all scientist performing simulations on quadrupoles, Denison specifies that the potential due to rounds rods is actually different that the one produced by hyperbolic rods. The solution of the Laplace equation for the potential has to be written as a serie expansion:

$$\phi = (U - V cos\,(\Omega t)) \sum_{m=0}^{\infty} C_m \left(\frac{r}{r_0}\right)^m cos\,(m\theta) \qquad \text{with} \qquad \theta = atan(y/x) \tag{3.2}$$

Given the symmetry of any multipolar system, the potential changes sign when θ changes by $\pi/2$. It implies that:

$$cos\left(m\frac{\pi}{2}\right) = -1 \Longrightarrow m = 2(2n+1) \qquad \text{with} \qquad n \in \mathbb{N} \tag{3.3}$$

Consequently, m is restricted to a set of values given by $m = 2, 6, 10, 14....$ Therefore, Equation 3.2 can be also written:

$$\phi = (U - V cos\,(\Omega t)) \sum_{n=0}^{\infty} C_n \left(\frac{r}{r_0}\right)^{2(2n+1)} cos\,(2(2n+1)\theta) \tag{3.4}$$

The Mathieu equation is adapted accordingly and becomes coupled along both x and y

directions:

$$\frac{d^2x}{d\xi^2} = -[a_u - q_u cos(2\xi + \phi)] \sum_{n=0}^{\infty} C_n(2n+1) \left(\frac{x^2+y^2}{r_0}\right)^{2n} \times [xcos(2(2n+1)\theta) + ysin(2(2n+1)\theta)] \quad (3.5)$$

$$\frac{d^2y}{d\xi^2} = [a_u - q_u cos(2\xi + \phi)] \sum_{n=0}^{\infty} C_n(2n+1) \left(\frac{x^2+y^2}{r_0}\right)^{2n} \times [ycos(2(2n+1)\theta) - xsin(2(2n+1)\theta)] \quad (3.6)$$

with a_u, q_u the Mathieu coefficients. This coupling makes the resolution of the system more complex. Equation 3.5 and Equation 3.6 correspond well to the Mathieu equation if $C_0 = 1$ and the other coefficients are equal to zero.

The key point is to be able to determine the value of each C_n coefficient for any system. A lot of studies have investigated this problem, tending to optimise the r/r_0 ratio that gets rid of higher order terms. Those studies have been chronologically done by Dayton (1954) [79], Paul (1958) [80], Lee-Whiting (1971) [81] and Denison (1971) [78]. The optimal ratios are slightly different depending on the studies and depending on the numerical precision considered in each case. The most satisfactory result in terms of numerical precision is r/r_0 = 1.1468. With that radius, the C_1 term tends to zero.

The latest simulations performed by Gibson and Taylor (2001) [10] suggest that the ideal ratio is between r/r_0 = 1.125-1.13. This ratio does not eliminate the 6^{th} order term and so does not minimise the non-quadrupole behaviour. The interest in that value lies in the behaviour of the quadrupole as a mass filter: that ratio of $r/r0 \simeq 1.127$ provides, theoretically, a better mass selection and a better resolution.

In the quadrupole A, the ratio is equal to $r/r_0 = 1.4$: this is much larger than the ideal ratio. This means that the potential between the rods does not correspond to the one of hyperbolic rods, i.e. the one considered in the Mathieu equation: it contains also higher order potential contributions, corresponding to a 12-pole, a 20-pole, etc. Anyway, it is clearly specified by Denison that whatever the r/r_0 ratio, a stability diagram still exists for any quadrupolar system with round rods. This diagram is simply shifted depending on the ratio.

This conclusion is really important for two reasons. First of all, it explains why the stability triangle of the quadrupole A is shifted with respect to a hyperbolic case. Secondly, it allows to compare the performances of the quadrupole A with quadrupoles B and C and find how to optimise the setup in the future.

3.4 Comparison with an ideal setup

In this section, the conclusion drawn about the non-ideal behaviour of the quadrupole is illustrated: firstly, the C_n coefficients are computed and secondly, the previously computed

stability triangle is compared with two other cases: quadrupole B and quadrupole C.

3.4.1 Computation of the C_n coefficients

The method used in order to derive the C_n coefficients of the quadrupole A is the following:

1. Potential files have been generated directly from SIMION to `.PATXT` files, managed with a *Python* script.

2. A perfect hyperbolic potential has been generated in the script, in order to compare it with the one from SIMION and compute their relative differences.

3. A least square fit has been done along the x-axis of the quadrupole to derive the C_n coefficients.

A contour plot of each system is shown on figs. 3.7a and 3.7b. As a first observation, it is hard to distinguish a significant difference in both potential shapes between the electrodes. The relative difference between both potentials is represented on figs. 3.7c and 3.7d. The difference between both systems is smaller than 4% in most of the regions. It increases from zero at the rods to a maximum value around $0.5r_0$ and decreases then until the center of the quadrupole, as represented in Figure 3.7d.

To translate mathematically the difference in potential between both systems, one has to compute the C_n coefficients related to the quadrupole with round rods. A least-squares fit method has been used in that purpose and the result is presented in Figure 3.8a. As a first guess, the fit, the hyperbolic potential and the SIMION data seem to overlap, but a zoom on the curve shows that this is not exactly the case: the least-squares fit and the data from SIMION match perfectly while the hyperbolic potential is slightly smaller. The fit has been done by considering four C_n coefficients, from C_0 to C_3. Their values are given in Table 3.3.

In Figure 3.8b is represented the relative difference between the fit and the data obtained thanks to the potental file from SIMION. It can be observed that the fit is accurate up to a relative precision of $4\ 10^{-6}$. This means also that the found coefficients are coherent and can be compared with other studies. The value of C_0 seems to be in adequation with other papers [78, 82] but the C_1 value seems a little bit overestimated. No precise data about higher order coefficients have been found in the literature.

Table 3.3: Summary of the C_n coefficients found with the least-square fit on the potential of the quadrupole A.

C_0	C_1	C_2	C_3
1.02	-0.017	$8\ 10^{-3}$	-0.012

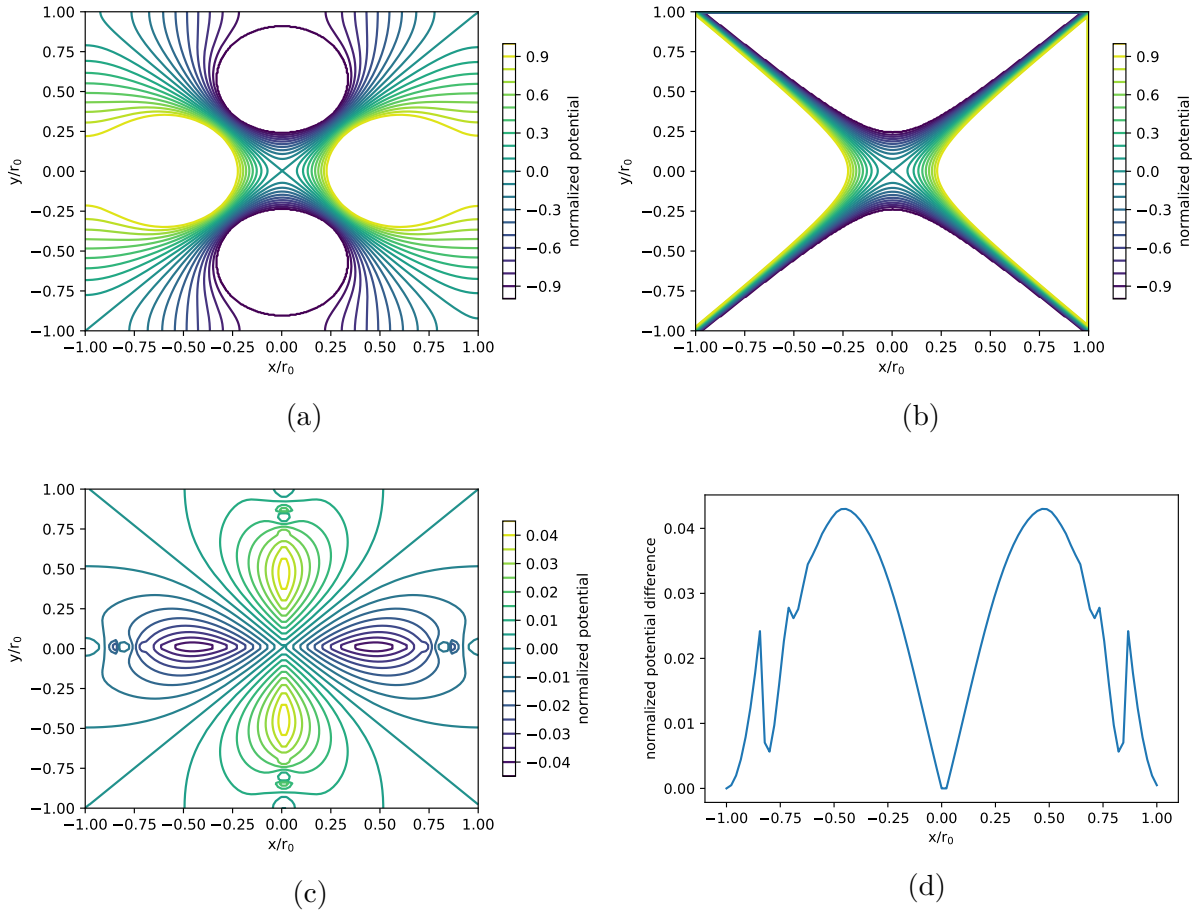

Figure 3.7: Contour plots of the potential in the XY plane of 2 quadrupolar systems. (a) the quadrupole currently used in the lab and (b) the hyperbolic case. (c) Difference of the potentials represented in (a) and (b) and (d) the latter difference taken along the x-axis ($y = 0$).

Finally, besides the discussion about the ideal r/r_0 ratio that gets rid of the C_1 term, another solution developed in some papers is to add an octopole or an hexapole field to the quadrupole one. Those fields acts as correcting contributions cancelling the higher order terms. This has been widely studied by the group of Douglas *et al*. It turns out that under some conditions, a quadrupole with added octopole or hexapoles fields display better performances that the quadrupole field only [83, 84, 85].

3.4.2 Comparison of three stability triangles

As long as a stability triangle exists for each r/r_0 ratio, it is interesting to compare the one of the quadrupole A with two other cases. Firstly, again in SIMION, with the quadrupole B: it has the same r_0 but a different radius r for the electrodes, in order to obtain the

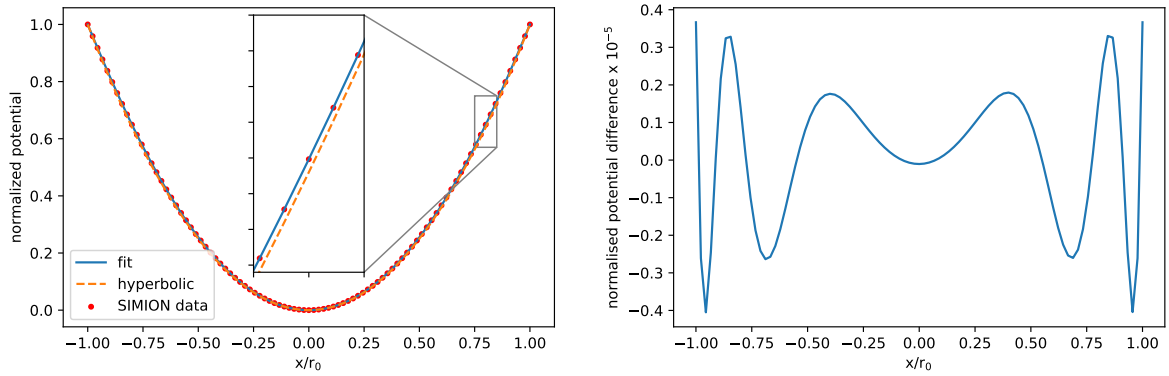

(a) (b)

Figure 3.8: (a) Fit of the potential along the $x-$axis (normalised with r_0). The difference with the ideal hyperbolic potential is clearly shown on the zoom. (b) Difference between the fit and the data from SIMION.

ideal ratio $r/r_0 = 1.1468$. Secondly, a *Python* script has been written to have another comparison point: this corresponds to the quadrupole C. This script is constructed as follow (inspired by Taylor *et al.* [8]):

1. All the quadrupole and ions parameters are specified. Another script has been used to generate several ion distributions (uniform, gaussian, etc.).

2. The Mathieu equation is solved thanks to a Runge-Kutta method of 4^{th} order (with `solve_ivp` in the *scipy_integrate* package).

3. The obtained data is treated, displaying the desired output (ion trajectories, transmission, stability, etc.).

As a first result, it is interesting to analyse and compare a simple ion trajectory in all three cases. The ion has been taken at a starting position $(x, y, z) = (0.1\ r_0, 0.1\ r_0, 0)$ mm, the origin being at the central point between the electrodes and z being the direction of propagation of the ion. In terms of electronics, the frequency is set to $\nu = 1$ MHz, the phase is set to $\phi = 0$ in $t = 0$ and the voltage combination is (U,V) = (0,15).

The results of that simulation are shown in Figure 3.9. It is clear that the trajectory along the quadrupole A is different than the one along the quadrupole C allowing to use the Mathieu equation. Indeed, the oscillation amplitude is roughly the same in each case, but the oscillation frequency is different. There is a shift of the ion trajectory in the quadrupole A with respect to the quadrupole C. On the other hand, the ion travelling in the quadrupole B simulated in SIMION has a similar trajectory to the one from the Mathieu equation. This shows again that, because of a difference in the r/r_0 ratio, the potential form in the quadrupole A presents higher order contributions than the pure hyperbolic case (quadrupole

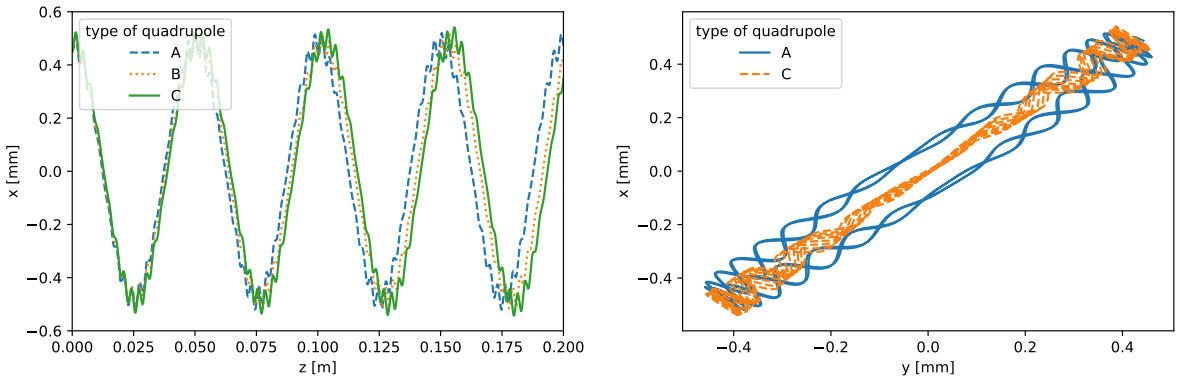

(a) (b)

Figure 3.9: Comparison of an ion trajectory along the quadrupole with respect to the (a) x axis and in the (b) xy plane. The trajectory of the quadrupole B has not been displayed in (b) for a better clarity.

C).

As a second step, the stability triangle has been reconstructed with the quadrupole B in SIMION and the result is shown in Figure 3.10. The same simulations have been done with the homemade *Python* script for quadrupole C and the resulting triangle is shown in Figure 3.11.

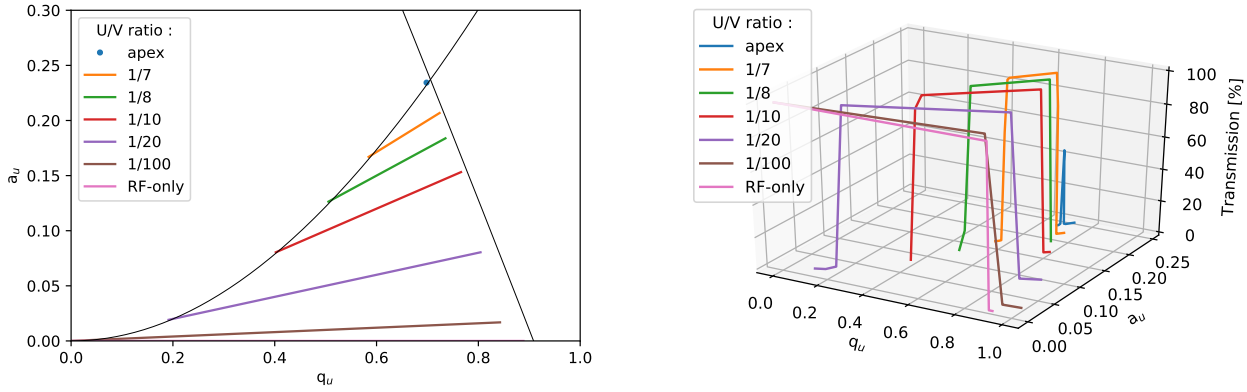

(a) (b)

Figure 3.10: Reconstruction of the stability triangle corresponding to the ideal r/r_0 ratio (quadrupole B). (a) 2D representation, the dotted black line corresponding to the theoretical stability limit. (b) 3D representation of the whole scan.

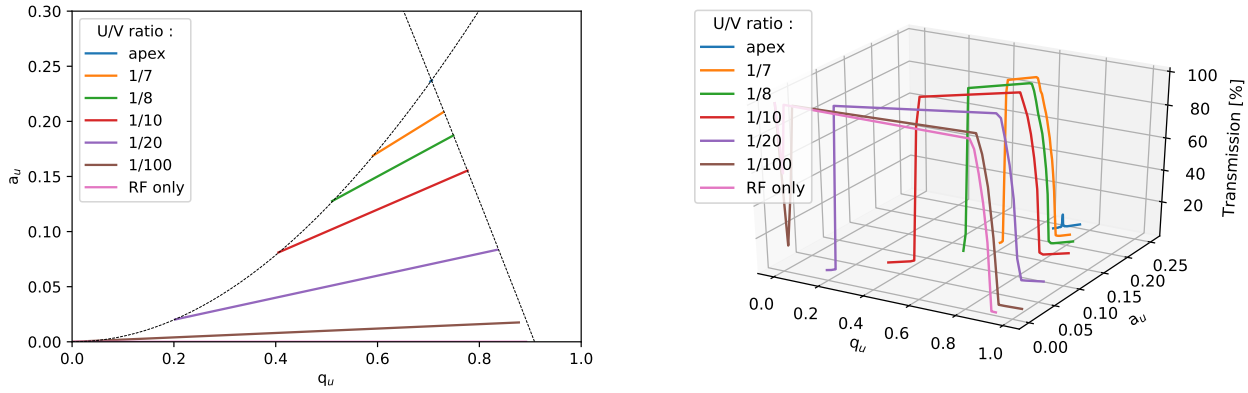

(a) (b)

Figure 3.11: Reconstruction of the stability triangle thanks to the *Python* script solving Mathieu equation. (a) 2D representation, the dotted black line corresponding to the theoretical stability limit. (a) 3D representation.

It can be observed on the Figure 3.10 that the quadrupole B (i.e. the one with $r/r_0 = 1.1468$) simulated in SIMION fits much better with theory than the quadrupole A. It remains a little bit shifted at some points, but this is mostly due to the sampled points of the scan. The shift is clearly smaller than for the quadrupole A. As an example, it is interesting to compare the apex of each system. In the quadrupole A, the simulated apex is located in $(a_u, q_u) = (0.231, 0.688)$ while in the quadrupole B, it is in $(a_u, q_u) = (0.234, 0.698)$. This difference is small but non-negligible. As a reminder, the apex given by the Mathieu equation (which is the apex obtained for the quadrupole C) is $(a_u, q_u) = (0.237, 0.706)$.

3.5 Discussion

In this chapter, a first approach of the quadrupole A has been done by analysing its behaviour thanks to SIMION. The simulation formalism has been presented, with all the specific parameters of the studied system. A sensitivity analysis on the extraction voltage and on the divergence of the ion beam has been done, showing that the system is robust for a wide range of input distributions. If the ion beam shape is worst than expected (highly divergent for example), the extraction voltage could be increased, but this presents some disadvantages, the main one being a decrease in mass resolution (see section 4.2). The stability triangle of the quadrupole A has been reconstructed, showing a small shift with respect to the theory. This shift has been understood by looking more carefully to the shape of the electric field induced by the rods, which is not exactly hyperbolic: it contains higher order terms. Those higher order contributions have been quantified thanks to the C_n coefficients of the electric field expansion. The latter explanation for the shift has been validated given two other simulations. The first one was with SIMION but by changing the

r/r_0 ratio (quadrupole B), in order to reproduce the hyperbolic potential with round rods. The second one was with a *Python* script solving the Mathieu equation (quadrupole C).

Thanks to those studies about the general behaviour of the quadrupole, one can investigate its performances with a better understanding of the underlying process. This has been done in three particular operating modes: the ion guiding, the mass filtering and the ion trapping.

Chapter 4

The performances of the quadrupole A in three operating modes

The purpose of this chapter is to show that, combining the theory and the first simulations, the quadrupole A, that will be used in a further laboratory experiment, is able to act as an ion guide, as a mass filter and as an ion trapping system. This will be done thanks to simulations in SIMION and *Python*. The laboratory experiment aims to measure rovibrational spectra of CO_2^+ ions and $[(CO_2)_m\text{-}(H_2O)_n]^+$ complexes. Therefore, the masses of 44, 62, 80, 98 and 116 amu are typically used in the following simulations. As a first study, the number of CO_2 molecules has been kept at one and only the number of H_2O molecules has been increased.

The conditions under which it is possible to guide, filter or trap ions are discussed. The performances of the quadrupole, especially the resolution in the mass filter mode, are shown with a set of simulations outlining the effect of several experimental parameters. Finally, the *Python* script is extended to simulate ion trajectories in any multipolar device.

4.1 The quadrupole as an ion guide

As it has been explained in the state of the art (see subsection 2.1.4), the quadrupole acts as an ion guide in RF-only mode or with a low DC voltage: the purpose of the guide is, by definition, to let a large range of ions fly through it. This is achieved by staying low in the stability triangle. Given the extreme q_u value found in section 3.3, it turns out that the maximal RF voltage to transmit masses greater than 44 amu (singly charged) is $V \simeq 114$ V (for a frequency of 1.2 MHz). To have a more accurate extreme value, the RF voltage has been finely scanned around 114 V. The result of the simulation can be seen in Figure 4.1a. The transmission remains at 100% up to 113.9 V, just before the critical value. The same kind of scan has been done on masses with an RF voltage of 113.9 V and the result of the simulation is represented in Figure 4.1b. It shows that a mass below 44 amu will not be selected for that voltage: the ion guide works as expected.

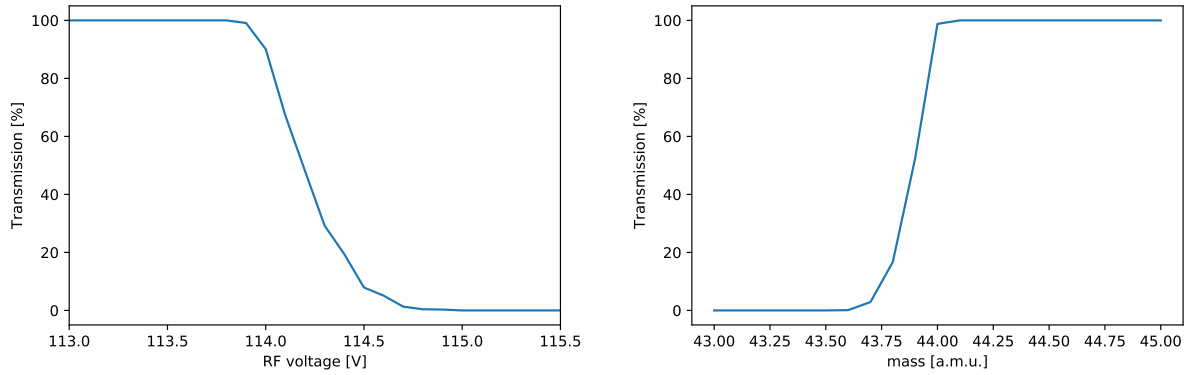

(a) (b)

Figure 4.1: Transmission as a function of (a) the RF voltage applied to the electrodes and (b) the mass of the ions.

The ion guide used at its extreme point in RF-only mode (extreme right of the triangle) acts as a high-pass mass filter that eliminates impurities.
The experiment using the quadrupole aims to perform rovibronic spectroscopy on complexes produced by the valve and with a higher mass-to-charge ratio than 44 amu corresponding to CO_2^+. If one wants to analyse those complexes, the RF voltage can be increased in order to eliminate lighter masses. This is experimentally possible in the limit of the electronics supply: at a certain point, the theoretical RF voltage is too large with respect to the maximal RF voltage that can be provided by the circuit. This limitation will be briefly discussed in the section 5.2.

Despite this high-pass mass filtering capability, an ion guide can act as a focusing element. The ions experience a certain number of RF cycles while travelling through the quadrupole. This number is given by:

$$N_{RF} = \nu_{RF} t_{ion} \tag{4.1}$$

with ν_{RF} the RF frequency in [Hz] and t_{ion} the time of flight of the ion in the quadrupole in [s]. Much like electromagnetic or sound waves, the envelope of the ion bunch oscillates, leading to the presence of bellies and nodes. A precise choice of the operating conditions can lead to a focusing or a defocusing of the bunch at the exit of the quadrupole. This focusing effect is illustrated in Figure 4.2a.

A periodic focusing effect is observed as a function of the q_u value. In the same figure is also represented the evolution of the variance of the beam divergence angle. Both curves are shifted by a half-period. The higher the beam size, the smaller the divergence angle:

this corresponds to a belly of the wave. On the contrary, the smaller the beam size, the higher the divergence angle: this is a node of the wave. Those two extreme conditions are depicted in Figure 4.2b. It turns out that to have a non-divergent beam in output, it is better to maximize the beam spot size at the exit of the quadrupole as to minimise the divergence.

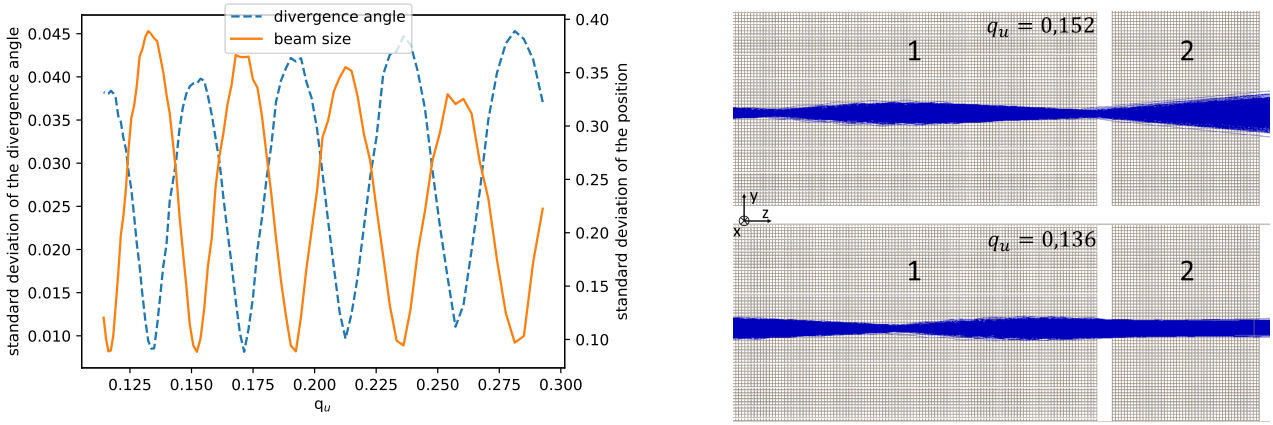

(a) (b)

Figure 4.2: (a) Variance of the ion beam spot size and of the divergence angle as a function of the operating conditions. Only q_u is indicated, $a_u = 0$. (b) Representation of the simulated ion bunch in SIMION for two cases. The legend is 1: the quadrupole and 2: the outer electrode. The operating condition is indicated on the figure.

4.2 The quadrupole as a mass filter

In this work the quadrupole will be used as a mass filter with the aim to observe rovibronic transitions thanks to the excitation of a continuous wave laser source. With a quadrupole mass filter, a mass selection can be performed with slow ions, which is a great advantage if one wants to perform continuous excitation (see section 5.3). By selecting properly the desired mass to analyse, the observed spectral signature will be mass specific and the ion detection will reach high sensitivities.

Also, in fundamental physics, if one wants to observe the amount of a certain product resulting from an ion-molecule reaction, a mass filter is usually installed after the trapping system. This is the case in the following experiments of Gerlich or Asvany for example [26, 27, 34]. A scan on the U/V values (i.e. the mass scan line) provides the mass spectrum of the reaction.

4.2.1 Mass resolution

In order to select a specific mass in the best way, one has to think about the mass resolution of a quadrupolar system. Indeed, the better the resolution, the better the mass selection. The resolution is defined as:

$$R = \frac{m}{\Delta m} \tag{4.2}$$

i.e. the ratio between the peak mass (m) and the full width at half maximum (Δm) of that peak.

It has been already mentioned in sections 2.1.5 and 3.3 that in the stability triangle of a quadrupole, U/V lines are also called mass scan lines: the best mass selection is achieved when the slope of the scan line crosses the apex of the triangle.
It has been shown by Paul *et al.* [1, 80] that the resolution can be written:

$$R = \frac{0.126}{0.16784 - U/V} = \frac{0.126}{(0.16784 - \gamma) + \delta/V} \tag{4.3}$$

This relation is based on the stability diagram of a quadrupole. Indeed, because q_u is inversely proportional to m, one can derive a relation for $q_{apex}/\Delta q_u$ and transpose it to $m/\Delta m$. Here, Δq_u corresponds to the range of q_u values intercepted by the U/V (or $a_u/2q_u$) slope considered. This reasoning process is depicted in Figure 4.3a. The Equation 4.3 is only valid in a range of $\Delta q_u \leq 5\%$ since it is based on a Taylor expansion of the q_u equation near the apex.

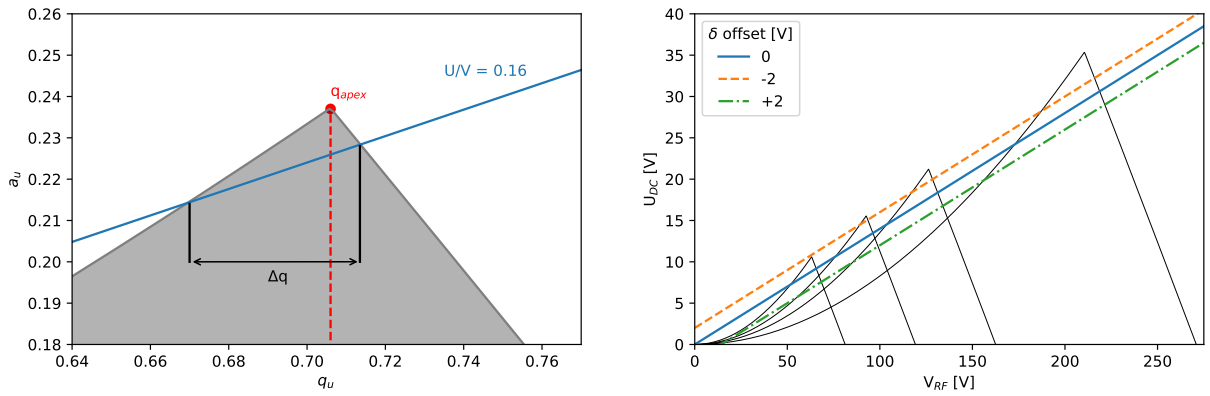

(a) (b)

Figure 4.3: (a) Graphical illustration of the methodology leading to the derivation of Equation 4.3 and (b) graphical illustration of the impact of the application of a dc offset on the resolution.

Equation 4.3 is only valid in the case of an infinitely long quadrupole and considering an ideal behaviour. At the denominator of this expression, the 0.16784 factor corresponds to

the slope passing through the apex of the stability triangle, i.e. the maximal $a_u/2q_u$ ratio providing stable conditions. The second equality is obtained given the following relation between U and V, $U = \gamma V - \delta$, where γ (an adimensional factor) and δ (in [V]) are two parameters that can be modified experimentally. In a laboratory experiment, this is how resolution can be changed: one can vary U proportionally to V or by only adding a small DC offset. The parameter γ corresponds to a change in resolution, because the U/V slope is either increased or lowered. The parameter δ corresponds to the addition of a certain dc offset, implying a change in the origin of the U/V slope. The effect of a change in δ is illustrated in Figure 4.3b. Two cases can be distinguished:

1. If $\delta = 0$, the resolution will stay constant for any mass: this is the constant $m/\Delta m$ mode.

2. If $\delta \neq 0$, the resolution will become proportional to V. This means that R will increase or decrease (depending on the sign of the offset) proportionally to V and so proportionally to m. This is the so-called constant Δm mode.

In a real setup, the resolution is limited by several experimental factors, the most important one being the finite length of the quadrupole. Because of that, some theoretically unstable ions will be transmitted, leading to a decrease in resolution. This effect is mathematically translated by considering the number of RF cycles seen by an ion while travelling into the quadrupole [6]. The higher the number of cycles is, the higher its interaction with the electric field, the more precise is the ion selection and the higher the resolution will be. The number of RF cycles introduced in the Equation 4.1 is developed here as:

$$N = \nu_{RF}\frac{L_{quad}}{v_z} = \nu_{RF}L_{quad}\sqrt{\frac{m}{2E_{kin}}} \tag{4.4}$$

with ν_{RF} the frequency in [Hz], L_{quad} the length of the quadrupole in [m], m the mass in [kg] and E_{kin} the kinetic energy of the ions in [J].
The link between the resolution and the number of RF cycles is given by the following empirical relation [86]:

$$R = \frac{N^n}{h} \tag{4.5}$$

where h is a constant depending on the experimental setup and n is close to 2. This link can be understood as follows: getting back to the solutions of the Mathieu equation (see subsection 2.1.2), it has been shown that the stability depends on the value of a certain parameter β. The latter is directly related to the frequencies making up the trajectories of the ions. This β parameter can be expressed in the same form as Equation 4.3.

Indeed, iso-β lines near the apex can be considered as straight lines as shown in Figure 4.4. By considering the link between a_u, q_u and β (see Equation 2.32), one can derive an equation for β as a function of U/V. Paul *et al.* have shown that depending on the axis, β can be

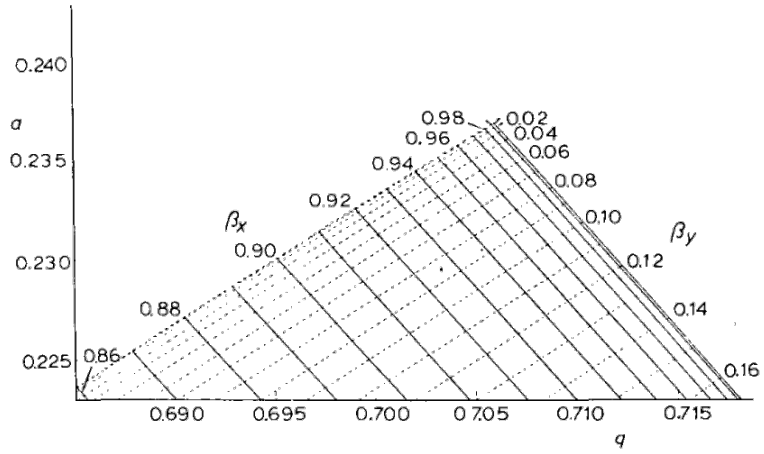

Figure 4.4: Zoom on the higher part of the first region of the stability diagram, where iso-β lines are represented. Taken from [6].

written [80]:

$$\beta_y^2 = \frac{0.16784 - U/V}{0.562} \tag{4.6}$$

$$(1 - \beta_x)^2 = \frac{0.16784 - U/V}{1.372} \tag{4.7}$$

The β factor can also be written in terms of the number of RF cycles experienced by the ion: it is related to the frequency of the secular motion. Considering $N = 1/2\beta_y$ and $N = 1/2(1 - \beta_x)$, it turns out that the theoretical value for the h factor is $h = 2.23$ in the x direction and $h = 5.43$ in the y direction. On the other hand, the h factor has been experimentally measured and some papers have shown that it lies between $h = 12$ and $h = 20$. For example, Austin *et al.* have shown that, for reasonable values of R (typically from 20 to 500), the power law in Equation 4.5 is a square law with h close to 20 [86].

By considering a factor of around 15, the maximal attainable resolution by a quadrupole with hyperbolic electrodes can be written:

$$R \simeq \nu_{RF}^2 L^2 \frac{m}{30 E_{kin}} \tag{4.8}$$

In this experiment, with $\nu_{RF} = 1.19$ MHz and $E_{kin} = 2.082$ eV, the resolution should be close to $R \simeq 413$ in the best case.

A first simulation has been done for a range of masses to observe the mass resolution of each system (quadrupoles A, B and C). The (U,V) combination used for this simulation corresponds to the one of the apex found thanks to the simulations presented in the chapter 3. The result of the first simulation obtained with the quadrupole A as a mass

filter is given in Figure 4.5a. It turns out that the transmission is good for a quite wide range of masses: the resolution is equal to $R = 59$, which is bad compared to the ideal value ($R \simeq 413$).

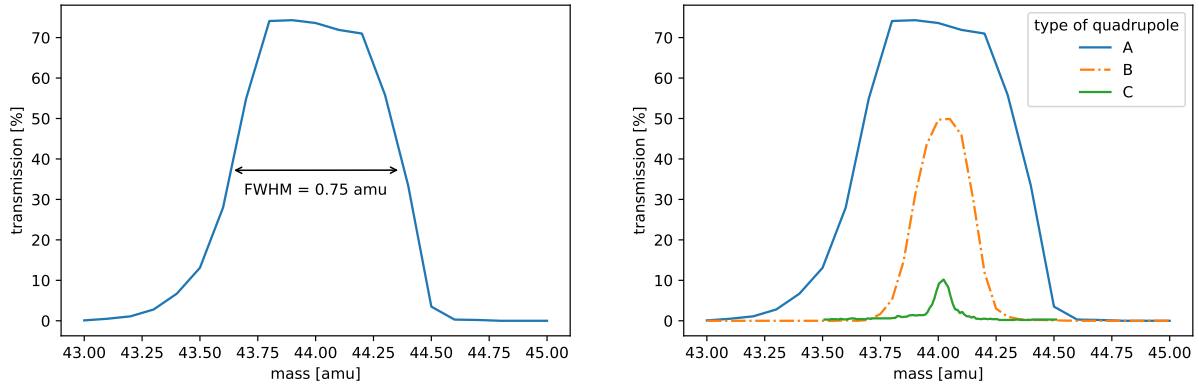

(a) (b)

Figure 4.5: Transmission as a function of the mass of the ion beam passing through the quadrupole (a) for the quadrupole A (b) for the three studied systems.

A comparison has been done with the two other cases in Figure 4.5b. It is clear that the quadrupole A has a worst resolution than both other systems, and the quadrupole C has a really good resolution. Indeed, in that case, $\Delta m = 0.075$ and so $R = 587$. That value is even better than the resolution derived before, considering the number of RF cycles (see Equation 4.8). For that quadrupole, the h factor is smaller because no other effect than the finite length of the quadrupole have been considered. For the quadrupole B, the resolution ($R = 157$) is almost three times higher than the one of the quadrupole A.

One can observe that the transmission in the quadrupole A is large (T $\simeq$ 70 %) compared to the two other studied systems (T $\simeq$ 50 % and T $\simeq$ 10 % for the quadrupoles B and C respectively). To increase the resolution, one could take operating conditions where U/V $>$ 0.1678, theoretically out of the stability diagram. As long as this quadrupole does not exactly obey the Mathieu theory, it could have stable operating conditions at higher values: the stability triangle could be slightly shifted up. This has not been proven before (see Figure 3.6a) but the transmission higher U/V slope could have been investigated. Given that hypothesis, a mass scan has been done with U/V = 0.17. There, transmission is low (a few percents) and represented in Figure 4.6. The resolution is improved from $R = 59$ to $R = 71$. This value is still far from the ideal case.

4.2.2 Effect of several parameters on the resolution

In order to check that the behaviour of the quadrupole is consistent with the theoretical resolution (see Equation 4.8), a few scans have been performed on several determinant

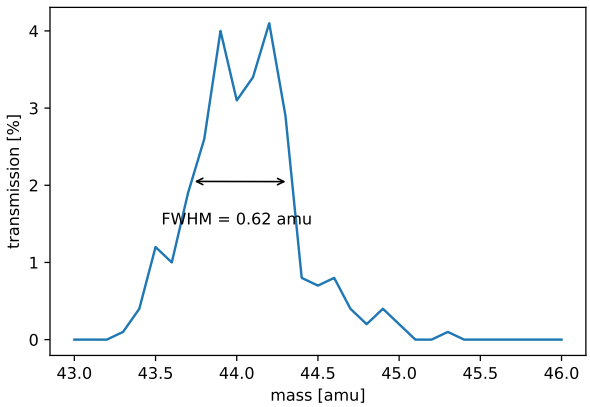

Figure 4.6: Transmission as a function of the mass for a U/V slope of 0.17.

parameters. It has been supposed that any frequency and any voltage can be reached by the electronics but this is of course not the case in the real setup. A discussion about the experimental limitations will be done in the chapter 5.

Input beam parameters

The same mass scan as before has been performed with an increased beam radius. Consequently, some ions are out of the acceptance of the quadrupole: the transmission is lowered for a beam radius up to $r = 4$ mm, as shown in Figure 4.7a. Increasing the radius leads also to a small increase in resolution. Another simulation has been done with the addition of a small divergence angle in the initial distribution and the result of the simulation is shown in Figure 4.7b. Again, for small angles, the transmission is lowered and the resolution slightly increases.

One can conclude from those two simulations that the acceptance impacts significantly the transmission of an ion beam passing through a quadrupole mass filter but not its resolution. The resolution slightly increases with a larger or a more divergent beam, but this leads to an important decrease in the collected signal in output.

Frequency of the oscillating field

According to Equation 4.8, the resolution should evolve with the square of the RF frequency. A scan over the frequencies has been done to analyse this evolution for the quadrupole A. The result of this simulation is shown in Figure 4.8a. One can observe two main elements on that graph. Firstly, the resolution increases as a function of the RF frequency: peaks are thinner when ν increases, especially in the low masses range. This larger reduction in the low mass side has been observed in other studies performing the same kind of simulations [8, 11]. This increase in resolution as a function of the frequency is shown in Figure 4.8b. That value has been computed by considering the FWHM of the peaks in Figure 4.8a and

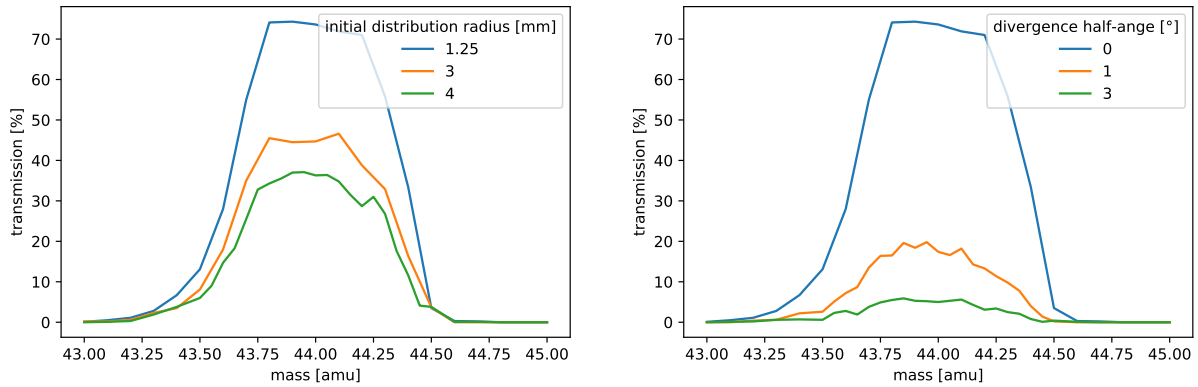

(a) (b)

Figure 4.7: (a) Transmission as a function of the mass for different input beam radii and (b) for different initial divergence angles of the ion beam.

by using Equation 4.2. One immediately notices that the resolution does less than double when tripling the driving frequency.

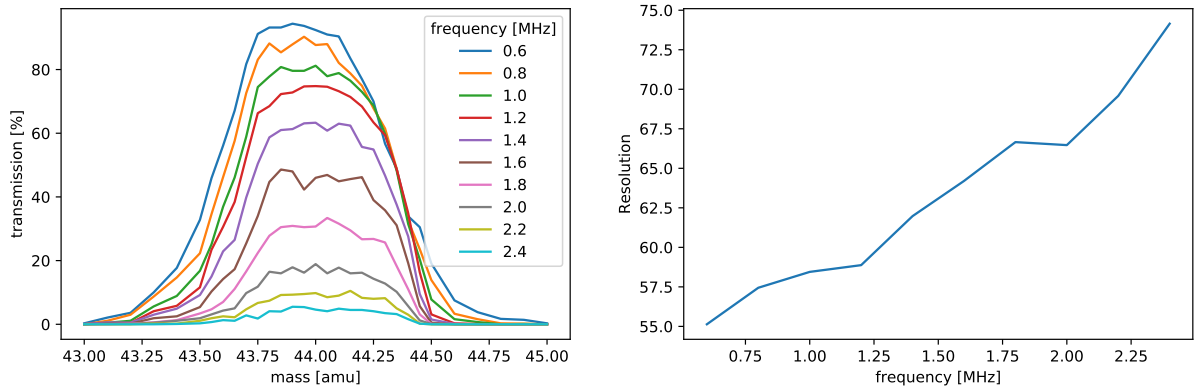

(a) (b)

Figure 4.8: (a) Transmission as a function of the mass for different frequencies. and (b) evolution of the resolution as a function of the frequency.

Secondly, the transmission significantly decreases when the frequency increases. This is (partly) due to the fact that, because of the high frequency, fringing fields are stronger and consequently the output beam is highly divergent. Even without this effect, a small decrease in transmission is normal because of the number of RF cycles seen by the ions is increasing proportionally with the RF frequency.

Is R proportional to m ?

In the theoretical equation for the ideal resolution, R is proportional to the mass of the filtered ion. This has been investigated for typical masses that could be studied in the future: clusters of $[(CO_2)_x\text{-}(H_2O)_n]^+$, having masses of $m = 44x + 18n$. A study of the resolution has been done for $x = 1$ and $n = [0, 4]$. For each mass of interest, the (U, V) combination has been adapted to correspond to the same (a_u, q_u) position in the stability triangle. The result is shown in Figure 4.9a. Each mass peak can be distinguished, even if transmission diminishes drastically when the mass increases. The reason behind this decrease in transmission is again a matter number of RF cycles seen by the ions in the quadrupole and in the fringing fields region, and a matter of extraction voltage. For the masses from 44 to 80, the resolution increases slightly but above that mass, the resolution is too difficult to determine given the low transmission and the shape of the peaks.

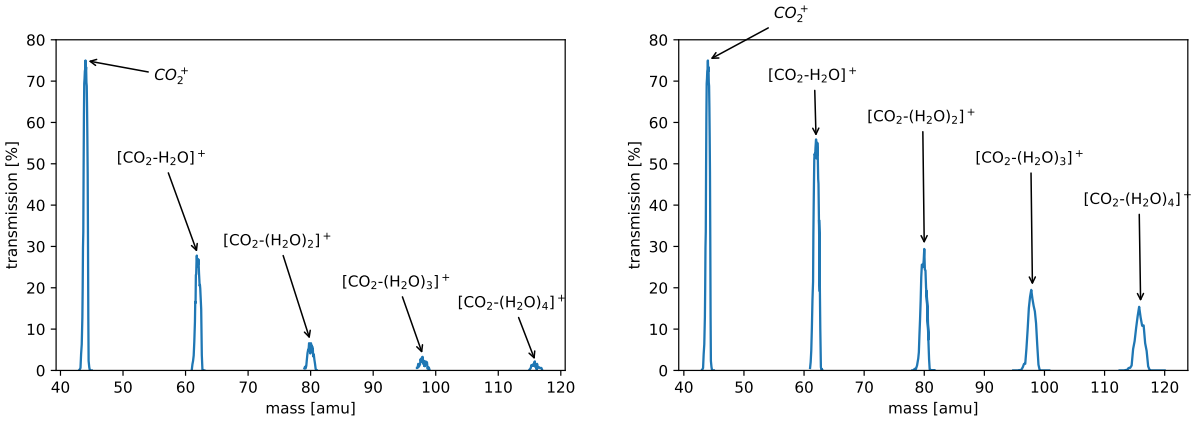

(a) (b)

Figure 4.9: Transmission as a function of several $[(CO_2)_m\text{-}(H_2O)_n]^+$ complexes (a) by changing U and V and (b) by changing the frequency.

A second scan has been done and the result of the simulation is represented in Figure 4.9b. There, to avoid this problem of reduction in transmission, the (U, V) combination has been kept constant but the frequency has been changed to keep the same (a_u, q_u) position in the stability triangle. This is interesting thinking about the definition of the resolution (Equation 4.8): this is the constant R mode. In terms of electronics, this is also an advantage because the RF frequencies that need to be reached for higher masses are much lowered.

From both graphs, it turns out that with the selected operating conditions, R is not proportional to m. In the first case, the extraction voltage should be increased to have a visible peak for masses above 80 amu. This leads however to a decrease in resolution. In the second case, the change in frequency imposes a constant number of RF cycles seen by the ions in the quadrupole, leading to a roughly constant resolution.

Extraction voltage

The extraction voltage is determinant speaking about the kinetic energy of the ions entering into the quadrupole. In Equation 4.8, the resolution is inversely proportional to the kinetic energy of the ions. As before, a scan has been done on several extraction voltages to observe the evolution of the resolution with that parameter. The result is presented in Figure 4.10a. It is clear that the resolution becomes really bad as the extraction voltage increases, as shown in Figure 4.10b. Below 5 V, it has been observed that the change in resolution is limited. The resolution decrease is not exactly fitting with a relation in $1/E_{extr}$ as expected: other factors are influencing its evolution below an extraction voltage of 10 V.

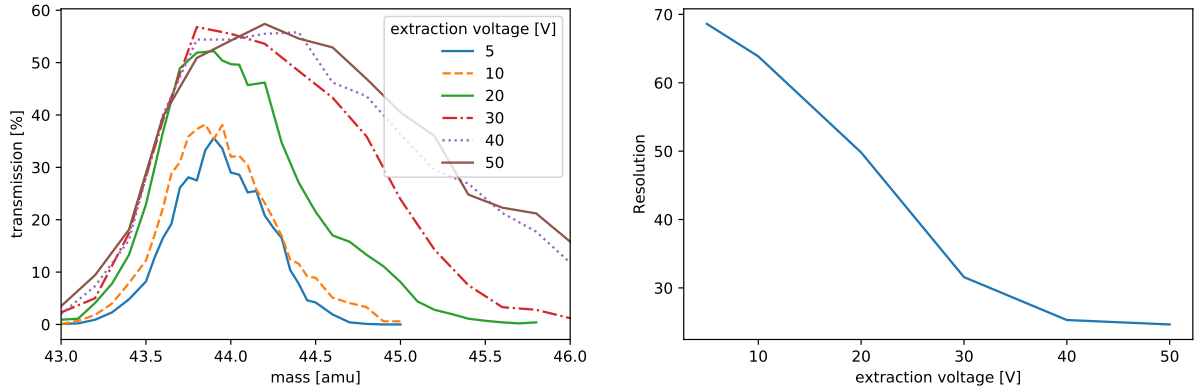

(a) (b)

Figure 4.10: (a) Transmission as a function of the mass for different extraction voltages and (b) the corresponding resolution as a function of the extraction voltage.

Influence of higher harmonics

After a discussion with the electronics workshop and according to the paper after which the electronic circuit feeding the quadrupole is designed on (see section 5.2), it turns out that the RF signal sent to the system might not be purely of frequency ν_{RF}. A second harmonic term can appear. That factor is generally small (close to an attenuation of 60 dB, i.e. 1/1000) but it might influence the performances and the resolution of the quadrupole.

The result of the simulation is represented in Figure 4.11. The peak is exactly the same with or without the contribution of 60 dB: that factor is too small to influence the mass resolution. If one increases the second harmonic contribution, it appears that resolution is surprisingly improved at 50 dB and even better at 40 dB. This effect is probably due to the shape of the potential in this particular quadrupole A. Still, transmission is reduced, such as in the case of a contribution of 30 dB. At 20 dB, i.e. a contribution of 1/10, the transmission is instead equal to zero. One can conclude from this simulation that the second

harmonic can contribute up to 40 dB (i.e. 1/100) to the electric signal without significantly affecting the performances (in terms of transmission and resolution) of the quadrupole mass filter.

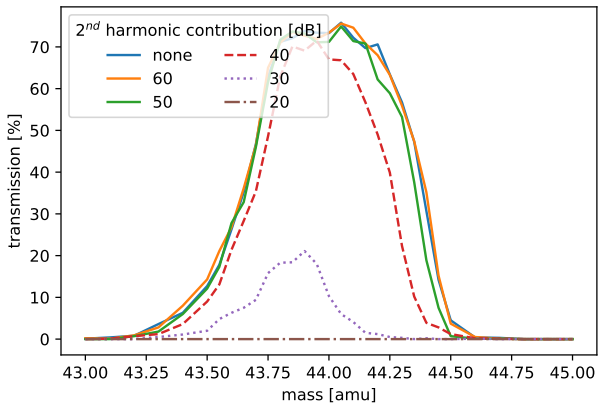

Figure 4.11: Transmission as a function of the mass for different contributions of the second harmonic.

Discussion

As a conclusion, those simulations show that mass filtering with the quadrupole A is experimentally possible. Its resolution is however quite low compared to the quadrupoles B or C but also with other quadrupole mass filters. Indeed, the commercially available quadrupoles commonly used in experiments have a resolution that can easily attain $R = 1000$ depending on the operating conditions [87, 88]. One solution in order to increase the resolution of this quadrupole A is to go higher in the stability diagram, in a theoretically unstable operating condition. This might however reduce the transmission drastically, leading to a too weak signal collection. A good point regarding this quadrupole is that the resolution is not affected by a reasonable range of divergent or larger incoming ion distributions: it is robust in that point of view.

The influence of several parameters has been studied. It turns out that resolution is indeed increased with the RF frequency, but the transmission is significantly reduced due to the presence of fringing fields and the increase in RF cycles experienced in the quadrupole. Speaking about a complete mass scan of $((CO_2)_x\text{-}[H_2O]_n)^+$ complexes, it turns out that the RF frequency has to be changed (and reduced) instead of the (U,V) combination. If the frequency is lowered, the resolution stays roughly constant while if the (U,V) combination is increased, transmission becomes really bad and no clear signal is observed in output of the simulation for high masses. Then, it has been shown that the extraction voltage implies an important decrease in resolution above 10 V. Below that value, its effect is limited. Finally, experimentally speaking, the higher harmonic contribution has to be minimised, at least

under 40 dB (i.e. a factor 1/100).
One can say that given those simulations, an optimum has to be found between those parameters of U, V, ν and E_{kin} in order to maximise the resolution.

One could push the investigation in mass resolution further, by considering for example the space charge effects on the ion beam, an eventual mechanical misalignment of the rods, the addition of an extraction voltage at the end of the quadrupole, etc. Still, this first set of simulation already gives a satisfactory basis speaking about the resolution of the quadrupole A.

4.3 The quadrupole as an ion trap

The working timeline of the ion trap has been described in the subsection 2.1.6. The goal of this section is to simulate a few trapping conditions and to observe which of them are the best ones. The trapping has to last as long as possible, with a high transmission in output and a slightly divergent beam. The motivation behind ion trapping lies in the ability to study ion-ion and ion-molecule reactions. Also, in a further step, an ion trapping system can be coupled with a cold head to cool down the studied ions.

4.3.1 Preliminary studies with Python

The previously presented *Python* script has been extended from a simple resolution of the Mathieu equation to the simulation of a whole trapping system. To do so, a potential has been added in the z direction. That potential has been approximated as independent of x and y. The idea is then to solve the equation of motion not only in x and y as before but also along z in order to experience the trapping potential.

As a first approximation, a harmonic potential has been considered. It is written:

$$V(z) = U_e \left(\frac{z}{z_0}\right)^2 \tag{4.9}$$

with U_e the potential applied to the electrodes in [V] and z_0 the half-length of the quadrupole in [m]. The equation of motion in z is:

$$m\frac{d^2z}{dt^2} = qE_z = -q\frac{\partial V(z)}{\partial z} = -\frac{2qU_e}{z_0^2}z \tag{4.10}$$

In order to have a coherent resolution in x, y and z, the dimensionless parameter of Mathieu ξ has to be introduced in the equation. It turns out that:

$$\frac{d^2z}{d\xi^2} = -a_{trap}\ z \qquad \text{with} \quad a_{trap} = \frac{8qU_e}{m\Omega^2 z_0^2} \tag{4.11}$$

a_{trap} is the analogous coefficient of the a_u Mathieu coefficient but characterising the ion motion along z.

The harmonic potential is represented in Figure 4.12a with the kinetic energy of the ion. The trajectory of the trapped ion is represented in Figure 4.12b. The ion has a kinetic energy of 2.082 eV in $z = 0$, the potential combination of the rods is (U,V) = (0,15), the RF frequency is at 1 MHz and the potential of the electrodes is set to $U_e = 2.5$ V. The ion started in a position $(x, y) = (0.1, 0.1)r_0$ from the axis of the quadrupole and has been trapped for 0.175 ms. That initial condition in depicted in Figure 4.13, with a general scheme of the trapping system.

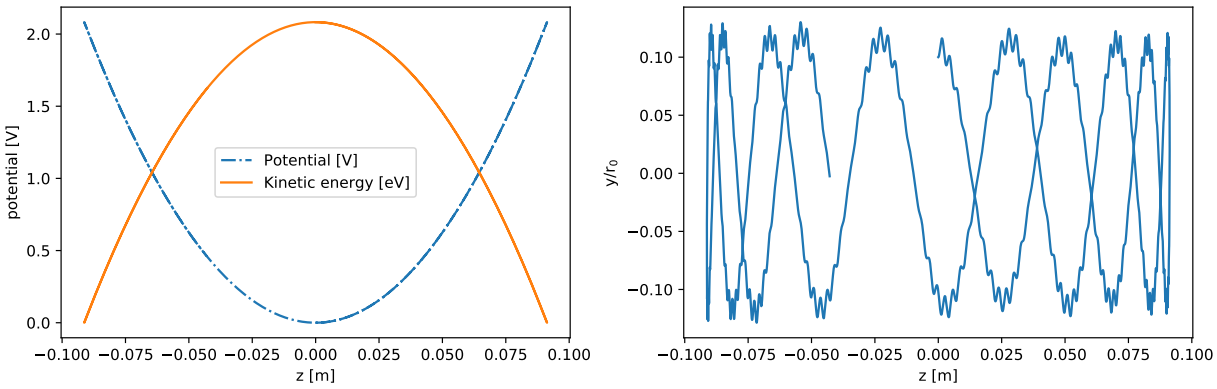

(a) (b)

Figure 4.12: (a) Electric potential and kinetic energy of an ion in a quadrupole trap and (b) its trajectory along y.

As long as no other effect than the potential in z has been considered, the total energy of the ion is a constant of the motion and is equal to its initial kinetic energy.

Thanks to those equations, any ion trajectory can be simulated for a certain trapping time and its stability can be studied. The ion should be stable along the whole stability triangle, but the acceptance of the quadrupole will be smaller and smaller while increasing the trapping time. Therefore, a highly stable operating point in the stability triangle is preferred, especially in its lower part.

In a real setup, the potential is not harmonic but has a bucket-like shape. It is approximated by:

$$V(z) = \left[1 - exp\left(-\left(\frac{z}{z_0}\right)^{2n}\right)\right] U_e \qquad \text{with } n > 2 \tag{4.12}$$

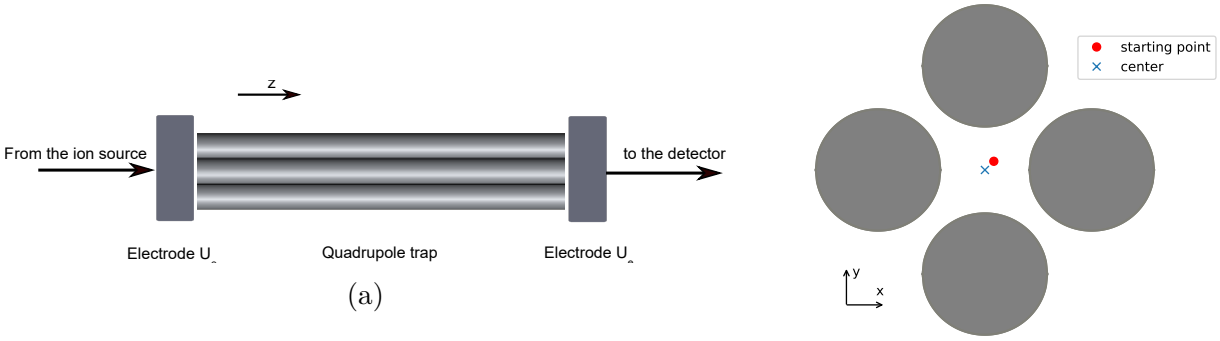

(a)

(b)

Figure 4.13: (a) Schematic view of the trapping section, with the quadrupole and its two surroundings electrodes and (b) cross-sectional view with the starting point for the example in Figure 4.12

Putting this potential in the equation of motion leads to:

$$m\frac{d^2z}{dt^2} = -q\frac{\partial V(z)}{\partial z} = -qU_e\frac{2n}{z_0}\left(\frac{z}{z_0}\right)^{2n-1} exp\left(\left(\frac{z}{z_0}\right)^{2n}\right) \tag{4.13}$$

Again, by analogy with the harmonic potential, one can express this equation as a function of ξ with the a_{trap} coefficient:

$$\frac{d^2z}{d\xi^2} = -a_{trap}n\left(\frac{z}{z_0}\right)^{2n-1} exp\left(\left(\frac{z}{z_0}\right)^{2n}\right) \tag{4.14}$$

This more realistic potential has also been implemented in the *Python* script. The potential is represented in Figure 4.14a for a set of different n exponents. It is clear that the higher the exponent is, the larger the potential-free region and the steeper the potential wall at the end of the quadrupole will be. Consequently, the ion will be reflected further as n increases. This large field-free region is interesting because it limits the perturbation of the ion trajectory. For the same n exponent, the voltage of the electrodes plays a role in the stiffness of the potential walls: the greater U_e, the steeper the potential wall. That U_e effect is represented in Figure 4.14b.

The trajectory of an ion with the same parameters than the one represented in Figure 4.13 has been computed with a bucket-like potential. The voltage of the electrodes has been set to $U_e = 5V$ for a bucket exponent of $n = 10$. With that U_e and n combination, the reflection of the ion happens precisely at the end of the quadrupole. The ion has been trapped during 1 ms and its trajectory along the y direction is represented in Figure 4.15a.

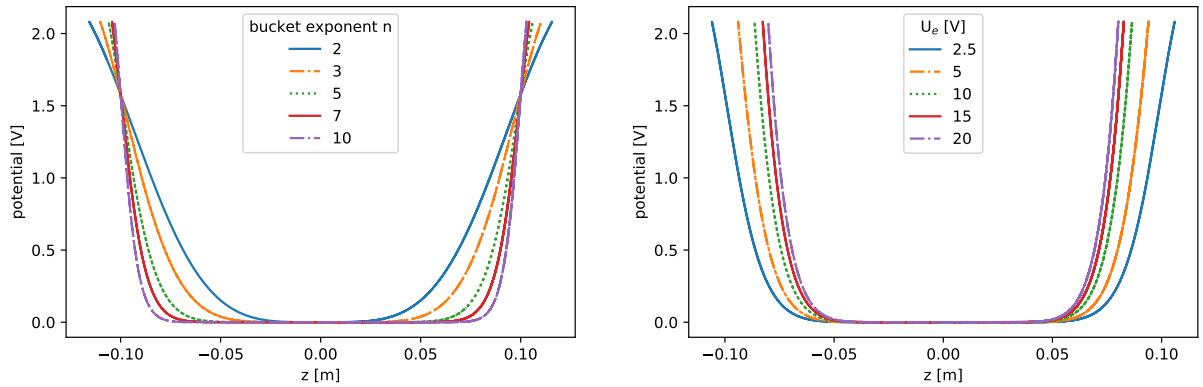

(a) (b)

Figure 4.14: Bucket-like potential as a function of the position in the trap, represented for (a) different n exponents ($U_e = 2.5$ V) and (b) for different U_e voltages ($n = 5$).

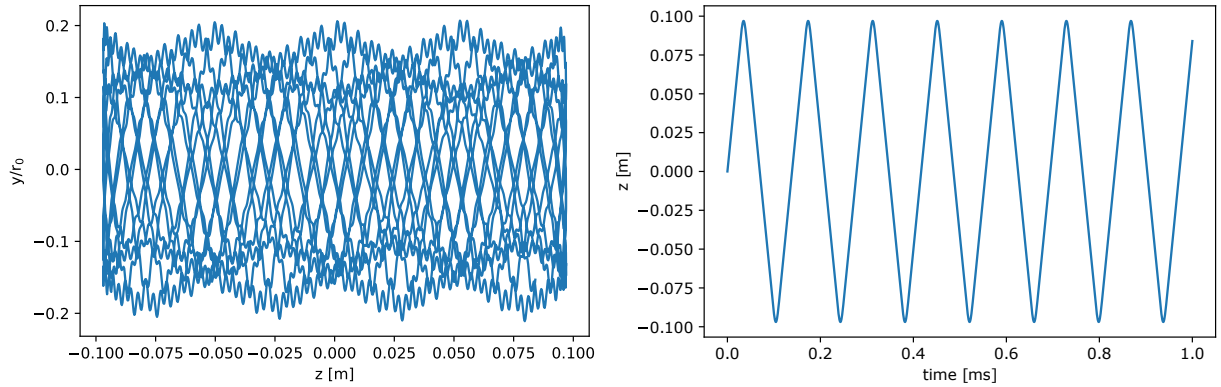

(a) (b)

Figure 4.15: (a) Trajectory of an ion along the y direction, in a bucket-like potential and trapped during 1 ms and (b) its z trajectory as a function of time.

Another point can be analysed in this trajectory: the number of round trips experienced by the ion. This is represented in Figure 4.15b. This is directly related to the velocity of the ion and the distance that it can travel into the trap. For a bucket potential such that the ion is reflected at the extremity of the quadrupole, for a trapping time of 1 ms and a kinetic energy of 2.082 eV, the number of round trips is given by:

$$N_{RT} = \frac{t_{trap}}{t_{RT}} = \frac{t_{trap} v_z}{2L} = \frac{t_{trap}}{2L}\sqrt{\frac{2E_{kin}}{m}} = 7.56 \tag{4.15}$$

with the RT index standing for "round-trip". The obtained number matches with the

number of round trips represented in Figure 4.15b ($N_{RT} \simeq 7.2$), but is slightly reduced because the mean kinetic energy of the ion stands a little bit below 2.082 eV.

At this stage, the developed simulation is a first good approximation of the effect of the trapping voltage but it presents two main limitations. Firstly, it supposes a perfect energy transfer between the electric potential and the kinetic energy. Secondly, it makes the hypothesis that the quadrupole field is present all along the trajectory. This is not necessarily the case in a real setup: the electrodes are placed out of the quadrupole field. If the voltage U_e is too low, the ion will travel beyond the quadrupole and will be reflected between the quadrupole and the electrode. In a mathematical point of view, it means that the z_0 value in Equation 4.12 has to be increased, leading to potential walls positions above $L/2$ (L being the length of the quadrupole). Above $L/2$, the Mathieu equation should not be solved anymore, only fringing fields have to be considered.

A set of simulations have been performed with the described formalism, in order to check that transmission remains reasonable for different operating conditions and trapping times. It would have been time consuming and not necessarily interesting to reproduce a scan on the whole stability triangle. Therefore, the trapping has been considered for a set of operating conditions only: the apex, (U,V) = (8,80), the largest q_u value in RF-only mode and some points in the adiabatic region (i.e. for $q_u < 0.3$). Those operating conditions are represented in a stability triangle in Figure 4.16.

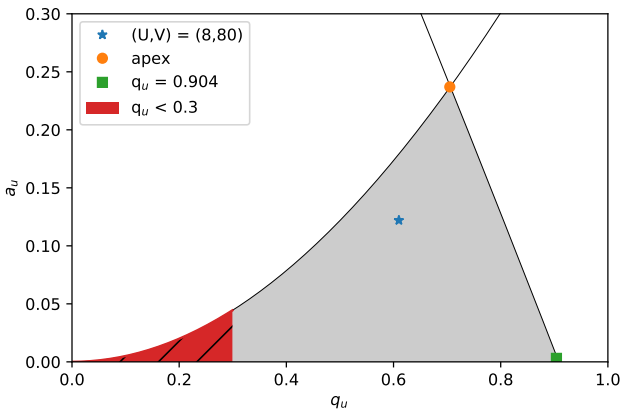

Figure 4.16: Stability triangle with a few operating conditions highlighted. Those conditions have been simulated to observe the trapping abilities of the quadrupole.

The trapping time was set to 1 ms, the electrodes at a voltage $U_e = 5$ V and the bucket exponent to $n = 10$. For the given input distribution (Gaussian in velocity and circular uniform in space), transmission was perfect in the adiabatic case. It was instead equal to zero at the apex: the trapping time is too high and the amplitude of the trajectories are

too large. For the two last cases (the extreme q_u value and (U,V) = (8,80)), transmission is lowered but remains non-zero.

After this first approach, it seems that trapping is indeed possible with a linear quadrupole for a reasonable amount of time of typically 1 ms. The operating conditions have to be carefully chosen because transmission might be lowered or even become equal to zero near the stability limits.

4.3.2 Trapping with SIMION

The more theoretical considerations made with *Python* give a first approach of the trapping conditions. This has been transposed to the setup in SIMION, with the real geometric parameters and with the accurate potential shape in the z direction (automatically evaluated by SIMION itself). The objective of this subsection is to observe the main differences and the non-ideal phenomena that could appear with SIMION with respect to the *Python* code.

Bucket potential fit

As it has been shown in the previous subsection, the voltage applied to the endcap electrodes influences the position of the reflection of the ions. In order to have a better idea of the shape of the potential induced by the electrodes, a trajectory has been recorded and the energy of an ion has been fitted with the form of the bucket potential given in the Equation 4.12. Again, it has been considered that the system is conservative.

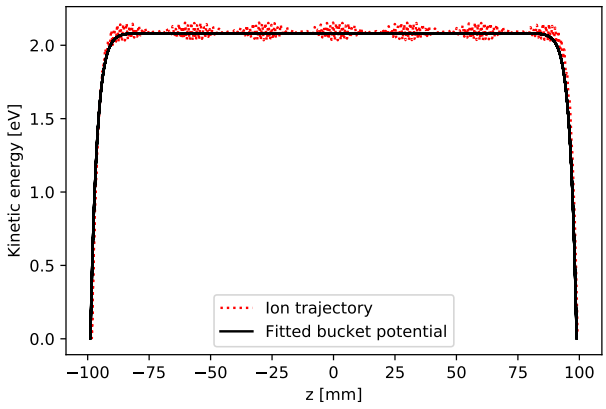

Figure 4.17: Energy of the ion as a function of its position along the quadrupole.

The fit is represented in Figure 4.17. The voltage of the electrodes was set at $U_e = 30V$. The micromotion of the ion is clearly visible around its main kinetic energy of 2.082 eV. The fit is really good and corresponds to the following parameters: $z_0 = 106$ mm (the quadrupole is 200 mm long) and $n = 19$. Two other fits have been done for different U_e

voltages but with the same z_0 and n parameters and it gave corresponding results.

Given those parameters, the SIMION and *Python* results can be compared. A similar trend to the one observed with the *Python* code is observed with SIMION: transmission is generally reduced, especially at positions close to the limits of the stability triangle. Still, two other effects deserve to be analysed in SIMION.

Electrodes voltage

One important effect that is observed in SIMION but not in *Python* is the effect of the electrodes voltage U_e. This is due to the fact that in *Python*, no distinction is made whether the ion is into the quadrupole or between the quadrupole and the electrode. In SIMION, the effect of the quadrupole is limited to its length and attenuated out of it (due to fringing fields). Also, in *Python*, the geometry of the electrode is not taken into account: the potential felt by the ion is also x and y dependent.

The idea here is to analyse what will be the transmission out of the quadrupole, after a trapping time of 1 ms, for different U_e trapping voltages. The applied time sequence is considered to be as given in Figure 2.9, but repeated for different U_e voltages. Transmission is higher when the applied U_e voltage is such that the ion is reflected when it is strictly confined into the quadrupole. A scan has been performed on a set of U_e values for the typical condition (U,V) = (8,80). The transmission is shown in Figure 4.18a.

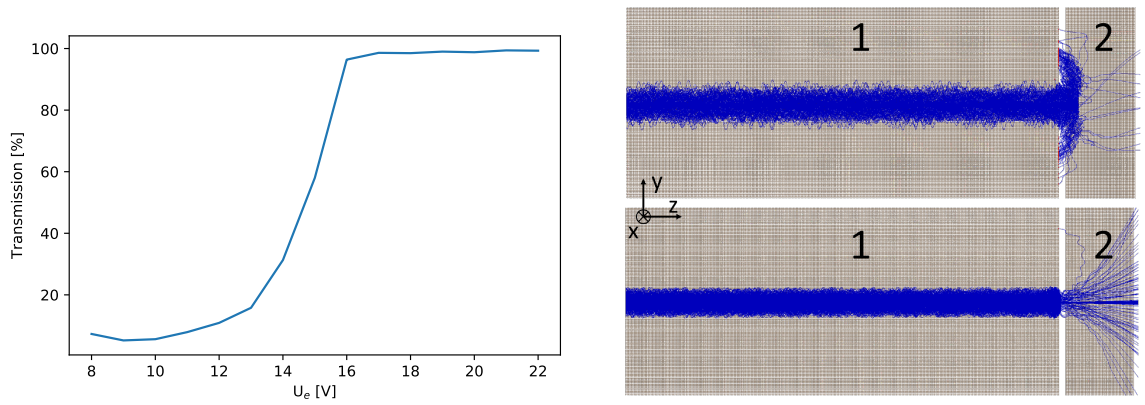

(a) (b)

Figure 4.18: (a) Transmission as a function of the voltage applied on the outer electrodes (U_e) and (b) Two examples of results obtained with SIMION. The upper panel corresponds to $U_e = 10$ V and the lower panel corresponds to $U_e = 20$ V. The legend is 1: the quadrupole and 2: the exit electrode.

Below $U_e = 16$ V, the transmission is not good because the ions are reflected after

the limit of the quadrupole. This is illustrated in the upper panel of the Figure 4.18b. The potential walls are not steep enough, leading to a slow reflection process and a long reflection time. The ions spend more time in the fringing fields region and are clearly reflected after the end of the quadrupole. Depending on their position and velocity, their trajectory might be strongly modified: ions crash onto the rods. After their trapping time of 1 ms, the transmitted ions are forming a highly divergent beam as it can be seen after the electrode (2) in the figure.

Instead, above $U_e = 16$ V, ions are reflected near the limits of the quadrupole. The reflection is faster and happens under a strong hyperbolic field confining the ions between the rods. This is illustrated on the lower panel of the Figure 4.18b: the reflection clearly happens at the limit of the quadrupole. One can see that some ions are divergent but a high majority of them are concentrated in a small bunch close to the center axis of propagation. To improve the focus of the outgoing ion beam, one could take advantage of the focusing properties of an electrostatic lens and optimise the voltage of the lens (2) at the end of the trapping time.

Stationary trapping

Another property of the quadrupole could be used in order to increase the transmission: the focusing effect. This has been introduced in section 4.1. A scan has been done on the frequency for the (U, V) combination considered before, i.e. $(8, 80)$ and for an electrode voltage of $U_e = 14$ V. The result of the simulation is shown in Figure 4.19.

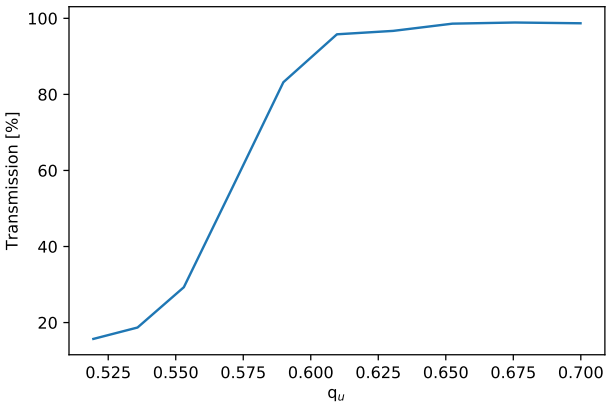

Figure 4.19: Transmission as a function of the q_u value, along the slope U/V = 1/10.

One could expect to observe small oscillations in transmission such as for the ion guide but the obtained result is quite different: there is a transition between low and high transmission values. Two hypotheses are suggested to explain this behaviour:

1. The operating conditions are getting closer to the limit of the stability triangle while

increasing the frequency (i.e. decreasing q_u), leading to an increase of the amplitude of the trajectory and therefore a decrease in transmission.

2. An increase in frequency induces an increase in the number of RF cycles felt by the ion in the fringing field region. The ion is more and more deflected at each reflection and crashes onto the rods.

This is probably a combination of both processes that induces this decrease in transmission for high frequency values. Some small oscillations might be overlapped to this curve but the scanning steps were not thin enough to provide such a result. Those steps could be increased but this would lead to a time consuming simulation.

Discussion

As a conclusion, it has been shown that ion trapping is possible with the quadrupole A for at least one millisecond for several operating conditions. This has been shown in both *Python* for the quadrupole C and transposed in SIMION for the quadrupole A. One has however to be careful with the chosen operating conditions in the stability diagram for two reasons. Firstly, near the stability limits, transmission is reduced. Secondly, the electrodes voltage U_e plays an essential role. If the latter is too low, ions are reflected too far from the end of the quadrupole and are consequently deflected toward the rods leading to a decrease in transmission.

4.4 Trapping and guiding with higher order multipoles

As a final application of the use of electric field to manipulate ions, the *Python* code has been extended in order to simulate the behaviour of ions in multipolar devices. It is able to handle any multipolar order. Again, the code is based on the numerical resolution of the equation of motion, given in eqs. (2.41) and (2.42). This extension can be combined with trapping in order to simulate trajectories of ions in a multipolar trap.

4.4.1 First simulations

As explained in the section 2.2, the two main studied and used multipolar traps in the experiments involving ions are the octupole and the 22-pole traps. Their contour plots are represented in Figure 4.20. The main advantage of such multipolar devices is the large field free region between the rods, much larger than the one of a quadrupole device. Thanks to that, the ions are not feeling any perturbation during most of the trapping or guiding time. This is a great advantage if one wants to study collisional processes or if one wants to cool down the ions to a cryogenic temperature.

As a first result, it is interesting to observe a simple trajectory in both cases. It has been mentioned in section 2.2 that no stability diagram exists for multipole orders higher

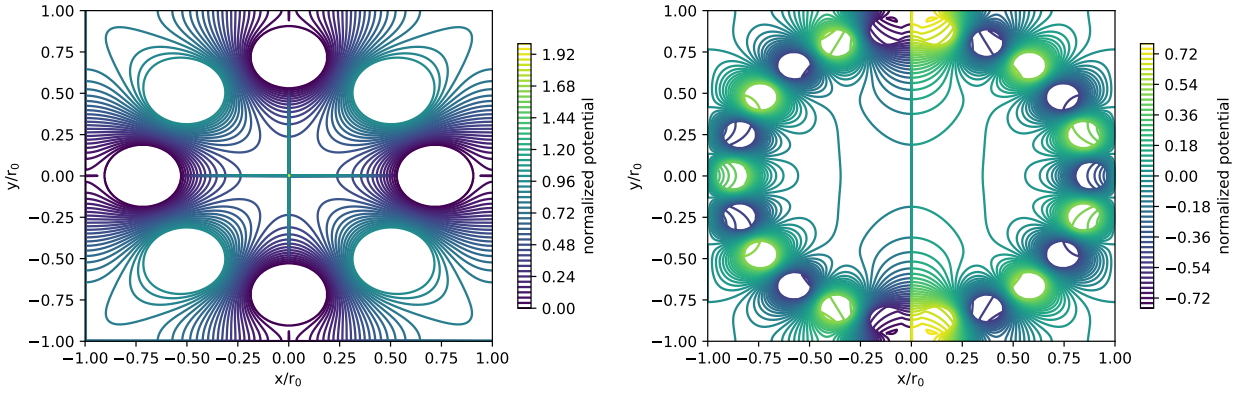

(a) (b)

Figure 4.20: Contour plots of the potential in a (a) octopole and in a (b) 22-pole. 50 equipotential lines are drawn

than the quadrupole. However, a stable trajectory is ensured if the adiabatic parameter η is smaller than 0.3, i.e. if the adiabatic approximation is valid. For operating conditions such that $\eta > 0.3$, the stability depends also on the initial position and velocity of the incoming ions.

For this first simulation, the (U,V) combination is equal to $(0, 15)$, the frequency set to $\nu = 1$ MHz and the ion started in a position $(x, y, z) = (0.001, 0.1, 0)r_0$ and a velocity $(v_x, v_y, v_z) = (0.1, 0.1, 3022)$ m/s. The trajectories are represented in Figure 4.21, for a guiding time of 65 μs in the octupole and 130 μs in the 22-pole.

As it can be seen in Figure 4.21, the oscillation shape is much more "triangular" that the one of a quadrupole device. Also, the amplitude of the trajectory is much higher than in the case of a quadrupole. Both effects are due to the large field free region: the ion travels in straight line until it encounters a high field value close to the electrodes.

Finally, beyond the computation of a simple trajectory, the *Python* code can be used in order to see the trapping of an ion in those traps. The methodology is the same that the one derived in section 4.3 but extended to higher orders.

4.4.2 Conclusion and further improvements of the Python script

The extension of the homemade *Python* script to multipolar elements combined with the ion trapping ability closes the actual developed package. It allows one to have a first theoretical idea of the stability of an ion entering into a multipolar element. Also, thanks to another script, one can generate any distribution in space and velocity of the coming ion beam, extending the abilities of this code to transmission studies depending on the

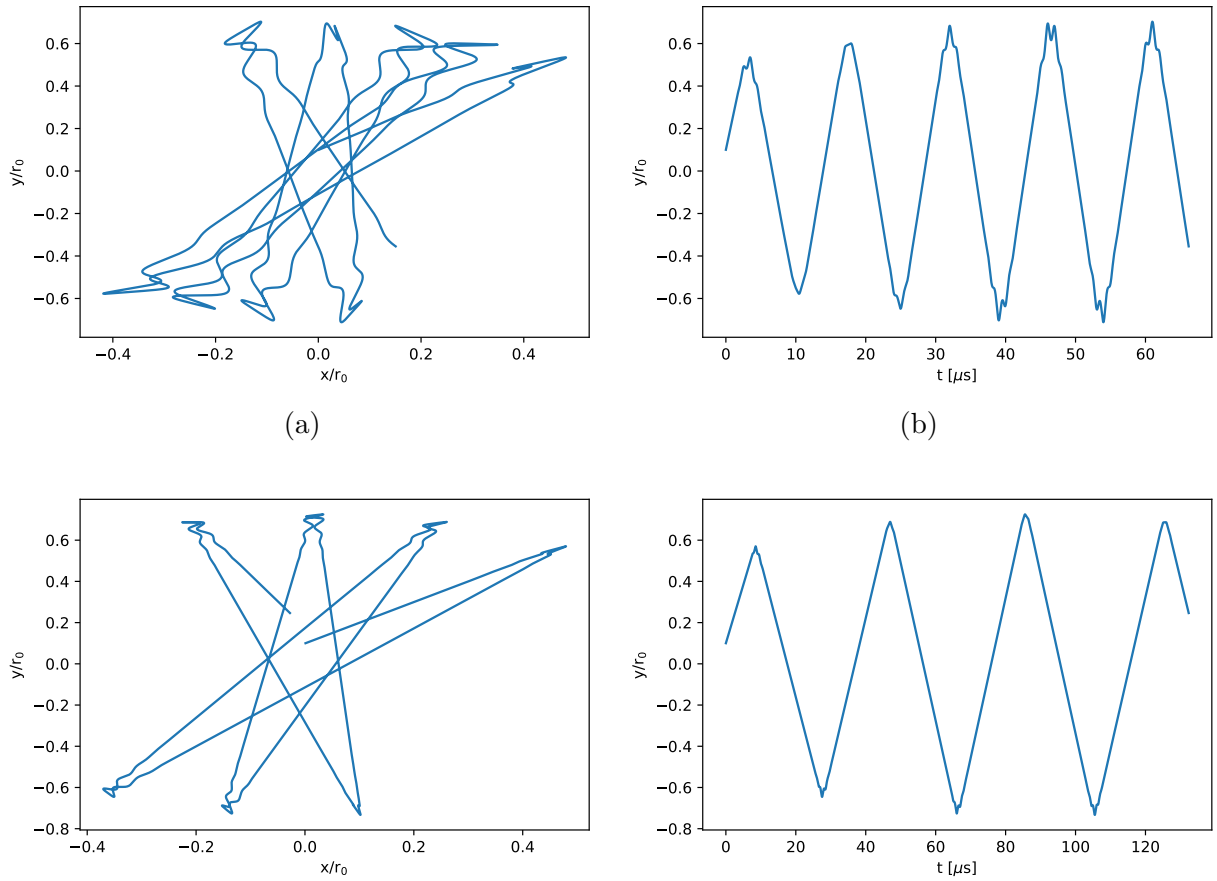

(a) (b)

(c) (d)

Figure 4.21: Trajectories of the ion in (a) and (b) for an octupole guide and in (c) and (d) for a 22-pole guide. In both cases, the left panel is in the xy plane and the right panel corresponds to the yz plane.

operating conditions given as an input. Those studies can be done in all three operating modes: ion guiding, filtering or trapping. For the trapping part, the code is versatile in the sense that the exponent of the bucket potential can be specified in the input. The code in its present level of development can be found in Appendix D.

Further extensions of this code could be the ability to simulate collisions between trapped ions and eventually a buffer gas, as developed by Roland Wester [66] or Oskar Asvany and Stephan Schlemmer [67]. This could be a great advantage to study the buffer gas cooling operation when mounting the trap on a cold head. In terms of potential considerations, the x and y dependence of the bucket potential should be implemented. Also, the finite length of the multipole should be taken into account, with the addition of fringing fields after it.

Chapter 5

Experimental setup

The purpose of this chapter is to give a general description of how the quadrupole could be tested. It is based on an actual setup developed by A. Roucou and R. Bejjani. Some details are also given regarding the homemade electronics of the quadrupole, built by M. Daman and the electronics workshop. The ability of doing a continuous excitation in output of the quadrupole is then discussed, before concluding with a presentation of a smaller quadrupole device allowing one to select or trap much higher masses.

5.1 General overview

The current experiment aims to analyse some rovibronic N_2O^+ spectra thanks to a photodissociation (PD) spectroscopy process. This kind of spectroscopy consists in the analysis of photo-fragments generated by a laser, here a pulsed dye laser (DCM) pumped with a Nd:YAG one. When pumped with a frequency-doubled Nd:YAG laser (emitting at 532 nm), the DCM emits in a range of wavelength between $\lambda = 614$ nm and 654 nm. Then, passing through a non-linear BBO crystal, it is frequency doubled to finally emit in the UV-A range. By scanning the wavelength of the laser, absorption occurs leading to the dissociation of the molecule. The fragments (NO^+) are collected and counted as a function of the wavelength to measure a spectrum.

The experimental setup is presented in Figure 5.1. Its description is based on the paper of R. Bejjani, A. Roucou *et al.* which will be soon submitted. The ions are produced thanks to a pulsed supersonic free jet expansion plasma source (1) and fly through the skimmer (2) to select the non-collisional part of the jet (3). There, acceleration, gating, bunching and re-referencing are made with that single unit to improve the resolving power of the spectrometer and to define a starting time for the time-of-flight (ToF). A first mass selection is made before the interaction with the laser, thanks to a pulsed deflector (5). After the interaction region (7) between the pulsed dye laser (10) and the ion beam, the photo-fragments are mass selected with a 90° deflector (8), before reaching the multi-channel plate (MCP) detector (9). The signal is, as said before, recorded for different wavelengths

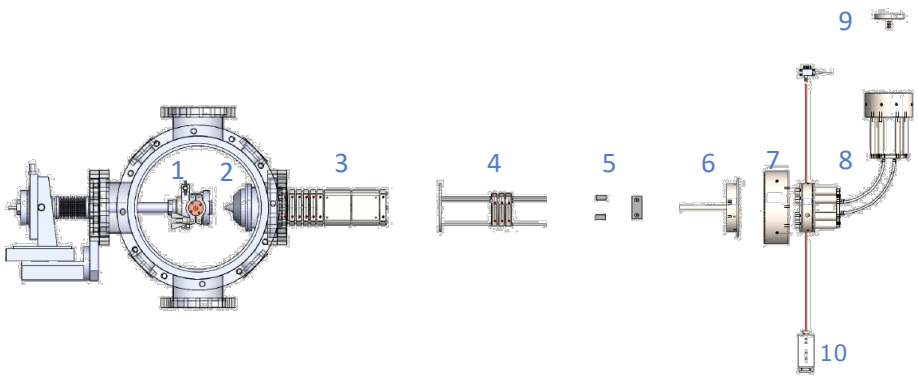

Figure 5.1: Overview of the actual experiment. The legend is 1: the valve. 2: the skimmer. 3: the gating-bunching unit. 4: the electrostatic lens. 5: the pulsed deflector. 6: the differential pumping tube. 7: the interaction region between the ion beam and the laser. 8: the 90° deflector. 9: the MCP detector and 10: the pulsed dye laser. This scheme is directly taken from the paper of R. Bejjani, A. Roucou *et al.* that will be soon submitted.

of the laser, the latter being scanned thanks to a LABVIEW interface.

Two more remarks deserve to be made on that setup. Firstly, the interest in the supersonic expansion lies in the temperature of the generated ions: they are rotationally cold. Therefore, the signal-to-noise ratio is improved and fewer transitions are observed: the spectral analysis is simplified.

Secondly, the skimmer (2) and the differential pumping tube (6) are installed to ensure an efficient differential pumping and therefore a high vacuum at the detector. This is required in order to avoid recombination of the photo-fragments before reaching the MCP. Three different turbomolecular pumps are installed, giving a pressure of around 10^{-7} mbar at the MCP.

The future setup will be based on the current one but adapted for infrared photodissociation spectroscopy of large clusters. At first glance, the same design of gas injection valve, acceleration, gating, bunching and re-referencing unit will be used, but the quadrupole will be added just after the skimmer to operate as a mass filter or as an ion guiding system. A second quadrupole could be installed just before the laser, in order to trap the ions before the interaction. That second quadrupole could also be installed after the laser, in order to perform a mass selection of the photo-fragments. This will be discussed in the section 5.4.

The laser will be a continuous Distributed Feedback Laser (DFB), which is a type of diode laser. Instead of emitting in the UV like the DCM dye laser, it emits in the near-IR, around $\nu = 6550$ cm^{-1}, i.e. $\lambda = 1.53$ μm. The addition of an optical cavity, in order to

reach a higher intracavity power and to perform continuous excitation, will be discussed in the section 5.3.

In the actual experiment, the pulsed valve operates at a repetition rate of 30 Hz providing pulses of temporal length of $t_{pulse} = 50\ \mu s$. The goal of the new experiment including the quadrupole is to improve this repetition rate to more than 1 kHz if possible: a higher repetition rate is an advantage in order to perform continuous excitation. It increases the averaging time by a factor of 33 and consequently, the signal-to-noise ratio will be significantly improved: the Gaussian noise, scaling in $\sqrt{N}$, will be reduced by a factor of $\sqrt{1000}/\sqrt{30} = 5.77$. However, by increasing the repetition rate, the amount of gas injected in the experimental setup increases and this has to be handled with a newly designed vacuum setup. A first discussion about the future vacuum installation is done in Appendix A.

5.2 The quadrupole: mechanics and electronics

A general description of the quadrupole has been already given in section 3.1. Its main physical dimensions were given in Table 3.1. After a brief mechanical description, this section focuses more on how its electrical feeding is achieved.

The quadrupole is made up of four rectified stainless steel rods and surrounded by a metallic outer cap, the latter being grounded. This is done in order to prevent any perturbation coming from an outer element to reach the rods. Two insulating parts hold the four rods together with the outer cap. The insulating material is presumed to be either a piece of Teflon or PEEK: those materials are typically used for this purpose. The whole structure seems to be maintained together thanks to pressure screws.

In terms of electronics, the circuit is based on the setup developed by Robbins *et al.* [89] and has been reproduced by the electronics workshop. The main principle to generate the RF signal is to use a driven harmonic resonant circuit. Its schematic block representation is given in Figure 5.2. One can distinguish the following elements: a sine wave generator, a power amplifier and a transformer. Consequently, the signal is firstly generated, then amplified and finally transferred to the quadrupole thanks to a transformer. The second inductance of that transformer is part of an LC resonant circuit providing the output signal.

The air-gap capacitance in the LC circuit can be tuned thanks to a small step-motor in order to scan a range of frequencies. Indeed, the resonant frequency of a LC circuit is given by:

$$f = \frac{1}{2\pi\sqrt{LC}} \tag{5.1}$$

with L and C the total inductance and the total capacitance of the resonant circuit. The ability to change the capacitance is then a great advantage. Still, one has to note that

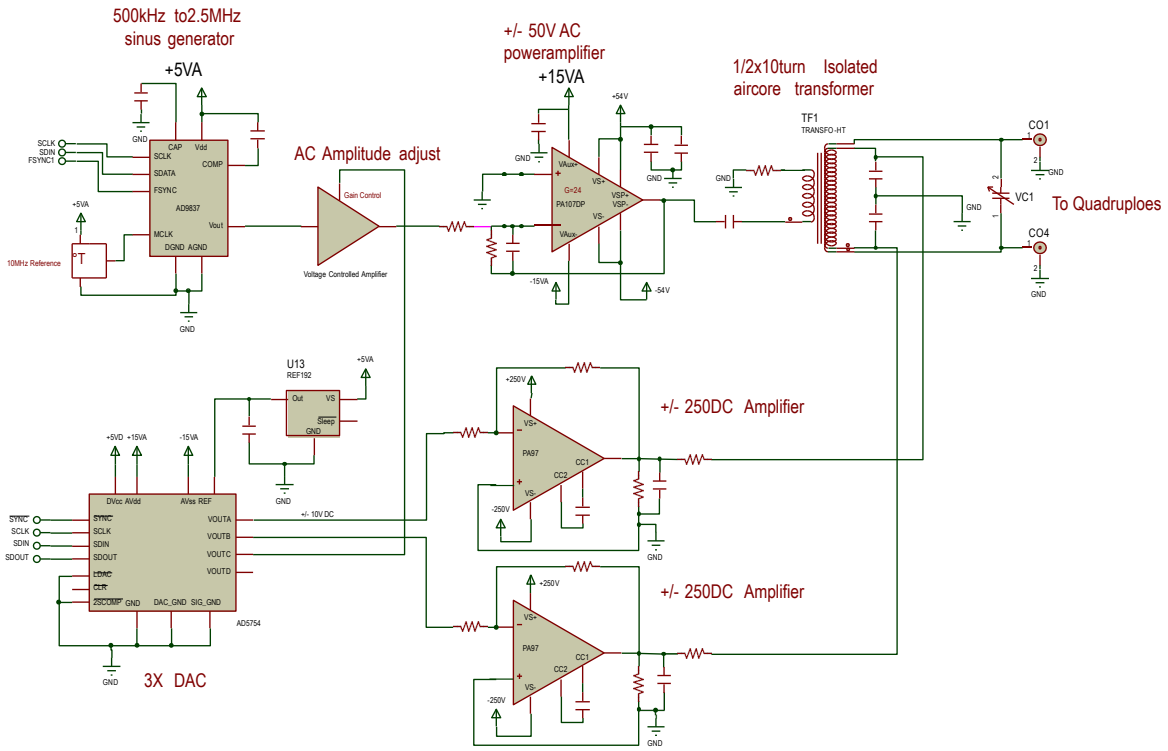

Figure 5.2: Schematic view of the electronic setup feeding the quadrupole. The main elements are denoted, from left to right : the sinus generator, the amplifier and the transformer.

the above capacitance is the total capacitance of the circuit. The rods of the quadrupole, the wires between the generator and the quadrupole, etc. have their own non-negligible capacitance. In order to have a great impact on the frequency, one has to minimise the previously cited values by placing the circuit as close as possible to the rods. The measure of the capacitance of the rods of the quadrupole has been done and it is equal to $C_{rods} = 34$ pF.

Three pictures of the final circuit are shown in Figure 5.3. Some previously mentionned elements can be recognised easily, for example (3) the transformer and (4) the air-gap tunable capacitor. The other elements are mentioned on the caption of the figure. The sine wave generator is too small to be identified directly on the circuit. As it can be seen in Figure 5.3b, the air-gap capacitor can be tuned in the range of $C_{var} = 20$ pF to 150 pF. The inductance of the transformer is an air-core inductance, ensuring a good coupling without the need of a high inductance value. Both components could be changed in a future improvement of the circuit, in order to reach higher frequencies for example. One can finally note that all this circuit is mounted on a metallic box, the latter being grounded. Indeed, as long as high frequencies and amplitudes are generated, it emits a large electric field that could perturb any surrounding element. To avoid any perturbation, that metallic box has been installed.

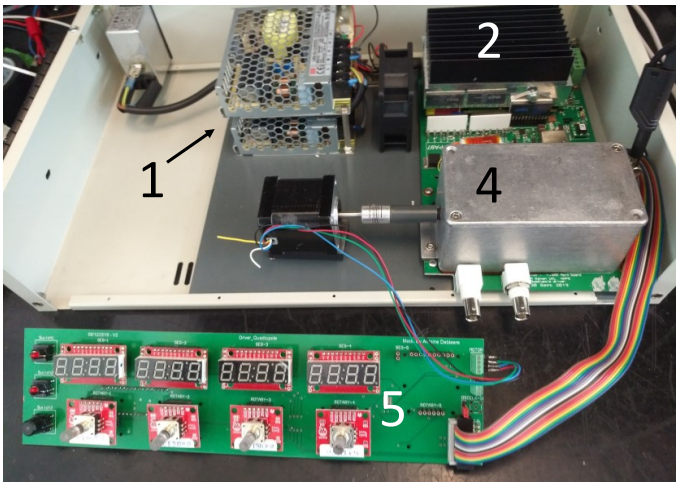

(a)

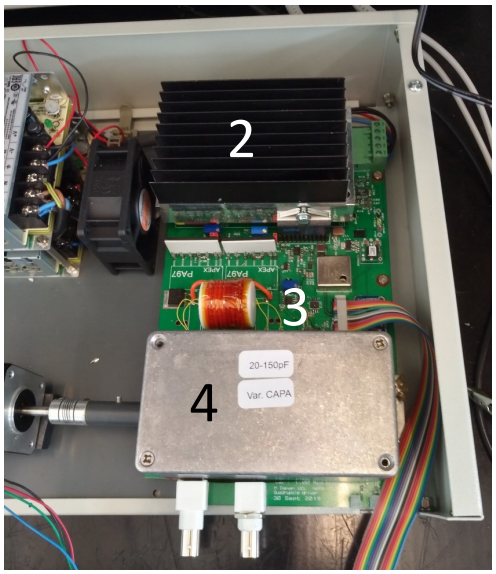

(b)

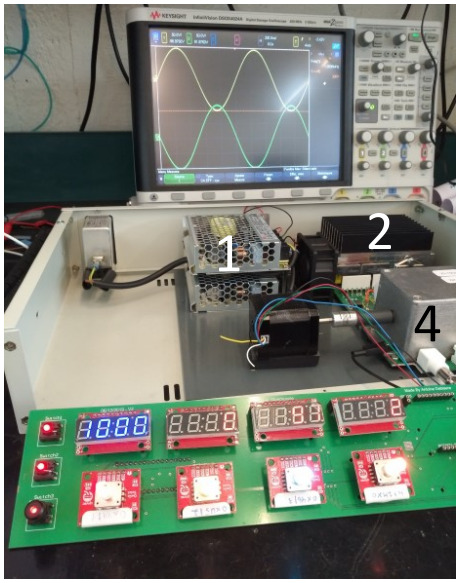

(c)

Figure 5.3: (a) General overview of the electronic circuit in its box. (b) Zoom on the right components. (c) View of the control panel and of the signal sent to the quadrupole (on the oscilloscope at the back). The legend is 1: the alimentation block. 2: the DC converters. 3: the transformer. 4: the tunable capacitance and 5: the control panel.

In terms of performances, the maximal RF and DC voltages that can be attained are 600 Vpp (peak-to-peak) and ± 280 V, respectively. The frequency can be varied between 750 kHz and 1.5 MHz without considering the wires between the circuit and the quadrupole. One could expect a small shift in frequency because of the additional capacitance induced by those elements: this is why a frequency around 1.2 MHz has been chosen for the simulations

performed in the section 3.3.

In terms of frequency, it is interesting to observe the spectral purity of the circuit. The contribution of higher harmonics to the signal could lead to a modification of the performances of the quadrupole (even if this has been shown to be negligible below a factor of 40 dB, see section 4.2). A signal has been recorded at 1.2 MHz on an oscilloscope and its spectrum, obtained thanks to a Fast Fourier Transform (FFT), is shown in Figure 5.4. One can see that the sinusoidal signal presents some tiny oscillations, leading to really high frequency contributions. Also, during the recording, an external contribution of 50 Hz has been observed on the oscilloscope, translated into an increase of the amplitude of the spectrum close to 0. Still, both effects are negligible while thinking about the performances of the quadrupole.

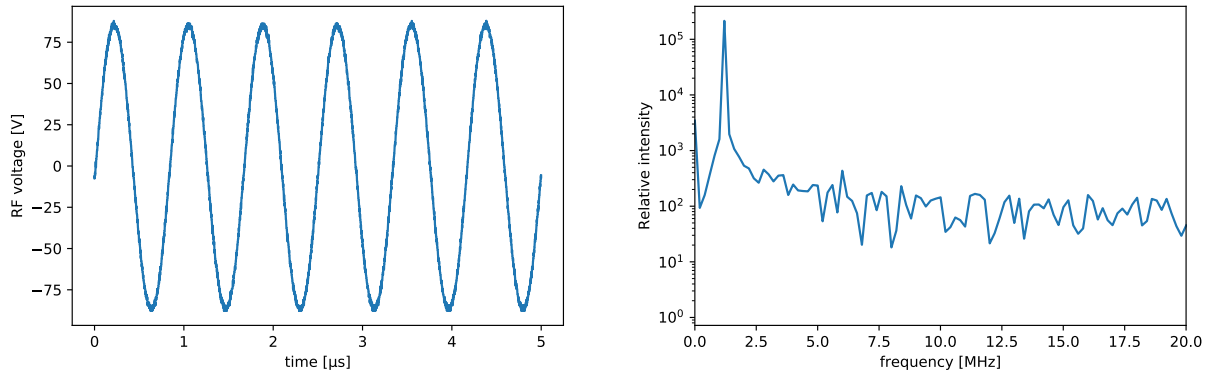

(a) (b)

Figure 5.4: (a) Output signal from the resonant LC circuit and (b) its fast Fourier transform (FFT).

One can observe that the frequency of 1.2 MHz is really intense. Above that, it is quite difficult to observe the contribution of any higher harmonics due to the noise on the spectrum. However, no clear peak is observed on the second, third or any higher harmonic: the higher harmonics contributions are clearly below the critical threshold of 40 dB.

Another interesting characteristic of such an electrical circuit is the quality (or Q) factor. It is defined as:

$$Q = \frac{f}{\Delta f} \tag{5.2}$$

with f the frequency of the peak and Δf the width of the peak at -3 dB, i.e. at 0.707 of the height of the peak. At a peak frequency of 1 MHz, a width of $\Delta f = 90$ kHz has been observed, leading to a quality factor of $Q = 11$.

One final point of interest regarding the electronics is the performance in terms of mass-over-charge ratio that it can select. Thinking about the Mathieu coefficients, the stability of an ion trajectory is determined by the RF and DC voltages and the RF frequency. It can be observed that the DC contribution is always smaller than the RF one: the RF voltage is the limiting factor. Therefore, a graph of the RF voltage as a function of the RF frequency has been constructed given a particular operating point and for several masses. Two operating points have been selected: the apex and the maximal value of q_u. The masses correspond to the $[(CO_2)_n\text{-}(H_2O)_n]^+$ complexes. The result is shown in Figure 5.5.

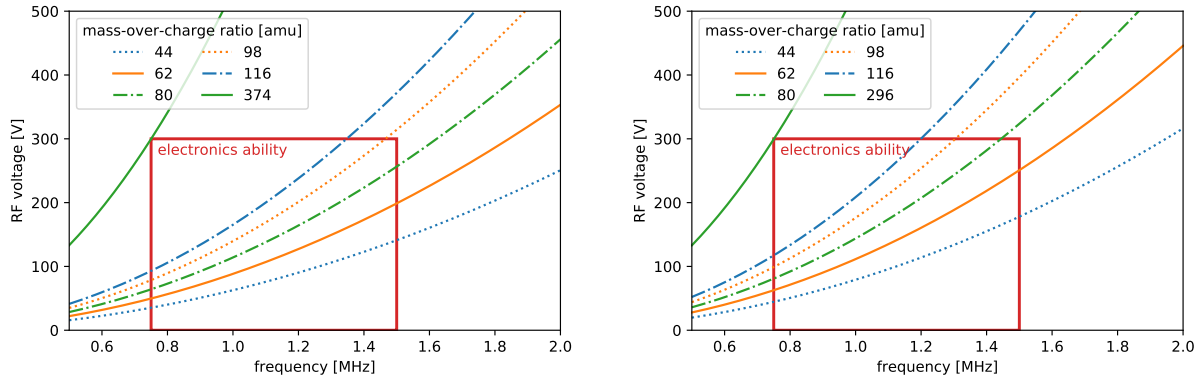

(a) (b)

Figure 5.5: RF voltage versus RF frequency for typical ion masses at two critical stability points: (a) at the apex and (b) at the maximal q_u value. The red box includes the achievable conditions by the electronics.

It can be observed that each mass up to $m/z = 116$ amu can be selected for a certain attainable RF voltage and frequency combination. The only limitation lies in the frequencies that can be used for higher masses, which are limited. This is actually not a good news in terms of resolution because R is proportional to the square of the frequency (or should be, even if this square law is not verified in Figure 4.8). Finally, the maximal m/z ratio that can be selected at the apex in the most extreme case (i.e. V = 300 V and f = 0.75 MHz) is $m/z = 374$ amu. In the case of a RF-only system, the maximal value is $m/z = 296$ amu.

5.3 Conditions for continuous excitation

One of the objectives, in the new experiment to be built, is to drastically improve the resolution of the obtained spectra. The spectral resolution of the actual pulsed dye laser can be determined thanks to a recorded N_2O^+ spectrum as shown in Figure 5.6. The full width at half maximum of the main peak (at 30 908 cm^{-1}) has been deduced and is equal to $(\delta\nu)_{dye}$ = 0.62 cm^{-1}. This value is actually overestimated with respect to the linewidth of the dye

laser, which is $(\delta\nu)_{dye,real} = 0.05$ cm^{-1}, then frequency doubled (consequently doubling the linewidth). The velocity of the ions and the poor statistics of the obtained spectrum are also increasing that value of 0.62 cm^{-1}. With the DFB laser instead, a spectral resolution around $(\delta\nu)_{DFB} = 6.10^{-5}$ cm^{-1} should be attainable. It means that a new setup involving a DFB laser as a light source could improve the resolution by a factor of at least 10^2 and up to 10^4 by considering the unfavourable case of the spectrum shown in Figure 5.6, which is significant. Moreover, if the valve operates at a pulse rate of 1 kHz instead of 30 Hz for the actual experiment, the Gaussian noise, scaling in $\sqrt{N}$, is reduced by a factor of $\sqrt{1000}/\sqrt{30} = 5.77$.

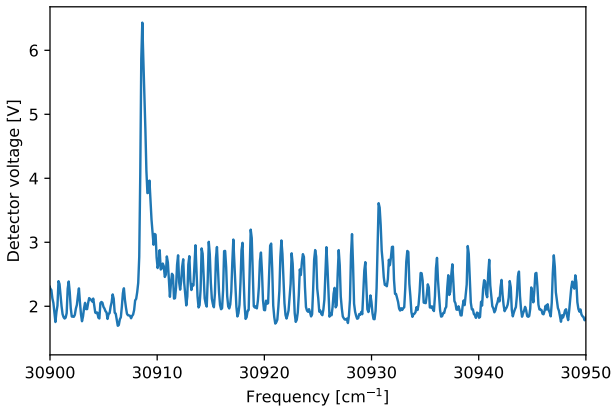

Figure 5.6: Part of a recorded spectrum of N_2O^+ on the current experimental setup.

Such a good spectral resolution is only possible with a continuous light source and a continuous excitation of the ions. The idea to derive those conditions is to take a reference experiment developed by Carré *et al.* to analyse O_2^+ [90] and then used by Abed and Larzillière to analyse N_2O^+ [91, 92]. The conditions under which they achieve a continuous excitation are transposed to the one of the future experiment involving the DFB laser. The comparison will be done also with the current experiment shown in section 5.1.

The experimental setup of Carré and Larzillière, represented in Figure 5.7, is quite different from the one presented here in the sense that they use the so-called fast ion beam laser spectroscopy (FIBLAS) technique. The ion beam of O_2^+ is accelerated up to dozens of keV and the interaction region with the laser is made of a long drift tube of length L_{drift} = 1.8 m. Given those data, the interaction time is of the order of 10 μs. The laser is a continuous wave high power Ar^+ laser (or Kr^+ in the analysis of N_2O^+). As it is mode selected with a Fabry-Pérot cavity in order to minimise its linewidth, the real power of the laser beam interacting with the ions is reduced to a few milliwatts [91]. A typical value of 10 mW is considered in the following.

The total energy transferred to the ions can be computed from the previously given data,

and knowing the wavelength of the laser ($\lambda = 496$ nm), the number of photons encountered by the ions is given by:

$$E_{transferred} = P\ t = N_{photons}\ h\ \frac{c}{\lambda} \qquad \Longrightarrow \qquad N_{photons} = 2.49\ 10^{11} \tag{5.3}$$

with P the power of the laser in [W], t the interaction time in [s], h the Planck constant in [Js], c the speed of light in vacuum in [m/s] and λ the wavelength of the laser in [m].

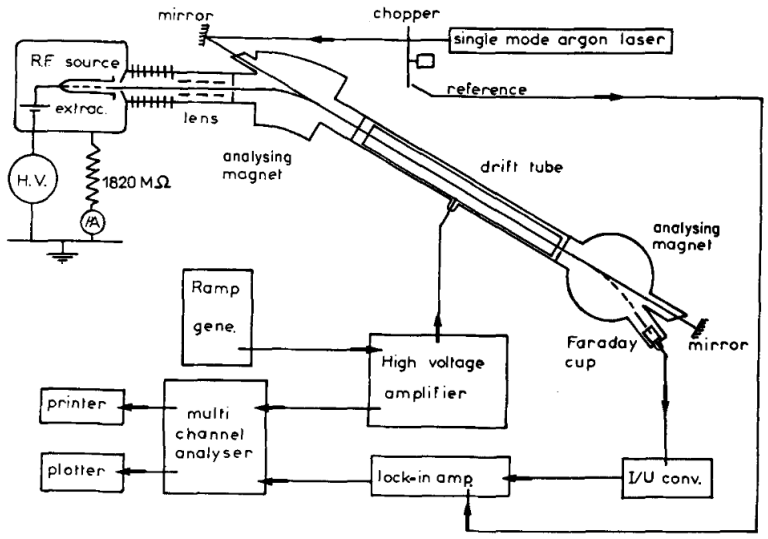

Figure 5.7: Experimental setup developed by Carré *et al.* for their FIBLAS experiment. Fig. 1 in [90].

The idea, with the new setup, is to obtain a comparable number of interacting photons in order to perform an efficient continuous excitation. To do so, two different scenarios can be developed:

1. A co-linear interaction between the laser and the ion beam is performed such as in the experiment of Carré and Larzillière.

2. A perpendicular interaction between the laser and the ion beam is achieved, such as in the current experiment.

Both scenarios are represented in Figure 5.8. In the scenario A, the ions could be trapped in order to increase their interaction time with the laser. However, the main disadvantage of such a technique is the presence of significant Doppler doublets. Therefore, this setup will not be investigated in depth in the following discussion and is let aside for further studies.

To have a better comparison point between the co-linear interaction of Carré *et al.* and the perpendicular interaction between the DFB laser and the ion beam in the new setup, it

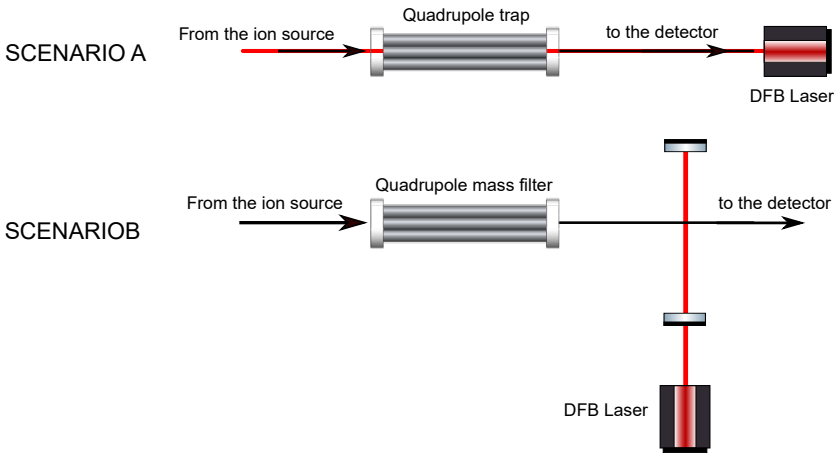

Figure 5.8: Overview of the two proposed setups to perform continuous excitation.

is better to talk in terms of photon density in the interaction region instead of the number of interacting photons. In the paper of Carré *et al.* [90], they estimated the ion beam radius to 0.5 cm in the drift tube and by assuming that the overlap between the ion beam and the laser is maximised, a radius of 0.5 cm for the laser spot is considered.

In the future experiment, the laser will be a Distributed Feedback Laser (DFB). Its power is equal to 100 mW and its wavelength stands typically around $\nu = 6550$ cm^{-1} ($\lambda = 1.53$ μm), in the near-infrared region. The diameter of the spot of the DFB laser is estimated to be close to 2 mm, it is a well collimated laser. The ion beam spot size is considered to be larger (with a radius of 2.5 mm). The interaction volume is approximated by a cylinder representing the overlap of both beams. Consequently, there is a ratio between both volumes of interaction equal to (in the scenario B):

$$\frac{V_{Carré}}{V_{DFB}} = \frac{\pi r_{spot}^2 \, L_{drift}}{\pi r_{DFB}^2 \, L_{ion}} = 9000 \tag{5.4}$$

$$\Longrightarrow \qquad N_{photons,DFB} = 9000 \; N_{photons,Carré} = 2.24 \; 10^{15} \tag{5.5}$$

with r_{spot} and r_{DFB} the radius of the Ar^+ and DFB laser respectively and L_{drift} and L_{ion} the length of interaction between the ion beam and the laser. As long as only the scenario B is studied here, L_{ion} corresponds to twice the spot radius of the ion beam, i.e. 5 mm. From that ratio, one can see that the number of photons in the interaction region has to be around 9000 times greater in the case of the new experiment.

The reverse calculation than in Equation 5.3 can be done to find the needed interaction time providing the corresponding amount of photons with the DFB laser (found in the Equation 5.5). This leads to:

$$E_{transferred} = N_{photons} \; h \; \frac{c}{\lambda_{DFB}} = 0.29 \; mJ \qquad \Longrightarrow \qquad t_{int} = \frac{E_{transferred}}{P_{DFB}} = 2.91 \; ms \tag{5.6}$$

It turns out that to obtain the same number of interacting photons (scaled with the interaction volume), the DFB laser has to irradiate the ions during 2.91 ms.

This interaction time can also be compared with the current setup and the pulsed DCM dye laser. With that setup, the interaction time is 10 ns (the time of the pulse of the dye laser), the energy in the pulse is 1 mJ in the best case and its operating frequency stands around $\nu = 30\ 000\ \text{cm}^{-1} = 899$ THz. The number of interacting photons per unit time is then:

$$\frac{N_{photons,DCM}}{t_{pulse}} = \frac{E}{h\nu} = 1.67\ 10^{15}\ photons/10ns = 1.67\ 10^{23}\ photons/s \tag{5.7}$$

In the case of the continuous DFB laser with a perpendicular interaction between the ion beam and the laser, this number of photons per unit time is given by:

$$N_{photons,DFB} = \frac{P_{DFB}}{h\nu} = 7.7\ 10^{17}\ photons/s \tag{5.8}$$

There is a clear difference between both cases, implying an interaction time of the DFB laser such that:

$$t_{DFB} = t_{pulse}\frac{N_{photons,DCM}}{N_{photons,DFB}} = 2.16\ ms \tag{5.9}$$

It turns out that both interaction times found in the eqs. (5.6) and (5.9) are consistent, the DFB laser has to interact around 2.5 ms with the ion beam in order to perform the continuous excitation of the ions.

To go one step further in this investigation of the scenario B, one could think about the addition of an optical cavity around the interaction region in order to increase the number of interacting photons and consequently decrease the required interaction time. This could be justified also if one wants to perform an efficient continuous excitation of $[(CO_2)_m\text{-}(H_2O)_n]^+$ complexes. This is more challenging as long as the ion beam contains typically one percent of complexes: the number of interacting photons has to be multiplied by 100 in that case. In the same way, one could think about multi-photon excitation of the ions, or the study of other rovibrational transitions having a much lower absorption cross-section. Therefore, one can see in Figure 5.8 that an optical cavity can be placed around the ion beam.

The purpose of the optical cavity is to increase the number of photons in the interaction region. That number is directly related to the finesse:

$$\mathcal{F} = \frac{\pi\sqrt{R}}{1-R} \tag{5.10}$$

with R the reflectivity of the mirrors. The finesse is proportional to the power in the cavity, itself proportional to the energy of the beam and so to the number of photons.

$$P_{cav} = P_{laser}\ \frac{\mathcal{F}}{\pi} = E_{cav}\ t_{int} \qquad \text{with} \qquad E_{cav} = N_{cav}\ h\ \frac{c}{\lambda} \tag{5.11}$$

$$\Longrightarrow N_{cav} = P_{laser}\frac{\lambda}{hc}\frac{\sqrt{R}}{1-R}t_{int} \tag{5.12}$$

This number of photons is mainly dependent on the reflectivity of the mirrors and of course of the interaction time between the ions and the laser. A graph of the number of photons as a function of the interaction time for several reflectivities is shown in Figure 5.9.

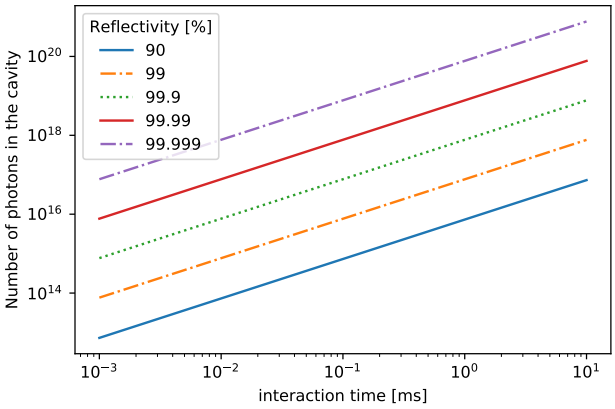

Figure 5.9: Number of photons in the cavity as a function of the interaction time for several reflectivities of the mirrors. Both axis are in a logarithmic scale.

The number of photons is roughly multiplied by 10 for each reflectivity increment. It can be observed that the required number of photons is reached for a short interaction time (1 μs) if the reflectivity of the mirrors is equal to or above R = 99.99%. Also, a sufficient amount of photons is provided for an interaction time of 0.3 ms even for the lowest reflectivity considered (i.e. 90 %): even with a relatively low reflectivity of the mirrors, the interaction time can be reduced by a factor of 8. Still, the width of a cavity mode is different than the one of the laser itself: a scaling factor has to be computed.

As it has been said before, the linewidth of the DFB laser is considered to be close to $(\delta\nu)_{DFB} \simeq 6.10^{-5}$ cm^{-1} = 1.8 MHz. In an optical cavity, the linewidth of the selected mode can be derived considering again the finesse, expressed in the following form:

$$\mathcal{F} = \frac{(\Delta\nu)_{FSR}}{(\delta\nu)_{FWHM}} \tag{5.13}$$

with $(\Delta\nu)_{FSR}$ corresponding to the free spectral range of the cavity and $(\delta\nu)_{FWHM}$ the linewidth of the mode. Knowing that $(\Delta\nu)_{FSR} = c/2L_{cav}$, the linewidth of the cavity can be easily computed. A cavity length of L_{cav} = 0.3 m has been considered in the following: it corresponds to a typically achievable length in the future experimental setup. Again, the number of photons depends on the same parameters than before, i.e. the reflectivity of the

mirrors and the interaction time.

The scaling coefficient is obtained by computing the overlap integral of both signals, considering a Lorentzian lineshape of equation:

$$L(\nu) = \frac{1}{\pi} \frac{\left(\frac{\delta\nu}{2}\right)}{\left(\nu^2 + \left(\frac{\delta\nu}{2}\right)^2\right)} \tag{5.14}$$

with ν the peak frequency of the mode and $\delta\nu$ its FWHM. The overlap integral has been computed thanks to a *Python* script and the result is graphically depicted in Figure 5.10a for different length of the optical cavity. For a length of 0.3 m, it can be seen that the overlap integral is still perfect for reflectivities of 90% and 99% but is way smaller for higher values of R. It has been considered that the scaling factor is proportional to the number of photons injected into the cavity. That scaled number of photons in the cavity is represented in Figure 5.10b.

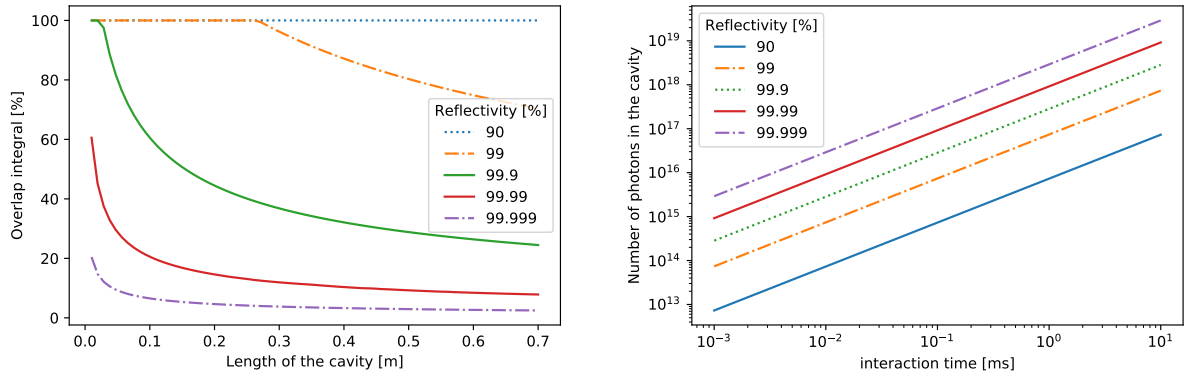

(a) (b)

Figure 5.10: (a) Overlap integral between both lorentzian lineshapes modes as a function of the length of the optical cavity for different reflectivities and (b) the corresponding number of photons as a function of the interaction time and for a defined length (L_{cav} = 0.3 m).

The number of photons in the cavity is no more multiplied by 10 at each reflectivity increment: it tends to saturate when reflectivity increases. This is due to the fact that with a high reflectivity of the mirrors, the finesse of the cavity is really high and consequently its lineshape is really narrow. Due to the scaling factor, the conditions under which a sufficient number of photons interact with the ion beam are more challenging. An optical cavity with 99.99% reflectivity for the mirrors can be used but with an interaction time of around 2 μs. As long as the scaling factor does not impact lower reflectivities of 90% and 99%, the interaction time with those values is kept at 0.3 ms and 30 μs respectively.
In order to optimise the system, the value of the scaling factor could be increased thanks to another adjustment: locking the laser mode on the cavity thanks to a feedback, for example

by means of the Pound-Drever-Hall (PDH) [93] or the tilt-locking [94] technique.

As a conclusion, continuous excitation is possible with a perpendicular excitation between the ion beam and the laser. The number of photons that is required can be attained by interacting during 2.5 ms with the ion beam. To extend the model further and reduce this interaction time, the addition of an optical cavity has been discussed. The conclusion is that the higher the reflectivity, the shorter the required interaction time. If the interaction cross-section between the laser and the ion beam is optimised, an interaction time of only 10 μs could be sufficient, just as in the case of Larzillière and Carré.

5.4 The miniaturised quadrupole

The purpose of this section is to show how to implement a smaller quadrupole device and why this is interesting in such an experiment. What is meant by miniaturised is a quadrupole that remains macroscopic: its free radius r_0 is typically reduced by a factor of 2.

5.4.1 Motivations

The interests in the quadrupole miniaturisation, in this experiment, are the following. Firstly, thinking about the Mathieu coefficients a_u and q_u, the $1/r_0^2$ factor will increase (see Equation 2.26). This means that, with the same electronics, i.e. the same peak-to-peak voltage amplitude, one will be able to manipulate ions of much higher masses. This is even more interesting given the fact that the relation between r_0 and m is quadratic. For example, if r_0 is divided by a factor of two, the higher mass that could be selected will be 1 496 amu: it opens up opportunities in the study of organic molecules or even relatively small macromolecules. On the other hand, if one would like to build a new electrical circuit for the same mass range as before, the frequency and/or DC and RF potentials to supply are significantly reduced. Again, the relation is quadratic for the potentials but linear for the frequency (see Equation 2.26).

Also, this smaller quadrupole is necessary in the new experimental setup if a second mass filter is used after the laser interaction for example. This situation is represented in Figure 5.11. This quadrupole could also be used as a trapping system for further experimental developments.

Still, the main disadvantage of such a device is its acceptance: the ion beam has to be strongly focused before entering such a small quadrupole. The addition of focusing electrodes before the quadrupole can manage this problem but this is important to consider while building the setup. Also, even if the dimensions are still reasonable, one has to think about the mechanical alignment and the precision of the dimensions of the rods. As it has been shown in several studies [86, 95, 96], a small misalignment or a small imperfection in

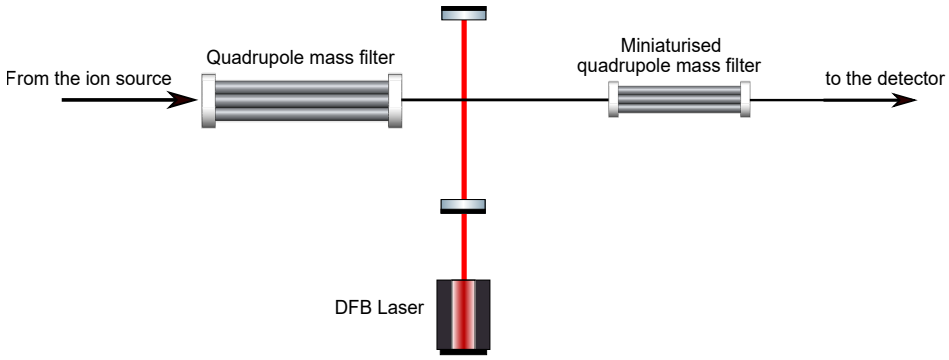

Figure 5.11: Example of experiment where the small quadrupole could be used. It is placed after the laser interaction in the scenario B of the Figure 5.8.

the manufacture of the rods can lead to a significant decrease in resolution.

So the motivations in the design of a smaller quadrupole are clear: it simplifies the electronics and/or opens interesting perspective in terms of the reachable mass range.

5.4.2 Design

The quadrupole design is comparable to the one already described in this work, but at a smaller scale. It is again made of four stainless steel rods positioned symmetrically with respect to the center of the quadrupole. One important question here is the mechanical tolerance of the rods required to avoid any field imperfection. Rectified stainless steel rods can be easily found with a good tolerance. In this case, stainless steel bars with a H7 tolerance have been chosen. Those bars can be found in any hardware store, such as ESSE Diffusion for instance[1]. Given a diameter of the rods equal to 6 mm, it means that their precision is 6 ± 0.012 mm. In the study of Austin *et al.*, the resolution of a quadrupole mass filter is shown as scaling in $R \propto (error)^{-n}$ with $n \simeq 1.3$. This would lead to a maximal attainable resolution close to $R = 1300$.

The inner free radius, r_0, has been determined given the ideal conditions: $r/r_0 = 1.1468$. This is the condition under which the ideal hyperbolic rods are well approximated by cylindrical ones in terms of potential. As it has been shown in the section 4.2, the resolution is slightly better with an ideal quadrupole. Also, it allows a better mathematical description and comprehension of the underlying associated phenomena.

Two insulating parts hold on the rods in their symmetric positions. Several discussion have been made about the right material to choose for this kind of insulator and it turns

[1]See "ROND PLEIN ACIER STUB BARRE RONDE 100C6 RECTIFIÉ H7 - ESSE Diffusion", url: `http://www.esse.fr/epages/xsisunlz.sf/fr_FR/?ObjectPath=/Shops/xsisunlz/Products/BAZ/SubProducts/BAZ-0070`, accessed on 05-06-2020.

out that PEEK seems to be the more appropriate one. It combines brilliantly all the requirements for the quadrupole: it can be precisely and easily machined, it has a low dilatation coefficient, it is relatively cheap compared to other ceramics and it is chemical and hydrolysis resistant.

The main characteristics of the miniaturised quadrupole are indicated on a first sketch shown in Figure 5.12.

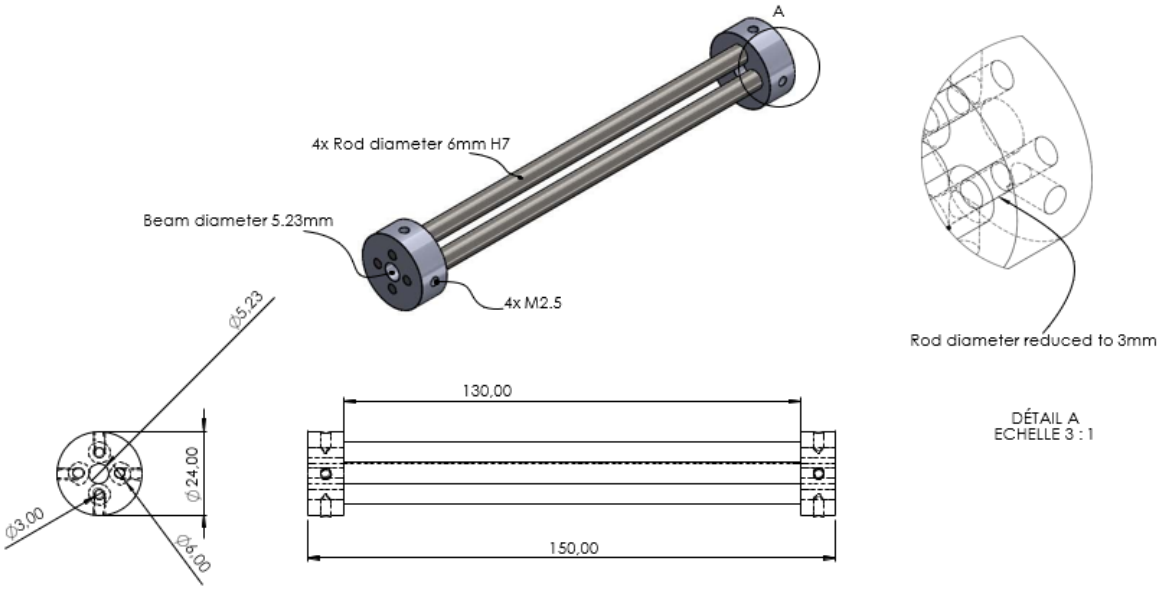

Figure 5.12: SolidWorks plan of the miniaturised quadrupole with its main dimensions.

In terms of electronic contacts between the rods and the external circuit, two main options are under discussion. The first one is the same as in the actual quadrupole. The idea is to drill a small hole at the end of each rod, to insert and glue (or weld) a female electrical pin and to plug the physical male connector into it. The drawback of this technique stays in the drilling of a hole in such a small rod. Also, one has to make sure that the female pin is well glued into the rod, which might be difficult to ensure considering those dimensions. A perfect electrical contact being an essential part of the quadrupole design (it avoids harmonics generation, electrical losses, etc.), another option deserves to be investigated. The second idea is to make an indirect link between the rods and the electric circuit. One can make use of the pressure screws holding the whole structure together. Those screws are directly in contact with the rods by passing through the PEEK. This kind of setup can avoid all the previously mentioned drawbacks and simplifies the manufacture of the quadrupole.

Finally, an outer cap has to hold the whole structure together before putting it in the

final setup. It has been shown [11] that the outer cap dimensions does not influence the potential distribution in the interaction region (i.e. between the rods) so this point is not of major importance. The addition of a shielding element at both ends of the quadrupole can be discussed in order to minimise the fringing fields region.

Chapter 6

Conclusion and perspectives

This work has investigated the characterisation of a quadrupole device, from its mathematical description to its experimental implementation, passing through a set of simulations showing its general behaviour and abilities. Quadrupoles and more generally multipolar devices are common in ion spectroscopy experiments. Here, three different regimes of the quadrupole have been explored: the guiding, the mass filtering and the trapping of ions.

The theoretical formalism about the quadrupole and the multipolar field elements in general has been presented. The quadrupole is easier to study theoretically with respect to higher order multipolar devices: the equations of motion for an ion travelling into a quadrupole are decoupled. Those equations are of the Mathieu type, a special form of Hill's equation. The stability of the solution depends on two parameters, a_u and q_u, related to the RF and DC voltages applied to the rods, to the RF frequency, to the field-free radius between the electrodes and to the mass-over-charge ratio of the studied ion. In the case of higher order multipoles, the equations are not decoupled anymore and the stability depends also on the initial conditions of the ion, i.e. its position and velocity vectors.

The simulation formalism has been presented, with the use of SIMION on the one hand and with the use of a *Python* code on the other hand. In SIMION, two quadrupoles have been studied: quadrupole A, corresponding to the one used in the laboratory experiment and quadrupole B, corresponding to a quadrupole with an ideal r/r_0 ratio. This means that the geometry of the quadrupole B is such that round rods reproduce accurately the desired hyperbolic field shape. The quadrupole C has been modeled with a self-made code in *Python*: it corresponds to the perfectly hyperbolic design and consequently it obeys exactly to the Mathieu equation.

In the section 3.3, the stability diagram of the quadrupole A has been computed, presenting a small shift to the lower q values with respect to the theory. This shift is explained by the shape of the electric field into the quadrupole A, which is not perfectly hyperbolic: the potential is the sum of 4^{th}, 12^{th}, 20^{th}, etc. order terms, the contribution of each term being explicited by the derivation of a C_n coefficient. This non-ideal behaviour has been translated

numerically by computing those coefficients representing the higher order contributions to the potential. The stability triangle of the quadrupole A has been compared to the quadrupoles B and C. In the case of the quadrupole B, the shift is still present but it is way smaller than the one of the quadrupole A: the higher order contributions to the potential are minimised. Finally, the quadrupole C is perfectly obeying the theory: it is a direct solution of the Mathieu equation.

The quadrupole A has been studied more deeply in order to prove its possible use as an ion guide, as a mass filter or as an ion trap. The ion guiding is possible for two purposes. An ion guide can operate as a high-pass mass filter or as a focusing element.
Then, a complete discussion about mass resolution has been done, showing that the quadrupole A has a low resolution ($R \simeq 60$) compared to commercial quadrupoles ($R \simeq 1000$). However, this relatively low resolution does not prevent its use as a mass filter. The optimisation of several parameters such as the RF frequency, the kinetic energy of the ions, etc. could slightly improve that value.
The ion trapping has been discussed with its implementation in the homemade *Python* script. In SIMION, the effect of the voltage of the electrodes and the focusing effect have been discussed, showing that trapping is possible during 1 millisecond under two conditions. Firstly, the voltage of the electrodes has to be relatively high and secondly, the operating condition has to be relatively far from any limit of the stability triangle.
The *Python* code has finally been extended to the ability to compute the trajectory of an ion in any multipolar device, opening great opportunities for further simulation studies.

The actual experimental setup has been shown in the chapter 5. The new setup, including the quadrupole A, has been briefly introduced by outlining the modifications and adaptations between that experiment and the currently used one. One of the objectives of the new experiment is to drastically improve the spectral resolution of the obtained rovibrational spectra. This can be done thanks to a DFB laser and with a continuous excitation of the ion beam. Moreover, a higher pulse rate from the valve can reduce the acquisition time and/or improve the signal-to-noise ratio of the spectrum. It has been proven that continuous excitation is possible with a perpendicular interaction between the laser and the ion beam and that it can be improved with the addition of an optical cavity around the interaction region.

As a final step, the design of a new quadrupole has been presented, smaller than the quadrupole A. The interest of a smaller quadrupole is mainly regarding the lower peak voltage required from the electronics. It also opens interesting opportunities in the study of much larger molecular ions. Both the quadrupole A and a miniaturised quadrupole should be installed in the future experimental setup in the laboratory: it will allow one to perform two mass selections or both a mass selection and an ion trapping for example.

As a further step, one could investigate the higher order multipoles in more detail. Ion trapping can be analysed in *Python* for multipolar elements of any order. In those traps,

the collisional processes and the space charge effects have not been studied yet. It is clear that ion-ion collisions happen during their trapping time. These collisional processes can be extended to the numerical study of buffer gas cooling, allowing one to implement trapping at cryogenic temperatures. Those simulations would be the first step before an experimental implementation of such a cold head.

The results in this master thesis show that a quadrupole is a versatile tool that can be used in high-resolution spectroscopy experiments. It is hoped that the simulation results and the simulation tools developed in this work will allow one to develop, in this laboratory, the existing experimental setup further and will also contribute to the development of ionic spectroscopy of molecular species.

Bibliography

[1] W. Paul and M. Raether. Das elektrische massenfilter. *Zeitschrift für Physik*, 140(3):262–273, 1955.

[2] W. Paul. Electromagnetic traps for charged and neutral particles. Nobel Lecture, 1989. available on `https://www.nobelprize.org/uploads/2018/06/paul-lecture.pdf`.

[3] H.G. Dehmelt. Radiofrequency spectroscopy of stored ions i: Storage **part ii: Spectroscopy is now scheduled to appear in volume v of this series. volume 3 of *Advances in Atomic and Molecular Physics*, pages 53 – 72. Academic Press, 1968.

[4] P. Jusko, A. Stoffels, S. Thorwirth, S. Brünken, S. Schlemmer, and O. Asvany. High-resolution vibrational and rotational spectroscopy of CD_2H^+ in a cryogenic ion trap. *Journal of Molecular Spectroscopy*, 332:59–66, 2017.

[5] S. Brünken, L. Kluge, A. Stoffels, J. Pérez-Ríos, and S. Schlemmer. Rotational state-dependent attachment of He atoms to cold molecular ions: An action spectroscopic scheme for rotational spectroscopy. *Journal of Molecular Spectroscopy*, 332:67–78, 2017.

[6] P.H. Dawson. *Quadrupole Mass Spectrometry and its Applications*. Elsevier Scientific Publishing Company, 1976.

[7] D. Gerlich. Inhomogeneous rf fields: A versatile tool for the study of processes with slow ions. In *Advances in Chemical Physics*, pages 1–176. John Wiley & Sons, Ltd, 1992.

[8] F. M. Ma and S. Taylor. Simulation of ion trajectories through the mass filter of a quadrupole mass spectrometer. *IEE Proceedings - Science, Measurement and Technology*, 143(1):71–76, 1996.

[9] J. R. Gibson and S. Taylor. Prediction of quadrupole mass filter performance for hyperbolic and circular cross section electrodes. *Rapid Communications in Mass Spectrometry*, 14(18):1669–1673, 2000.

[10] J. R. Gibson and S. Taylor. Numerical investigation of the effect of electrode size on the behaviour of quadrupole mass filters. *Rapid Communications in Mass Spectrometry*, 15(20):1960–1964, 2001.

[11] J. R. Gibson, S. Taylor, and J. H. Leck. Detailed simulation of mass spectra for quadrupole mass spectrometer systems. *Journal of Vacuum Science & Technology A: Vacuum, Surfaces, and Films*, 18(1):237–243, 2000.

[12] S. Bize, S. A. Diddams, U. Tanaka, C. E. Tanner, W. H. Oskay, R. E. Drullinger, T. E. Parker, T. P. Heavner, S. R. Jefferts, L. Hollberg, W. M. Itano, and J. C. Bergquist. Testing the stability of fundamental constants with the $^{199}Hg^{+}$ single-ion optical clock. *Phys. Rev. Lett.*, 90:150802, 2003.

[13] D. Leibfried, R. Blatt, C. Monroe, and D. Wineland. Quantum dynamics of single trapped ions. *Reviews of Modern Physics*, 75(1):281–324, 2003.

[14] O. Boyarkin, S. R. Mercier, A. Kamariotis, and T. R. Rizzo. Electronic spectroscopy of cold, protonated tryptophan and tyrosine. *Journal of the American Chemical Society*, 128(9):2816–2817, 2006.

[15] N. S. Nagornova, T. R. Rizzo, and O. V. Boyarkin. Interplay of Intra- and Intermolecular H-Bonding in a Progressively Solvated Macrocyclic Peptide. *Science*, 336(6079):320–323, 2012.

[16] G. Siuzdak, B. Bothner, M. Yeager, C. Brugidou, C. M. Fauquet, K. Hoey, and C. M. Chang. Mass spectrometry and viral analysis. *Chemistry and Biology*, 3:45–48, 1996.

[17] B. Gologan, J. M. Wiseman, and R. G. Cooks. Ion Soft Landing: Instrumentation, Phenomena, and Applications. In Julia Laskin and Chava Lifshitz, editors, *Principles of Mass Spectrometry Applied to Biomolecules*, chapter 12, pages 433–474. John Wiley edition, 2006.

[18] D. J. Wineland, W. M. Itano, and R. S. Van Dyck. High-resolution spectroscopy of stored ions. *Advances in Atomic and Molecular Physics*, 19(C):135–186, 1983.

[19] D. J. Wineland. Trapped ions, laser cooling, and better clocks. *Science*, 226(4673):395–400, 1984.

[20] D. J. Wineland, C. Monroe, W. M. Itano, D. Leibfried, B. E. King, and D. M. Meekhof. Experimental Issues in Coherent Quantum-State Manipulation of Trapped Atomic Ions. *Journal of Research of the National Institute of Standards and Technology*, 103(3):259–328, 1998.

[21] D. Kielpinski, C. Monroe, and D. J. Wineland. Architecture for a large-scale ion-trap quantum computer. *Nature*, 417(6890):709–711, 2002.

[22] C. R. Monroe and D. J. Wineland. Quantuum computing with ions. *Scientific American*, 299(2):64–71, 2008.

[23] S. Sturm, I. Arapoglou, A. Egl, M. Höcker, S. Kraemer, T. Sailer, B. Tu, A. Weigel, R. Wolf, J. C. López-Urrutia, and K. Blaum. The ALPHATRAP experiment. *The European Physical Journal Special Topics*, 227(13):1425–1491, 2019.

[24] M. S. Safronova. Mass spectrometry for future atomic clocks. *Nature*, 581:35–36, 2020.

[25] R. X. Schüssler, H. Bekker, M. Braß, H. Cakir, J. R. C. López-urrutia, M. Door, P. Filianin, Z. Harman, M. W. Haverkort, W. J. Huang, P. Indelicato, C. H. Keitel, C. M. König, K. Kromer, M. Müller, Y. N. Novikov, A. Rischka, C. Schweiger, S. Sturm, S. Ulmer, S. Eliseev, and K. Blaum. Detection of metastable electronic states by Penning trap mass spectrometry. *Nature*, 581:3–8, 2020.

[26] D. Gerlich and S. Horning. Experimental Investigations of Radiative Association Processes as Related to Interstellar Chemistry. *Chemical Reviews*, 92(7):1509–1539, 1992.

[27] D. Gerlich. Experimental investigations of ion-molecule reactions relevant to interstellar chemistry. *Journal of the Chemical Society, Faraday Transactions*, 89(13):2199–2208, 1993.

[28] D. Gerlich. Ion-neutral collisions in a 22-pole trap at very low energies. *Physica Scripta*, T59:256–263, 1995.

[29] W. Paul, B. Lücke, S. Schlemmer, and D. Gerlich. On the dynamics of the reaction of positive hydrogen cluster ions (H_5^+ to H_{23}^+) with para and normal hydrogen at 10 K. *International Journal of Mass Spectrometry and Ion Processes*, 149-150(C):373–387, 1995.

[30] H. Kreckel. *Internal excitations of stored triatomic hydrogen molecular ions*. PhD thesis, Rupertus Carola University of Heidelberg, 2003.

[31] S. S. Kumar, F. Grussie, Y. V. Suleimanov, H. Guo, and H. Kreckel. Low temperature rates for key steps of interstellar gas-phase water formation. *Science Advances*, 4(6):1–7, 2018.

[32] O. Asvany, O.r Ricken, H. S.P. Müller, M. C. Wiedner, T. F. Giesen, and S. Schlemmer. High-resolution rotational spectroscopy in a cold ion trap: H_2D^+ and D_2H^+. *Physical Review Letters*, 100(23):13–16, 2008.

[33] E. K. Campbell, M. Holz, D. Gerlich, and J. P. Maier. Laboratory confirmation of C_60^+ as the carrier of two diffuse interstellar bands. *Nature*, 523(7560):322–323, 2015.

[34] O. Asvany, S. Brünken, L. Kluge, and S. Schlemmer. COLTRAP: A 22-pole ion trapping machine for spectroscopy at 4 K. *Applied Physics B: Lasers and Optics*, 114(1-2):203–211, 2014.

[35] M. Yamashita and J. B. Fenn. Electrospray ion source. another variation on the free-jet theme. *The Journal of Physical Chemistry*, 88(20):4451–4459, 1984.

[36] J. B. Fenn, M. Mann, C. K. Meng, S. F. Wong, and C. M. Whitehouse. Electrospray ionization–principles and practice. *Mass Spectrometry Reviews*, 9(1):37–70, 1990.

[37] M. Karas and F. Hillenkamp. Laser desorption ionization of proteins with molecular masses exceeding 10,000 daltons. *Analytical Chemistry*, 60(20):2299–2301, 1988.

[38] M. W. F. Nielen. Maldi time-of-flight mass spectrometry of synthetic polymers. *Mass Spectrometry Reviews*, 18(5):309–344, 1999.

[39] T. R. Rizzo, J. A. Stearns, and O. V. Boyarkin. Spectroscopic studies of cold, gas-phase biomolecular ions. *International Reviews in Physical Chemistry*, 28(3):481–515, 2009.

[40] V. Franchetti, B. H. Solka, W. E. Baitinger, J. W. Amy, and R. G. Cooks. Soft landing of ions as a means of surface modification. *International Journal of Mass Spectrometry and Ion Physics*, 23(1):29–35, 1977.

[41] S. A. Miller, H. Luo, S. J. Pachuta, and R. G. Cooks. Soft-landing of polyatomic ions at fluorinated self-assembled monolayer surfaces. *Science*, 275(5305):1447–1450, 1997.

[42] K. Bromann, C. Félix, H. Brune, W. Harbich, R. Monot, J. Buttet, and K. Kern. Controlled deposition of size-selected silver nanoclusters. *Science*, 274(5289):956–958, 1996.

[43] B. E. Winger, H. J. Laue, S. R. Horning, R. K. Julian, S. A. Lammert, D. E. Riederer, and R. G. Cooks. Hybrid BEEQ tandem mass spectrometer for the study of ion/surface collision processes. *Review of Scientific Instruments*, 63(12):5613–5625, 1992.

[44] O. Hadjar, P. Wang, J. H. Futrell, Y. Dessiaterik, Z. Zhu, J. P. Cowin, M. J. Iedema, and J. Laskin. Design and performance of an instrument for soft landing of biomolecular ions on surfaces. *Analytical Chemistry*, 79(17):6566–6574, 2007.

[45] Z. Ouyang, Z. Takáts, T. A. Blake, B. Gologan, A. J. Guymon, J. M. Wiseman, J. C. Oliver, V. J. Davisson, and R. G. Cooks. Preparing protein microarrays by soft-landing of mass-selected ions. *Science*, 301(5638):1351–1354, 2003.

[46] T. A. Blake, Z. Ouyang, J. M. Wiseman, Z. Takáts, A. J. Guymon, S. Kothari, and R. G. Cooks. Preparative linear ion trap mass spectrometer for separation and collection of purified proteins and peptides in arrays using ion soft landing. *Analytical Chemistry*, 76(21):6293–6305, 2004.

[47] M. A. Tito, K. Tars, K. Valegard, J. Hajdu, and C. V. Robinson. Electrospray time-of-flight mass spectrometry of the intact MS2 virus capsid. *Journal of the American Chemical Society*, 122(14):3550–3551, 2000.

[48] S. D. Fuerstenau, W. H. Benner, J. J. Thomas, C. Brugidou, B. Bothner, and G. Siuzdak. Mass Spectrometry of an Intact Virus. *Angewandte Chemie International Edition*, 40(6):982–982, 2001.

[49] E. Forsberg, M. Fang, and G. Siuzdak. Staying Alive: Measuring Intact Viable Microbes with Electrospray Ionization Mass Spectrometry. *Journal of the American Society for Mass Spectrometry*, 28(1):14–20, 2017.

[50] P.H. Dawson and N.R. Whetten. Mass Spectroscopy Using RF Quadrupole Fields. volume 27 of *Advances in Electronics and Electron Physics*, pages 59 – 185. Academic Press, 1970.

[51] R. E March and R. J Hughes. *Quadrupole storage mass spectrometry*. Chem. Anal. Wiley, New York, NY, 1989.

[52] E. Mathieu. Mémoire sur le mouvement vibratoire d'une membrane de forme élliptique. *Journal de Mathématiques Pures et Appliquées*, 13:137–203, 1868.

[53] I. Panardo. Stability of periodic systems and floquet theory. Master's thesis, Università degli Studi di Padova, 2014.

[54] R. H. Rand. Mathieu's Equation. In *CISM Course: Time-Periodic Systems*, Udine, Italy, 2016.

[55] F. G. Major, V. N. Gheorghe, and G. Werth. *Charged particle traps: physics and techniques of charged particle field confinement*. Springer series on atomic, optical, and plasma physics. Springer, Berlin, 2005.

[56] F. M Arscott, I N Sneddon, M Stark, and S Ulam. *Periodic differential equations: an introduction to Mathieu, Lamé, and allied functions*. Internat. Ser. Mono. Pure Appl. Math. Pergamon, London, 1964.

[57] T. Tamir. Characteristic Exponents of Mathieu Functions. *Mathematics of Computation*, 16(77):100, 1962.

[58] K. Maeda, A. Fuduka, and M. Sakimura. Tables relating to mathieu functions appearing in mass filter problem. *Journal of the Mass Spectrometry Society of Japan*, 17(1):530–574, 1969.

[59] K. L. Hunter and B. J. McIntosh. An improved model of the fringing fields of a quadrupole mass filter. *International Journal of Mass Spectrometry and Ion Processes*, 87:157–164, 1989.

[60] P. H. Dawson. Fringing Fields in Quadrupole-Type Mass Analyzers. *Journal of Vacuum Science and Technology*, 9(1):487–491, 1972.

[61] R.F. Lever. Computation of ion trajectories in the monopole mass spectrometer by numerical integration of mathieu's equation. *IBM Journal of Research and Development*, 10(1):26–40, 1966.

[62] P. E Miller. The transmission properties of an RF-only quadrupole mass filter. *International Journal of Mass Spectrometry*, 72:223–238, 1986.

[63] P. E. Miller and M. B. Denton. The quadrupole mass filter: Basic operating concepts. *Journal of Chemical Education*, 63(7):617–622, 1986.

[64] I. Szabo. New ion-optical devices utilizing oscillatory electric fields. I. Principle of operation and analytical theory of multipole devices with two-dimensional electric fields. *International Journal of Mass Spectrometry and Ion Processes*, 73(3):197–235, 1986.

[65] N. R. Hutzler, H.-I Lu, and J. M. Doyle. The buffer gas beam: An intense, cold, and slow source for atoms and molecules. *Chemical Reviews*, 112(9):4803–4827, 2012.

[66] R. Wester. Radiofrequency multipole traps: tools for spectroscopy and dynamics of cold molecular ions. *Journal of Physics B: Atomic, Molecular and Optical Physics*, 42(15):154001, 2009.

[67] O. Asvany and S. Schlemmer. Numerical simulations of kinetic ion temperature in a cryogenic linear multipole trap. *International Journal of Mass Spectrometry*, 279:147–155, 2009.

[68] S. Chakrabarty, M. Holz, E. K. Campbell, A. Banerjee, D. Gerlich, and J. P. Maier. A novel method to measure electronic spectra of cold molecular ions. *Journal of Physical Chemistry Letters*, 4(23):4051–4054, 2013.

[69] O. V. Boyarkin and V. Kopysov. Cryogenically cooled octupole ion trap for spectroscopy of biomolecular ions. *Review of Scientific Instruments*, 85(3), 2014.

[70] T. R. Rizzo, S. Warnke, A. Ben Faleh, and V. Scutelnic. High-throughput cryogenic spectroscopy for glycan analysis, 2019. US Patent 10,522,337 B2.

[71] D. Dahl. D. Manura. *SIMION (R) 8.0 User Manual*. Scientific Instrument Services, Inc. Ringoes, NJ 08551, 2008.

[72] U. Even. The even-lavie valve as a source for high intensity supersonic beam. *EPJ Techniques and Instrumentation*, 2(1):17, 2015.

[73] M. Jugroot, C. P.T. Groth, B. A. Thomson, V. Baranov, and B. A. Collings. Numerical investigation of interface region flows in mass spectrometers: Neutral gas transport. *Journal of Physics D: Applied Physics*, 37(8):1289–1300, 2004.

[74] P.H. Dawson. The acceptance of the quadrupole mass filter. *International Journal of Mass Spectrometry and Ion Physics*, 17(4):423 – 445, 1975.

[75] K. Blaum, Ch Geppert, P. Müller, W. Nörtershäuser, E. W. Otten, A. Schmitt, N. Trautmann, K. Wendt, and B. A. Bushaw. Properties and performance of a quadrupole mass filter used for resonance ionization mass spectrometry. *International Journal of Mass Spectrometry*, 181(1-3):67–87, 1998.

[76] L. A. Pipes. Matrix solution of equations of the Mathieu-Hill type. *Journal of Applied Physics*, 24(7):902–910, 1953.

[77] M. Baril and A. Septier. Piégeage des ions dans un champ quadrupolaire tridimensionnel à haute fréquence. *Revue de Physique Appliquee*, 9(3):525–531, 1974.

[78] Denison D. R. Operating Parameters of a Quadrupole in a Grounded Cylindrical Housing. *J Vac Sci Technol*, 8(1):266–269, 1971.

[79] I. E. Dayton, F. C. Shoemaker, and R. F. Mozley. The Measurement of Two-Dimensional Fields. Part II: Study of a Quadrupole Magnet. *Review of Scientific Instruments*, 25(5):485–489, 1954.

[80] W. Paul, H. P. Reinhard, and U. von Zahn. Das elektrische massenfilter als massenspektrometer und isotopentrenner. *Zeitschrift für Physik*, 152(2):143–182, 1958.

[81] G. E. Lee-Whiting and L. Yamazaki. Semi-analytical calculations for circular quadrupoles. *Nuclear Instruments and Methods*, 94(2):319 – 332, 1971.

[82] J. Heinrich. *A Be^+ Ion Trap for H_2^+ Spectroscopy*. PhD thesis, Sorbonne Université, 2018.

[83] M. Sudakov and D. J. Douglas. Linear quadrupoles with added octopole fields. *Rapid Communications in Mass Spectrometry*, 17(20):2290–2294, 2003.

[84] N. Konenkov, F. Londry, C. Ding, and D. J. Douglas. Linear Quadrupoles with Added Hexapole Fields. *Journal of the American Society for Mass Spectrometry*, 17(8):1063–1073, 2006.

[85] X. Z. Zhao and D. J. Douglas. Dipole excitation of ions in linear radio frequency quadrupole ion traps with added multipole fields. *International Journal of Mass Spectrometry*, 275(1-3):91–103, 2008.

[86] W. E. Austin, A. E. Holme, and J. H. Leck. *The mass filter: design and performance*. Elsevier, Netherlands, 1976.

[87] R. E Pedder and R. A. Schaeffer. Resolution and Transmission of Quadrupoles: RF-DC and RF-Only Operation. Technical report, Extrel CMS, LLC, 1995. Application Note GT 310-D.

[88] Extrel. Quadrupole Size Comparision - Application Note RAQ110A. Technical report, Extrel CMS, LLC, 2016.

[89] M. D. Robbins, O. K. Yoon, I. Zuleta, G. K. Barbula, and R. N. Zare. Computer-controlled, variable-frequency power supply for driving multipole ion guides. *Review of Scientific Instruments*, 79(3):3–8, 2008.

[90] M. Carré, M. Druetta, M. L. Gaillard, H. H. Bukow, M. Horani, A. L. Roche, and M. Velghe. Laser spectroscopy of the O_2^+ molecular ion using a fast ion beam: Fine structure and predissociation lifetimes in the b $^4\sum_g^-$ state. *Molecular Physics*, 40(6):1453–1480, 1980.

[91] S. Abed, M. Broyer, M. Carré, M. L. Gaillard, and M. Larzilliére. Bond-Breakage Mechanism in the Predissociation of the A State of N_2O^+ : New Information from High Resolution Spectroscopy. *Physical Review Letters*, 49(2):120–124, 1982.

[92] S. Abed, M. Broyer, M. Carré, M. L. Gaillard, and M. Larzilliére. High-resolution spectroscopy of N_2O^+ in the near ultraviolet using fiblas (fast-ion-beam laser spectroscopy). *Chemical Physics*, 74(1):97–112, 1983.

[93] R. W. P. Drever, J. L. Hall, F. V. Kowalski, J. Hough, G. M. Ford, A. J. Munley, and H. Ward. Laser phase and frequency stabilization using an optical resonator. *Applied Physics B*, 31(2):97–105, Jun 1983.

[94] D. Shaddock, M. B. Gray, and D. McClelland. Frequency locking a laser to an optical cavity by use of spatial mode interference. *Optics letters*, 24:1499–501, 12 1999.

[95] P. H. Dawson and M. Meunier. Some distortions in quadrupole fields and their relation to mass filter performance. *International Journal of Mass Spectrometry and Ion Physics*, 29(3):267–299, 1979.

[96] P. H. Dawson. Quadrupole mass analyzers: Performance, design and some recent applications. *Mass Spectrometry Reviews*, 5(1):1–37, 1986.

[97] R. Kersevan and M. Ady. Recent Developments of Monte-Carlo Codes Molflow+ and Synrad+. In *Proc. 10th International Partile Accelerator Conference (IPAC'19), Melbourne, Australia, 19-24 May 2019*, number 10 in International Partile Accelerator Conference, pages 1327–1330, Geneva, Switzerland, 2019. JACoW Publishing. https://doi.org/10.18429/JACoW-IPAC2019-TUPMP037.

[98] Kurt J. Lesker Company. Technical sheets on vacuum technology, 2002. found at the address `https://www.lesker.com/leskertech/leskertech_landing.cfm`.

[99] G. Keiser. *Fundamentals of Vacuum Technology*. Cologne, 2007.

[100] J. H. Moore, C. C. Davis, and M. A. Coplan. *Building Scientific Apparatus*. Cambridge, fourth edition, 2009.

Appendix A

High vacuum generation

The aim of this appendix is to give a first overview of the design of the vacuum system for the new experimental setup. As explained in the section 5.1, the current experiment developed by R. Bejjani and A. Roucou is designed such that the gas injection is performed at a pulse rate of 30 Hz, in contrast with the new experimental setup that will inject gas at a rate of 1 kHz. The amount of gas injected in the chamber per unit of time is therefore multiplied by 33, leading to some concerns in the vacuum management.

Indeed, a high vacuum (at least 10^{-7} mbar) is required at the MCP detector in order to obtain a good signal-to-noise ratio. Thanks to that vacuum, the amount of components that might "contaminate" the spectrum, either on their own or by interacting with the photodissociated fragments, are considerably reduced.

The aim of this appendix is to analyse two possible options in order to generate a high vacuum at the MCP detector, by combining several turbomolecular pumps and differential pumping units. Only the pumping system of the chamber is considered, further investigations are needed to extend this study to a complete analysis of the system. Those more precise and more complete results should be computed thanks to the MOLFLOW+ simulation software [97] for example.

A.1 Theoretical background

A set of definitions and characteristic numbers regarding the pumping systems are widely given in the literature [98, 99, 100]. In this first section, a few of those definitions are presented to have a good theoretical background before going through the case study of the experimental system.

Pumping speed

The main parameter specified in the datasheet of a turbomolecular pump is the pumping speed, expressed as following:

$$S = \frac{dV}{dt} \tag{A.1}$$

with V the volume of gas in [L] that the pump can remove from the chamber per unit of time t in [s]. This pumping speed is mainly dependent on the type of pump, on the operating pressure of the chamber and on the pumped gas. In this study, only turbomolecular pumps will be considered. The dependence on pressure and on the nature of the gas is usually presented on the datasheet of any pump and it looks typically like the curve given in Figure A.1.

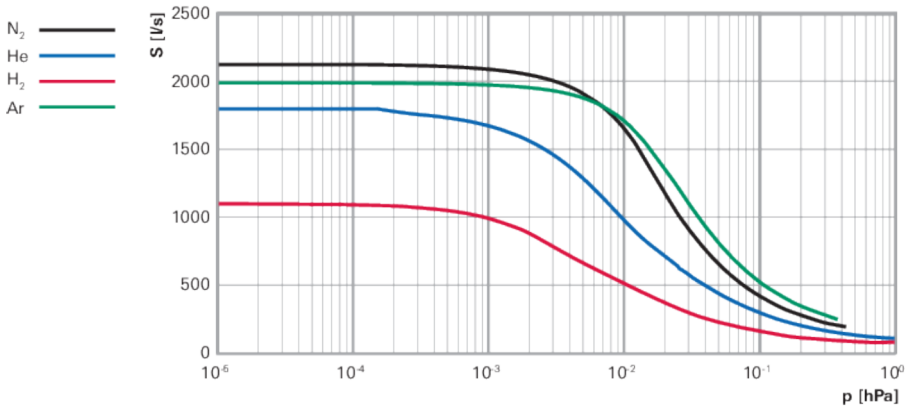

Figure A.1: Pumping speed as a function of the pressure for a typical turbomolecular pump and for several gases. This graph is taken from the datasheet of the turbomolecular pump ATH 2300 of Pfeiffer Vacuum.

Gas throughput

In order to know the pumping speed required for a certain pressure in the chamber, one has to think about the gas throughput. That quantity is defined as:

$$q_{gas} = \frac{pV}{t} = \frac{mk_BT}{t} \tag{A.2}$$

with q_{gas} the throughput in [bar L/s], p and V the pressure (in [bar]) and the volume (in [L]) respectively and t the time in [s]. The gas throughput is expressed in terms of the pV flow in the first equality, but it could also be expressed as a function of the mass, as shown in the second equality. There, m is the mass in [kg], k_B the Boltzmann constant in [J/K] and T the temperature in [K]. This relation is obtained by making use of the ideal gas law. Two other common units are used in the vacuum technology to describe the throughput: the [slm] (= 60 [bar L/s]) and the [sccm] (= 60 000 [bar L/s]), i.e. the standard liters

per minute and the standard cubic centimeters per minute respectively. In the pV flow, the temperature is assumed to be known and constant and if the [slm] unit is used, it is assumed to be equal to 273.15 K.

Pump throughput

In a chamber where the pressure is constant, the golden rule is then that **Gas in = Gas out**, i.e. the gas throughput has to be equal to the pump throughput:

$$q_{pump} = \frac{pV}{t} \tag{A.3}$$

where p, V and t are the same quantities than in Equation A.2 but related to the pump. The throughput can be related to the pumping speed:

$$q_{pump} = p\frac{V}{t} = pS \tag{A.4}$$

with S the pumping speed in [L/s] derived in Equation A.1.

Conductance

In the typical case of a supersonic expansion, there is a nozzle between the gas inlet and the chamber. Therefore, there is a huge pressure gradient at the nozzle. The gas flow (or throughput) can not be determined by the Equation A.2 because the pressure is not constant. The aim of the conductance is to determine what is the gas flow in such an element (pipe, nozzle, etc.), where there is a significant pressure gradient. The link between the conductance and the gas flow is defined as:

$$q_{gas} = \Delta p \; C \tag{A.5}$$

with Δp the pressure gradient in [bar] and C the conductance in [L/s]. The conductance depends on the geometry of the element. Some empirical equations about it can be found in the literature. In the case of a nozzle, it can be derived from the kinetic theory of gases. The velocity distribution at a certain temperature and for a certain ion mass follows a Maxwell-Boltzmann distribution. The average velocity is:

$$\overline{v} = \sqrt{\frac{8k_BT}{\pi m}} \tag{A.6}$$

with $\overline{v}$ the mean velocity in [m/s], k_B the Boltzmann constant in [J/K], T the temperature in [K] and m the ion mass in [kg]. The conductance is then written:

$$C = \overline{v}A10^3 \tag{A.7}$$

with A the area of the hole in the nozzle in [m^2]. The 10^3 factor converts the obtained m^3 in L to be coherent with the units of q_{gas}. Such as the capacitance of an electrical circuit, the total capacitance of a system made of a serie of elements (pipes, nozzle, etc.) is given by:

$$\frac{1}{C_{tot}} = \frac{1}{C_1} + \frac{1}{C_2} + ... \tag{A.8}$$

where C_{tot} is the total conductance and C_n is the conductance of each sub-element.

Effective pumping speed

An important and final point about the pumping speed is its link with the conductance. Indeed, if the pump is mounted at the end of a small pipe, its efficiency is drastically reduced compared to a case where it is mounted on the chamber itself. The effective pumping speed is then defined as:

$$\frac{1}{EPS} = \frac{1}{S} + \frac{1}{C} \tag{A.9}$$

where EPS is the effective pumping speed, S the pumping speed indicated on the datasheet of the pump and C the total conductance of the system, all quantities being expressed in [L/s]. One can observe that the objective is consequently to maximise the total conductance of a pumping system to make the pumping as efficient as possible. In this study, the pump is considered to be mounted directly on the chamber and consequently, the reduction of conductance is negligible. However, if one extends the study further, the pumps placed in the next differential pumping units should be more sensitive to that conductance and effective pumping speed concerns.

Given all those definitions and given some input parameters, one can find out the conductance, the gas load and the pumping speed required in order to design a vacuum system.

A.2 Case study of two scenarios

The needed vacuum at the MCP detector is, as said before, at the order of 10^{-7} mbar at least, in order to have a signal that can be efficiently recorded. Two main ideas have been developed until now and are inspired both on the actual setup presented in the chapter 5 (see Figure 5.1 in particular) and on the setup of another experiment in the group of A. Delcorte and C. Poleunis represented in Figure A.2. That second setup is a commercial setup corresponding to the one of A. Roucou and R. Bejjani, but it aims to send large argon clusters on surfaces in order to perform ion sputtering and surface analysis instead of performing ion spectroscopy. It can be used in both pulsed and continuous mode. As long as this setup is a commercial one, neither the pulse rate nor the time of pulse are precisely known. Therefore, the unfavourable case of a continuous jet has been considered.

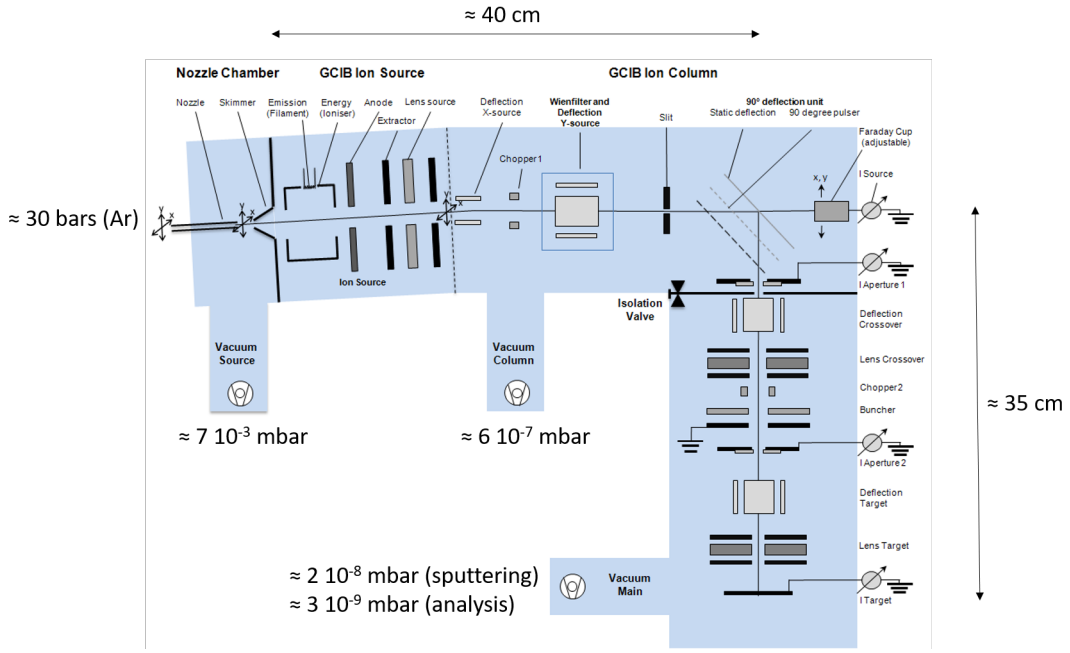

Figure A.2: Schematic representation of one setup actually in place in the group of A. Delcorte.

Two scenarios are currently under investigation in the design of the future experimental setup. They are represented in Figure A.3. In the scenario A, the idea is to keep a setup similar to the actual one. However, as it has been mentioned before, the injection rate of the pulsed valve will be increased by a factor of 33. As a first guess, it means that the pump 1 must have a pumping speed multiplied by the same factor, which is too high even for the modern pumping systems. It has to be consequently adapted, as discussed further. In the scenario B, the first chamber is followed by a second smaller chamber, in order to perform a first efficient differential pumping. The pressure in the first chamber will be higher than in the scenario A. This means that the required pumping speed of the first turbomolecular pump will be smaller. Then, the pump 2 will be a second small turbomolecular pump performing an efficient differential pumping. In summary, the scenario B aims to use two smaller turbomolecular pumps instead of a big one in the scenario A.

In this appendix, the idea is to have a first estimation of the pumping speed required in each scenario. The methodology is the following. Firstly, the conductance associated to the nozzle can be determined thanks to the Equation A.7, by considering CO_2^+ ions at room temperature. The gas flow entering into the chamber is computed in a second step, by knowing the pressure gradient, the time of pulse and the pulse rate of the valve. Then, as long as the stationary regime is considered to be reached in the chamber, i.e. **Gas in = Gas out**, the pumping speed can be easily deduced thanks to the Equation A.4.

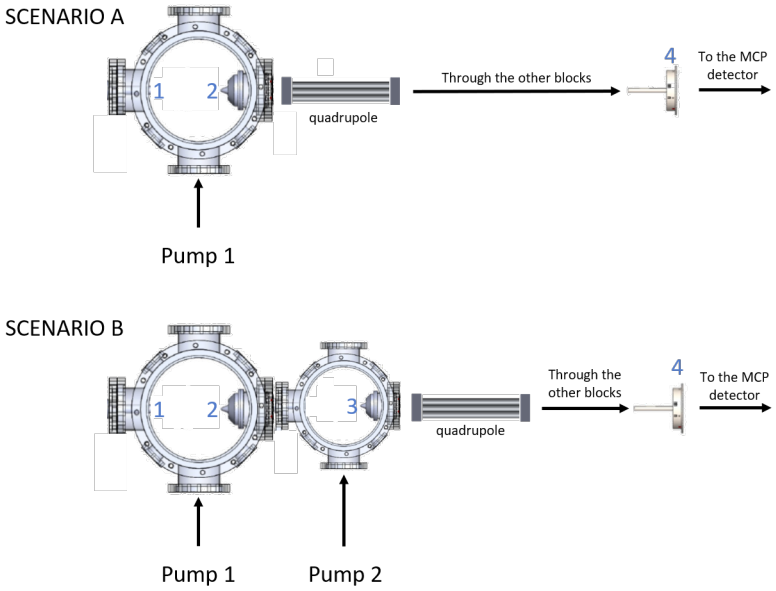

Figure A.3: Schematic representation of the two scenarios under investigation in the design of the new experimental setup. The legend is 1: the nozzle (gas injection), 2: the skimmer, 3: a second skimmer and 4: the differential pumping tube.

All the relevant parameters from the actual setup of A. Roucou and R. Bejjani (noted setup 1), the setup of A. Delcorte and C. Poleunis (noted setup 2) and both scenarios are summed up in the Table A.1. It can be observed that the new experiment will indeed increase the gas flow in the chamber by a factor of 66 (the pressure of the incoming gas is doubled and the repetition rate of the valve is multiplied by 33).

In the scenario B, one has to determine the conductance of the skimmer (2) (see Figure A.3 for the denomination) to have an idea of the required gas flow in the second chamber. As a reference case, the diameter of the skimmer (2) has been taken as equal to 2.5 mm, corresponding to the size of the skimmer placed on the current experiment.

From all the data displayed in the Table A.1, the required pumping speed for each scenario can be estimated. The results are summed up in the Table A.2.

A.3 Observations, solutions and further studies

As a first estimation, the pumping speed required in the scenario A is way too large with respect to the commercially available turbomolecular pumps. The scenario B seems to be better but it will probably be much more costly because of the multiplicity of the pumping systems.

Table A.1: Main parameters of the actual experiment of R. Bejjani and A. Roucou (= setup 1), the one of A. Delcorte and C. Poleunis (= setup 2) and both investigated scenarios. The mean velocity has been computed for a temperature of 293.15 K, a jet of Ar^+ in the setup 2 and a jet of N_2O^+ (or CO_2^+) for the other cases.

	Setup 1	Setup 2	Scenario A	Scenario B
Nozzle				
Diameter [μm]	500	estimated at ∼50	500	500
Δp [bar]	5	30	10	10
Δt [μs]	50	continuous	50	50
Repetition rate [Hz]	30	continuous	1000	1000
Ions				
Mean velocity [m/s]	375	394	375	375
Gas flow [mbar L/s]	0.138	5.80	9.22	9.22
Nominal pressure				
Chamber 1 [mbar]	$1\ 10^{-5}$	$7\ 10^{-3}$	$2\ 10^{-4}$	$7\ 10^{-3}$
Chamber 2 [mbar]	/	/	/	$1\ 10^{-6}$

Table A.2: Pumping speeds for each scenario, derived from the date given in Table A.1. The "expe" row corresponds to the pumping speed of the pump as currently installed in the corresponding experimental setup.

Pumping speed [L/s]	Setup 1	Setup 2	Scenario A	Scenario B
Pump 1 - experiment	2300	255	/	/
Pump 1 - computed	13800	1777	46 009	1316
Pump 2 - computed	/	/	/	500 - 1000 ?

Those results have to be put into perspective because of the large number of approximations that have been done in this first study. As it can be seen in the experiment of A. Roucou and R. Bejjani, and in the experiment of A. Delcorte and C. Poleunis, the computed pumping speed is way larger than the one of the installed pumps. On both setups, there is a ratio of around 1/6 between the pumping speed of the currently installed pump (row 1 in the Table A.2) and the computed pumping speed from the data in the Table A.1 (row 2 in the Table A.2). The main hypothesis to explain this ratio is that it has been considered that all the gas entering into the chamber has to be pumped, which is of course not the case. It is quite difficult, without any finite element simulation tool, to estimate the fraction of gas that is transmitted through the skimmer and the fraction of gas that is lost in the chamber, i.e. the gas that has to be effectively pumped. This could be estimated thanks to MOLFLOW+, in a more complete simulation about the entire vacuum system. Also, in the scenario

B, it is difficult to estimate the pressure gradient between both chambers because again, one does not have a precise knowledge about the amount of gas passing through the skimmer.

In terms of available pumping systems in the market, the turbomolecular pumps from Pfeiffer Vacuum can reach pumping speeds up to 3204 L/s for the best model. Such a system might be required in the scenario A, even with a much better estimation of the needed pumping speed. In the scenario B, both required pumping speeds stay in a range of values that are achievable with commercial turbomolecular pumps. For example, the ATH 1600 L/s pump from Pfeiffer seems to be more than sufficient for the pump 1.

One could also think about the parameters that could be optimised in order to reduce the required pumping speed, especially in the scenario A. The high repetition rate is a requirement for the future experiment so it must be kept at that high value. Still, other parameters such as the diameter of the nozzle could be reduced, implying a lowering of the gas flow. If the nozzle can be changed with another one having a twice smaller diameter, the gas flow will be reduced by four because there is a quadratic relation between both quantities. The pressure gradient at the nozzle could be reduced too, even if this will affect the subsequent supersonic expansion. For example, if both the diameter of the nozzle and the pressure gradient are reduced by a factor of 2, the gas flow becomes $q_{gas} = 1.15$ mbar.L/s, leading to a required pumping speed of $S = 5761$ L/s in the scenario A. This remains out of reach for the commercially available pumping systems, but as said before, this value will be reduced by considering other factors through numerical simulations.

As a conclusion, one can say that even by optimising the different parameters of the experimental setup, it seems that a system with two differential pumping levels is required: the pumping speed in the scenario A is really large and might be too difficult to handle. The pumping system might limit the abilities and some further improvements of the experimental setup such as an increase of the pulse rate for example. However, one has to carefully chose the pumps in the scenario B to minimise its cost. Further studies have to be performed in order to have a better idea of the exact gas load and consequently of the desired pumping speed of that system. The experimental elements could also be changed, for example by reducing the diameter of the nozzle, by reducing the diameter of the skimmer between both chambers, by slightly increasing the operating pressure in the first chamber, etc. Further simulation studies with MOLFLOW+ and with the whole experimental setup should precise this first investigation.

Appendix B

GEM file example

```
; Basic quadrupole design
; e(0) for outer cylinder
; e(1) and e(2) for the rods
; e(3) and e(4) for the entrance and exit electrode

# local r0 = 4.5        -- half min distance between opposite rods in mm
# local rrod = 6.3      -- rod radius in mm
# local gu_mm = 4       -- grid units per mm
# local outer_cap = 32  -- outer cap of 32 mm radius
# local nx = math.floor(outer_cap * gu_mm) + 1
# local quad_length = 200*gu_mm

; outer_cap
; noted e(0) because it is grounded
  ; (not considered as an electrode by SIMION)
e(0){
  fill{
        within{cylinder(0,0,801,128,128,800)}
        notin{cylinder(0,0,801,116,116,800)}
        notin_inside{locate(0,64,401,1,,,90){circle(0,0,56)}}
        notin_inside{locate(64,0,401,1,90){circle(0,0,56)}}
  }
}

; rods
e(1) {
  locate(0,0,0,1) {
    fill { within { cylinder($((r0+rrod)*gu_mm),0,801,$(rrod*gu_mm),$(
   rrod*gu_mm),800)}}
  }
}
; rod 2 - pi-shifted with respect to the rod 1
e(2) {
  locate(0,0,0,1, 0, 90) {
    fill { within { cylinder($((r0+rrod)*gu_mm),0,801,$(rrod*gu_mm),$(
   rrod*gu_mm),800)}}
```

```
}

; circular electrodes : 12 mm inner radius / 23 mm outer radius
; before the quadrupole
locate(0,0,-52,4){
  e(3){
        fill{ within{circle(0,0,38) locate(0,0,0,1){box3d
   (-38,-38,0,38,38,12)}} notin{circle(0,0,23)} }
        fill{ within{circle(0,0,23) locate(0,0,0,1){box3d
   (-23,-23,4,23,23,8)}} notin{circle(0,0,12)} }
        }
}
; after the quadrupole
locate(0,0,806,4){
  e(4){
        fill{ within{circle(0,0,38) locate(0,0,0,1){box3d
   (-38,-38,0,38,38,12)}} notin{circle(0,0,23)} }
        fill{ within{circle(0,0,23) locate(0,0,0,1){box3d
   (-23,-23,4,23,23,08)}} notin{circle(0,0,12)} }
        }
}
```

Appendix C

LUA file example

```
-- Lua workbench program for quadrupole simulation
--
-- C. Sepulchre 2020-02
-- Inspired from D.Dahl. D.Manura-2006-08/2007-03 (c) 2006-2007
↪  Scientific Instrument Services, Inc. (Licensed under SIMION 8.0)

      --- if a result has to be stored in an output file ----

local currentParticleNum = 0
-- file where the result of the simulation will be stored --
local dataFile = 'mass_scan_apex.txt'
local outputFile = io.open(dataFile, 'w') -- test opening file
outputFile:close()
local outputFile = io.open(dataFile, 'a') -- append mode

      -------------------- initialisation ------------------

simion.workbench_program()

-- Adjustable variables at the beginning of the simulation
adjustable pe_update_each_usec = 0.05 -- time step
adjustable phase_angle_deg = 0.0      -- RF phase shift quad (deg)

adjustable dc_voltage = 0     -- quad DC voltage
adjustable rf_voltage = 15    -- quad RF max voltage
adjustable in_voltage = 0     -- in electrode voltage
adjustable out_voltage = 0    -- out electrode voltage
adjustable frequency_hz = 1E6 -- RF frequency of quad (Hz)

-- time before switching inner electrode in trapping mode (µs)
```

```
adjustable switch_time1 = 0
adjustable trapping_time = 0  -- trapping time (μs)

-- Temporary variables used internally
local effective_radius_mm = 4.5 -- quadrupole free radius
local last_pe_update = 0.0 -- potential energy surface update time (μs)

-- Convert to SI units
local q = 1.602176462*10^-19              -- (C/e)
local m = ion_mass * 1.66053886*10^-27    -- (kg/u)
local omega = frequency_hz * 2 * math.pi  -- (rad/cycle)
local r0 = effective_radius_mm / 1000     -- (m/mm)

function segment.fast_adjust()

    -- frequency_hz (in radians/μs) --
   local omega = frequency_hz * (1E-6* 2 * math.pi)
   -- phase_angle_deg (in rad) --
   local theta = phase_angle_deg * (math.pi / 180)

   local tempvolts = dc_voltage - rf_voltage * cos(ion_time_of_flight *
    ↪  omega + theta )  -- rods voltage

   adj_elect01 = tempvolts    -- voltage rod 1
   adj_elect02 = - tempvolts  -- voltage rod 2

   if ion_time_of_flight < switch_time1 then
   -- inner electrode is "off" before switching time --
     adj_elect03 = 0
     adj_elect04 = out_voltage
   elseif ion_time_of_flight < trapping_time then
   -- both electrodes are "on" in trapping mode --
     adj_elect03 = in_voltage
     adj_elect04 = out_voltage
   else
   -- exit electrode is "off" after trapping time --
     adj_elect03 = in_voltage
     adj_elect04 = 0
   end
end

function segment.other_actions()
    -- if an update of the PE surface is required --
```

```
    if abs(ion_time_of_flight - last_pe_update) >= pe_update_each_usec
    ↪  then
     last_pe_update = ion_time_of_flight
     sim_update_pe_surface = 1
    end
end

function segment.tstep_adjust()
    -- adjustment of the time step
    ion_time_step = min(ion_time_step, 0.1)
end

function segment.terminate()

    -- write the result in output file --

    ↪  outputFile:write(ion_number..'\t'..ion_pz_mm..'\t'..frequency_hz..'\n')
    outputFile:flush()  --updates file while simulation is running

     -- count the number of splats --
    currentParticleNum = 1 + currentParticleNum

    if currentParticleNum == 1000 then -- end of the simulation
      currentParticleNum = 0           -- reset of the parameters
      -- the other parameters can be changed here is case of a scan --
    end

    -- restart the simulation with the updates parameters --
    sim_rerun_flym = 1

    -- example of one final condition for the scan --
    if frequency_hz > 1.2E6 then
      sim_rerun_flym = 0
    end
end
```

Appendix D

Mathieu solver

```
# This code simulates trajectories of ions in a multipolar device.
# The differential Mathieu equation is solved, taking into account
# a set of initial parameters.
# Ions can also be trapped in the latter device, given a bucket exponent
# and a trapping voltage
# ----------------------------------------
# Created by Cyrille Sepulchre - April 2020

from numpy import *
import matplotlib.pyplot as plt
import scipy.integrate as ode
import scipy.signal as s

# Definition of the Mathieu equation.
# The second order differential equation is written as a set of two
# differential equations of order one as follow:
# x' = u
# u' = (-a + 2*q*cos(2*xi+phi))*x
# with a and q the adimentional Mathieu factors related to the voltages
# phi the phase shift and xi the adimentional factor related to the time
#
# n is the multipole order (2 for quadrupole, 4 for octupole, etc.)
#
# Trap determines if a trapping potential has to be applied or not
def Mathieu(xi,x,a,a_trap,q,phi,n,Trap):

    x_prime = x[1]
    u_prime = (a-2*q*cos(n*xi+phi))*
```

```
    (combi(0,n-1)*x[0]**(n-1) - combi(2,n-1)*x[0]**(n-3)*x[2]**2 +
    ↪  combi(4,n-1)*x[0]**(n-5)*x[2]**4 -
    ↪  combi(6,n-1)*x[0]**(n-7)*x[2]**6 +
    ↪  combi(8,n-1)*x[0]**(n-9)*x[2]**8 -
    ↪  combi(10,n-1)*x[0]**(n-11)*x[2]**10)
    # all those combinations come from the equation for a
    # multipolar element of order 2n. Higher order terms
    # can be added to handle higher order multipoles.

    y_prime = x[3]
    v_prime = -(a-2*q*cos(n*xi+phi))*
    (combi(1,n-1)*x[0]**(n-2)*x[2] - combi(3,n-1)*x[0]**(n-4)*x[2]**3 +
    ↪  combi(5,n-1)*x[0]**(n-6)*x[2]**5 -
    ↪  combi(7,n-1)*x[0]**(n-8)*x[2]**7 +
    ↪  combi(9,n-1)*x[0]**(n-10)*x[2]**9 -
    ↪  combi(11,n-1)*x[0]**(n-12)*x[2]**11)

    # along z, the equation of motion depends either on the mode
    # (trapping or not) and on the shape of the trapping potential
    if Trap!=0:
        if bucket > 2:
            z_prime = x[5]
            w_prime = -bucket/2*x[4]**(bucket-1)*a_trap*
            (2/(L*pi*f))**(bucket-2)*exp(-(2*x[4]/(L*pi*f))**bucket)
        else:
            z_prime = x[5]
            w_prime = -x[4]*a_trap
    else:
        z_prime = x[5]
        w_prime = 0

    return array([x_prime, u_prime, y_prime, v_prime, z_prime, w_prime])

# small auxiliary function used to compute the combination
# of n number taken in a sample of k.
def combi(k,n):
    if (n-k)<0:
        return 0
    else:
        return math.factorial(n)/(math.factorial(k)*math.factorial(n-k))

# Check if the ion, given its x & y vectors, crashed onto the rods
# of the quadrupole (if it exceeds the free radius r0).
```

```
# x and y are assumed to be same length and that each point corresponds
# to the same z position.
# Returns 0 if the trajectory is stable, 1 if the ion crashed on one rod
def splat_rod(x,y):
    for i in range(len(x)):
        if sqrt(x[i]**2+y[i]**2) > 1:
            return 1
    return 0

# Computes the transmission out of the quadrupole for a certain
# distribution file given in distr [x,x',y,y',z,z'] and for a
# certain dataset given in a, q and/or phi.
# Returns the transmission for each point of the scan, written in
# an output file for each (a,q) condition
def simulation(distr,xi,a,q,phi):

    transmission = []
    file = open("scan_mass_apex.txt", "w")
    for j in range(len(a)):
        transmis = 0
        if q[j] < 1:
            print ("dealing with q = " + str(q[j]))
            # computation of the solution of the Mathieu equation
            for i in range(len(distr)):
                # initial conditions in SPACE
                xstart = [distr[i,0]/r0,distr[i,3],distr[i,1]/r0,
                          distr[i,4],distr[i,2],distr[i,5]]
                # solve the Mathieu equation for the given parameters
                sol =
                ↪  ode.solve_ivp(Mathieu,xiSpan[i,:],xstart,method='RK45',
                       t_eval=linspace(xiSpan[i,0],xiSpan[i,1],m+1),
                       args=(a[j],a_trap,q[j],phi,n,Trap))

                # extraction of the solution
                x_sol = sol.y[0,:]; px_sol = sol.y[1,:];
                y_sol = sol.y[2,:]; py_sol = sol.y[3,:];
                z_sol = sol.y[4,:]; pz_sol = sol.y[5,:];
                time = sol.t
                # the above quantities can be used to plot the
                # trajectories or if one wants to write the whole
                # trajectories of each ion in the output file

                # for transmission analysis
```

```
                if splat_rod(x_sol, y_sol, r0) == 0:
                    transmis = transmis + 1

            # write the transmission in the output file
            transmission.append(transmis)
            file.write(str(a[j]) + "\t" + str(q[j]) + "\t"
                       + str(transmis) + "\n")
    file.close()

# Function used in the trapping mode
# Traps the particles given in distr during a certain trapping_time
#
# In this first version, a, a_trap, q and phi are considered as scalars
# (no scan possible yet)
# A second version would allow to write the result in an output file and
# to handle scans
def trapping(distr,a,a_trap,q,phi,trap_time):
    transmis = 0
    for i in range(len(distr)-1):
        # initial conditions in SPACE
        xStart = [distr[i,0]/r0,distr[i,3],distr[i,1]/r0,
        distr[i,4],(distr[i,2]-L/2)*pi*f*2/n,distr[i,5]]
        # initial conditions in TIME
        xiStop_trap = 2*pi*f*trap_time/n
        xiSpan_trap = [xiStop_no_trap, xiStop_trap]
        xi_trap = linspace(xiStop_no_trap,xiStop_trap,m+1)

        sol_trap = ode.solve_ivp(Mathieu,xiSpan_trap,xStart,method='RK45',
                    t_eval=xi_trap,args=(a,a_trap,q,phi,n,Trap))

        if splat_rod(sol_trap.y[0,:], sol_trap.y[2,:], r0) == 1:
            print ('ion number ' + str(i) + ' crashed while trapping')
            crash = 1
        else:
            # if the ion exceeds the limits of the quadrupole
            # happens if a_trap is too low w.r.t. the kinetic energy
            # of the ion.
            if min(sol_trap.y[4,:])/(pi*f) < -L/2
                    or max(sol_trap.y[4,:])/(pi*f) > L/2:
                print ('ion number ' + str(i) +  ' not trapped')
                crash = 1
            else:
                print ('ion number ' + str(i) + ' successfully trapped')
```

```
                # eventual extraction of the solution for any plot
                # or any output file generation
                x_sol = sol_trap.y[0,:]; px_sol = sol.y[1,:];
                y_sol = sol_trap.y[2,:]; py_sol = sol.y[3,:];
                z_sol = sol_trap.y[4,:]; pz_sol = sol.y[5,:];
                time = sol_trap.t

                transmis += 1

    print (str(transmis) + ' ions transmitted')

# Main block of the code
# Initialise all the parameters and launch the corresponding function
if __name__=="__main__":

    ## FUNDAMENTAL CONSTANTS ##

    amu = 1.66053906660e-27 # atomic mass number [kg]
    eV = 1.602176634e-19 # electron volt [J]

    ## GENERAL PARAMETERS ##

    mass = 44*amu    # ion mass
    n = 2            # multipole order (2 = quad, 4 = oct, etc.)
    r0 = 4.5e-3      # free radius [m]
    L = 20e-2        # quadrupole length [m]
    f = 1e6          # RF frequency [Hz]
    omega = 2*pi*f   # angular frequency [rad/s]
    phi = 0          # RF phase

    # The following parameters are (un)commented depending on the scan #

    U = 0            # DC voltage applied to the electrodes
    V = 15           # RF voltage applied to the electrodes
    trap_v = 5       # trap voltage (= electrodes voltages)

    v0 = 600                      # initial speed of the ions [m/s]
    e0_kin = mass*v0**2/(2*eV)    # inital kinetic energy of ions [eV]
    V_extr = 2                    # extraction voltage [V]
    e_kin_extr = e0_kin + V_extr # kinetic energy after extraction
    v_extr = sqrt(e_kin_extr*2*eV/mass) # speed after extraction [m/s]

    ## a and q - again computed differently as a function of the scan ##
```

```
a = n**3*eV*U/(mass*omega**2*r0**2)
q = n**3*eV*V/(2*mass*omega**2*r0**2)
a_trap = 8*eV*trap_v/(mass*omega**2*(L/2)**2)

# example for a scan in U/V
U = linspace(0,0,50)
V = linspace(0,120,50)
a = 8*eV*U/(mass*omega**2*r0**2)
q = 4*eV*V/(mass*omega**2*r0**2)

## TRAPPING PARAMETERS ##

Trap = 1
trap_time = 1e-4
# exponent of the bucket-like potential
# bucket < 2 is considered as a harmonic potential
bucket = 20

## INITIAL CONDITIONS ##

# computation for a complete ion distribution
# the file in "file" contains the distribution parameters
file = ["gaussian.txt"]
distr = loadtxt(file[0])

# extracting the initial conditions in TIME
v_extr = []; xiSpan = zeros((len(distr),2))
for i in range(len(distr)):
    v_extr.append(sqrt(distr[i,5]**2 + 4*eV/(44*amu)))
    tstart = 0; tend = L/v_extr[i]
    xiSpan[i,0] = pi*f*tstart; xiSpan[i,1] = pi*f*tend

# if only one ion trajectory is computed (no distribution)
tstart = 0; tend = L/v_extr

xiStart = 2*pi*f*tstart/n; xiStop = 2*pi*f*tend/n
xiSpan = [xiStart,xiStop]
m = 10000                              # number of time steps
xi = linspace(xiStart,xiStop,m+1)    # time vector

# initial conditions in SPACE
# respectively [x0/r0, x0', y0/r0, y0', z0, z0']
```

```
xStart = [0.1, 0, 0.1, 0, 0.0, v_extr]

## LAUNCHING THE SIMULATION ##

if Trap==0:
    simulation(distr,xiSpan,a,q,phi)
else:
    trapping(distr,xiSpan,a,a_trap,q,phi,trap_time,switch_time)

## EXTRACTION OF THE SOLUTION ##
# If stored in an output file
t = loadtxt("scan_mass_apex.txt")

# If only one ion trajectory for one (a,q) is computed
sol = ode.solve_ivp(Mathieu,xiSpan,xStart,method='RK45',
                    t_eval=xi,args=(a,a_trap,q,phi,n,Trap))

# extraction of the solution
x_sol = sol.y[0,:]; px_sol = sol.y[1,:];
y_sol = sol.y[2,:]; py_sol = sol.y[3,:];
z_sol = sol.y[4,:]*n/(2*pi*f); pz_sol = sol.y[5,:];
time = sol.t

# example of plot (simple trajectory)
plt.figure()
plt.plot(z_sol,x_sol)
plt.xlabel('z [m]')
plt.ylabel(r'x/r$_0$')
plt.show()
```

UNIVERSITÉ CATHOLIQUE DE LOUVAIN
École polytechnique de Louvain
Rue Archimède, 1 bte L6.11.01, 1348 Louvain-la-Neuve, Belgique | **www.uclouvain.be/epl**